

# CHARACTERIZATION OF NOVEL PLASMONIC, PHOTONIC, AND SEMICONDUCTOR MICROSTRUCTURES

by

Jasmine Soria Sears

---

Copyright © Jasmine Soria Sears 2017

A Dissertation Submitted to the Faculty of the

COLLEGE OF OPTICAL SCIENCES

In Partial Fulfillment of the Requirements

For the Degree of

DOCTOR OF PHILOSOPHY

In the Graduate College

THE UNIVERSITY OF ARIZONA

2017

THE UNIVERSITY OF ARIZONA  
GRADUATE COLLEGE

As members of the Dissertation Committee, we certify that we have read the dissertation prepared by Jasmine Soria Sears entitled

Characterization of Novel Plasmonic, Photonic, and Semiconductor Microstructures

and recommend that it be accepted as fulfilling the dissertation requirement for the Degree of Doctor of Philosophy

\_\_\_\_\_  
Euan McLeod Date: 8/14/17

\_\_\_\_\_  
Miroslav Kolesik Date: 8/14/17

\_\_\_\_\_  
Robert Norwood Date: 8/14/17

Final approval and acceptance of this dissertation is contingent upon the candidate's submission of the final copies of the dissertation to the Graduate College.

I hereby certify that I have read this dissertation prepared under my direction and recommend that it be accepted as fulfilling the dissertation requirement.

\_\_\_\_\_  
Dissertation Director: Euan McLeod Date: 8/14/17

### **STATEMENT BY AUTHOR**

This dissertation has been submitted in partial fulfillment of requirements for an advanced degree at the University of Arizona and is deposited in the University Library to be made available to borrowers under rules of the Library.

Brief quotations from this dissertation are allowable without special permission, provided that accurate acknowledgment of source is made. Requests for permission for extended quotation from or reproduction of this manuscript in whole or in part may be granted by the head of the major department or the Dean of the Graduate College when in his or her judgment the proposed use of the material is in the interests of scholarship. In all other instances, however, permission must be obtained from the author.

SIGNED: Jasmine Soria Sears

## ACKNOWLEDGEMENTS

Thank you to Professors Galina Khitrova and Hyatt Gibbs for welcoming me into the QNOS group despite difficult circumstances. I truly enjoyed the projects I worked on, the people I met, and the places I went. I'd also like to thank the rest of the QNOS group for their unrelenting guidance and encouragement.

Thank you to Professor Euan McLeod for accepting me into your group after Galina passed away. Your mentorship made completing my Ph.D. far more feasible than it otherwise would have been.

The QNOS group had a true spirit of collaboration, working on projects with groups across the world. I'd like to thank these collaborators for making my research possible: Dr. Josh Hendrickson and his group at AFRL in Dayton; Professor Dr. Dagmar Gerthsen and her group at Karlsruhe Institute of Technology; Professor Axel Scherer's group at Caltech; Professor Yong-Hee Lee and his group at KAIST; and Antti Säynätjoki and Lasse Karvonen at Aalto University. In addition, I gratefully acknowledge the use of facilities with the LeRoy Eyring Center for Solid State Science at Arizona State University, with special thanks to John Mardinly.

Although I've always wanted to be a scientist, I wasn't sure what field to pursue until I spent a summer in Professor Jun Jiao's lab through the ASE program. I'd like to thank Professor Jiao and Devon McClain for allowing a high school student to experience real research, and for starting me down the path to an Optics degree.

I made many friends during my time at the University of Arizona who contributed to getting me to the finish line. I'd like to thank Sarah Netherton, in particular, for being a powerful role model, but I'm grateful to all my friends here.

I'd also like to thank Abe, Castile, Andrea, Lisa, Chris, Maurer, Abigail, Oren, Wendell, Mike, Steven, and Jacob for keeping me company for so many years, and for listening to so much of my venting and gushing.

And finally, I'd like to thank my mother and the rest of my family for holding me to such high standards, and for celebrating every step of my journey.

Thank you.

## DEDICATION

*To Reverendo Roberto Soria.*

## TABLE OF CONTENTS

List of Figures .....	8
List of Tables .....	10
Abstract .....	11
Chapter 1: Introduction .....	12
1.1 Mathematical Concepts.....	12
1.1.1 Quality Factor .....	12
1.1.2 Energy and Wavelength.....	13
1.1.3 Particle in a Box.....	13
1.1.4 Purcell Enhancement .....	16
1.2. Definitions of Terms .....	17
1.2.1 Indium Island Samples.....	17
1.2.2 Arbitrary Units .....	18
1.3. Layout of Dissertation .....	19
Chapter 2: Methods.....	20
2.1 Photoluminescence Measurement.....	20
2.2 Molecular Beam Epitaxy .....	21
2.3 TEM .....	24
2.4 Energy Dispersive Spectroscopy .....	27
Chapter 3: Silicon Nanobeams.....	33
3.1 Motivation.....	33
3.2 Erbium Doping .....	34
3.3 Fano Resonance .....	38

Chapter 4: TEM EDS Analysis of Self-Assembled Indium Islands .....	42
4.1 Motivation.....	42
4.2 TEM Results .....	46
4.3 EDS Results .....	49
4.4 Discussion of Results.....	54
Chapter 5: Microdome Formation on Indium Island Samples.....	61
5.1 Context of Observation.....	61
5.2 Characterization of Microdomes .....	63
5.3 Attempts to Replicate.....	65
5.4 Possible Explanations .....	66
5.3 Potential Applications.....	68
Chapter 6: Localized Sub-Surface Indium Layers.....	71
6.1 Motivation.....	71
6.2 Experimental results .....	72
6.3 Further analysis and possible explanations.....	75
Chapter 7: Conclusion and Future Directions.....	78
Appendix A – Fiber Transmission Data .....	81
Appendix B – TEM EDS Analysis of Epitaxially-Grown Self-Assembled Indium Islands .....	84
Appendix C – Additional TEM EDS Data .....	91
References.....	95

## LIST OF FIGURES

Figure 1.1 SEM images of indium island samples In38, In44, and In54.....	18
Figure 2.1 Bandgap energies and lattice constants of III-V semiconductors .....	23
Figure 2.2 TEM image resolving the different crystal structures of two adjacent materials .....	24
Figure 2.3 In54 after electron-beam deposition of platinum .....	26
Figure 2.4 In54 after ion-beam-deposited platinum layer .....	26
Figure 2.5 A series of images illustrating the TEM cross-section preparation process.....	27
Figure 2.6 An example EDS spectrum .....	29
Figure 2.7 Illustration of the volume of x-ray generation from a stationary electron beam.....	30
Figure 2.8 Software readout of quantitative EDS results from In44 island 1 .....	31
Figure 2.9 EDS line scan of In54.....	31
Figure 2.10 Indium and composite EDS area maps of In38 island 1 .....	32
Figure 3.1 SEM image of a silicon nanobeam.....	33
Figure 3.2 Diagram of a silicon nanobeam with simulated electric field energy density.....	34
Figure 3.3 SEM images of a silicon nanobeam before and after ALD coating .....	35
Figure 3.4 Spectrum from nanobeam sample coated with erbium-containing ALD.....	37
Figure 3.5 Nanobeam resonance data overlaid with a Fano-Lorentz fit.....	40
Figure 4.1 Indium, zinc blende, and GaAs crystal structures .....	47
Figure 4.2 TEM images of In38 Island 2 with and without region outlines.....	48
Figure 4.3 Low-magnification TEM image of In54. ....	48
Figure 4.4 False-color elemental composition maps of In38, In44, and In54 islands .....	49
Figure 4.5 In38 Island 1 line scan.....	50
Figure 4.6 In38 Island 2 line scan.....	51

Figure 4.7 TEM image of In54 with quantitative EDS measurement points indicated.....	52
Figure 4.8 Comparison of EDS colormap and TEM image of In38 Island 2 .....	53
Figure 4.9 In38 quantitative EDS results from Germany .....	55
Figure 5.1 First observation of microdome formation.....	61
Figure 5.2 AFM image of In44 .....	62
Figure 5.3 SEM image of In54 at the start of the ion milling process .....	63
Figure 5.4 SEM image of In54 showing five islands with attached microdomes. ....	64
Figure 5.5 EDS line scan of dome cross-section .....	64
Figure 5.6 SEM and AFM images of rapidly-cooled indium islands.....	67
Figure 6.1 TEM micrograph of the hollow region between In44 islands.....	72
Figure 6.2 EDS line scan through sub-surface indium layer .....	72
Figure 6.3 Images of other sub-surface indium layers.....	73
Figure A.1 Fiber transmission data across 90° of polarization on a single nanobeam. ....	81
Figure A.2 Higher-resolution plots of three of the lines from Figure A.1.....	82
Figure A.3 Lineshape comparison with and without the fiber connected directly to the detector	83

## LIST OF TABLES

Table 1.1 Indium island growth parameters .....	17
Table 4.1 Average elemental composition of island interiors by atomic percentage. ....	51
Table 4.2 Elemental composition of In54 measurement points by atomic percentage. ....	52

## ABSTRACT

The fields of telecommunications and optoelectronics are under constant pressure to shrink devices and reduce power consumption. Micro-scale photonic and plasmonic structures can trap light and enhance the brightness of active emitters; thus, these types of structures are promising avenues to accomplishing the goals of miniaturization and efficiency. A deeper understanding of specific structures is important in order to gauge their suitability for specific applications. In this dissertation, two types of microstructures are explored: one-dimensional silicon photonic crystals and self-assembled indium islands. This dissertation will provide novel characterization of these structures and a description of how to utilize or compensate for the observed features.

A photonic crystal can act as a tiny resonator for certain wavelengths, making it a promising structure for applications that require extremely small lasers. However, because of silicon's indirect bandgap, a silicon photonic crystal cavity would require the addition of an active emitter to function as a light source. Attempts to incorporate erbium into these cavities, and the observation of an unusual coupling phenomenon, will be discussed.

Self-assembled indium islands are plasmonic structures that can be grown via molecular beam epitaxy. In theory, these islands should be pure indium nanoantennas on top of a smooth gallium arsenide substrate. In practice, the component materials are less segregated than predicted, giving rise to unexpected hollow dome shapes and a sub-surface indium layer. Although these features were not an intended result of indium island growth, they provide information regarding the island formation process and potentially contribute additional applications.

## CHAPTER 1: INTRODUCTION

Micro- and nanostructures have diverse technological applications [1][2][3]. Reduced feature sizes result in phenomena that are not observed at the macro scale, such as quantum confinement and Purcell enhancement. By allowing us to exploit these phenomena, microstructures have opened up exciting new possibilities such as plasmonic metamaterials [4] and photonic circuits [5]. Due to the miniscule size of these structures, variations in composition of a few atoms can drastically alter their behavior.

### 1.1 Mathematical Concepts

#### 1.1.1 Quality Factor

Quality factor, or Q-factor, is a parameter used to describe resonators. Conceptually, the Q-factor is defined as

$$Q = 2\pi \frac{\textit{stored energy}}{\textit{energy loss per cycle}}, \quad (1.1)$$

with higher Q-factors indicating lower percentage loss per round trip of the resonator [6]. In general, a high Q-factor implies a low-loss resonator, which is often a desirable property. Silicon resonant cavities exhibit Q-factors exceeding  $10^5$  [7], although metallic cavities tend to have much lower Q-factors (on the order of 10) [8].

It is often difficult to directly determine the energy stored in a particular resonator, or the energy lost per cycle. Instead, an alternate form of Equation 1.1 is used to determine the Q-factors of some cavities:

$$Q = \frac{\textit{center wavelength}}{\textit{spectral width}}. \quad (1.2)$$

The center wavelength of a cavity is its resonant wavelength. To calculate the spectral width of a cavity, a curve can be fit to the cavity resonance; the spectral width corresponds to the full-width-half-max (FWHM) of this curve.

### 1.1.2 Energy and Wavelength

The energy  $E$  of a photon can be related to its wavelength  $\lambda$  in free space using the equation

$$E = \frac{hc}{\lambda}, \quad (1.3)$$

with  $h$  being the Planck Constant and  $c$  being the speed of light in a vacuum. Thus, knowing the energy of a photon provides its wavelength, and vice versa. This is valuable in the context of transitions between energy levels, as the difference in initial and final particle energies can be inferred from the wavelength of the emitted or absorbed photon, and an emission wavelength can be predicted from the known spacing between energy levels.

### 1.1.3 Particle in a Box

A common simplification of quantum confinement is the idea of a particle (an electron, for our purposes) trapped in a potential well (a “box”) of infinite depth. Rather than being permitted to stably exist in a state with an arbitrary associated energy value, the particle can only occupy certain energy levels, given by

$$E = \frac{n^2\pi^2\hbar^2}{2ma^2}. \quad (1.4)$$

In this equation,  $n$  is a positive integer indicating the energy level,  $m$  is the mass of the particle, and  $a$  is the width of the box. If enough energy is imparted to the particle to move it from one energy level to the next, the particle can eventually drop back down to a lower energy level by releasing a photon with energy equivalent to the difference in energy levels. If a particle receives

an amount of energy that would place it between allowed energy levels, the particle will rapidly lose energy in ways that do not emit photons until the particle has reached an allowed energy level.

As indicated by Equation 1.4, separation between the energy levels decreases as the width of the box increases. As would be expected, as the width of the box becomes infinite, the separation between allowed energy levels becomes negligible, and the particle approaches classically-predicted behavior.

The particle in an infinite-walled box concept can be adjusted to better approximate the reality of semiconductor structures by making the heights of the walls finite. This seemingly-simple adjustment brings about two key differences from the infinite potential well case: the particle can now spatially exist, albeit rarely, within the walls of the box, and the values of the allowed energy levels can no longer be solved for analytically. The equation for determining allowed energy levels becomes the system of equations

$$\left| \cos\left(\frac{ka}{2}\right) \right| = \frac{k}{k_0} \text{ or } \left| \sin\left(\frac{ka}{2}\right) \right| = \frac{k}{k_0} \quad (1.5-a)$$

$$\tan\left(\frac{ka}{2}\right) > 0 \quad (1.5-b)$$

$$k = \sqrt{\frac{2m(E + V_0)}{\hbar^2}} \quad (1.5-c)$$

$$k_0 = \sqrt{\frac{2mV_0}{\hbar^2}} \quad (1.5-d)$$

where  $V_0$  is the height of the potential barrier (in this convention, the energy value of the bottom of the well is  $-V_0$ , and the energy value of the barrier is 0) [9]. This system of equations can be solved computationally for the allowed energies  $E$ .

In the case of a semiconductor quantum well, the particle in a finite-walled box approximation can be further refined. Semiconductors have valence and conduction bands, with the conduction band having higher energy than any valence bands. This structure can be approximated by considering two finite-walled boxes, one inverted and placed below the other. The heights of the walls are determined by the bandgaps of the materials that make up the well, and the width of the boxes is determined by the physical width of the well [10]. In this model, the allowed energy levels of the conduction and valence bands can be calculated separately, and a quantum well emission wavelength can be determined by finding the energy difference between, for instance, the ground states of each band.

Quantum dots can be approximated via a conceptual model similar to that used for quantum wells, but rather than experiencing quantum confinement in only one dimension, dots experience quantum confinement in all three spatial dimensions. The particle in a box idea can be extended to multiple dimensions by having a separate set of boxes for each dimension, with quantum dots requiring three dimensions. (Quantum wells could receive the same three-dimensional treatment, with the boxes in two dimensions being sufficiently wide to treat classically.)

The particle in a box model has thus far assumed that the particle can transition from one allowed energy state to another through solely the absorption or emission of energy. In the III-V semiconductor systems considered in this dissertation, this assumption is valid. In other words, these semiconductors have direct bandgaps. However, although silicon is also a semiconductor, it has an indirect bandgap, meaning that both an energy and a momentum difference exist between its conduction and valence bands. In the case of silicon's indirect bandgap system, an electron must absorb both a photon and a phonon near-simultaneously to transition from the

valence to the conduction band, making inter-band transitions far more difficult to accomplish than in a direct bandgap system.

#### 1.1.4 Purcell Enhancement

The Purcell factor describes the change in spontaneous emission rate of an emitter in a resonant cavity compared to an uncoupled emitter. Spontaneous emission is the emission of a photon due to the transition of an electron from a higher energy state to a lower one. Other forms of energy loss which do not result in photon emission are also possible, and become more likely the longer the electron remains in the higher energy state. Thus, by increasing the rate of spontaneous emission, the fraction of absorbed energy emitted as photons also tends to increase.

The Purcell factor is usually given by

$$F_p = \frac{3}{4\pi^2} \left( \frac{\lambda_0}{n} \right)^3 \frac{Q}{V}, \quad (1.6)$$

with  $Q$  the quality factor of the resonant cavity,  $V$  the mode volume of the cavity, and  $\lambda_0/n$  the in-medium emission wavelength of the emitter. The increase in spontaneous emission that results from coupling an emitter to a resonant cavity is called Purcell enhancement.

From Equation 1.6, the Purcell factor can be increased by increasing the Q-factor of the cavity, or by decreasing the mode volume of the cavity. As mentioned in Section 1.1.1, the Q-factor of a metallic cavity is generally very low compared to the Q-factors achievable in cavities made of other materials. However, while dielectric cavity mode volumes are diffraction-limited to approximately  $(\lambda/2n)^3$  [8], metallic cavities can confine an electric field to a substantially smaller volume. Thus, the use of a metallic cavity can still result in a large expected Purcell factor.

In practice, the Purcell factor is actually determined by the more comprehensive equation

$$F_p = \frac{3}{4\pi^2} \left(\frac{\lambda_0}{n}\right)^3 \frac{Q}{V} \cdot \frac{\Delta\omega_0^2}{4(\omega - \omega_0)^2 + \Delta\omega_0^2} \cdot \frac{|\mathbf{E}(\mathbf{r})|^2}{|\mathbf{E}_{\max}|^2} \cdot \left| \frac{\mathbf{d} \cdot \mathbf{E}(\mathbf{r})}{|\mathbf{d}| |\mathbf{E}(\mathbf{r})|} \right|^2, \quad (1.7)$$

with the additional terms describing how well the emitter is matched to the cavity [11]. Any mismatches reduce the Purcell factor, and thus, the expected enhancement of spontaneous emission. Therefore, measured Purcell enhancement falls short of the ideal enhancement predicted by Equation 1.6. Regardless, Purcell enhancement can still be improved by increasing the  $Q/V$  ratio of the cavity.

## 1.2. Definitions of Terms

### 1.2.1 Indium Island Samples

In this dissertation, three indium island samples are primarily analyzed. The naming convention of our group was to combine a brief description of the sample with a number indicating the order in which the samples were grown. Thus, our indium island samples all share the In prefix. The three samples this dissertation focuses on are In38, In44, and In54; the numbers are only a chronological indication, and do not provide further information about the samples. The island growth conditions and SEM images of the samples are provided below.

Table 1.1 Indium island growth parameters.

Sample	Substrate temp. (°C)	Indium temp. (°C)	Arsenic clear time (hours)	Deposition rate	Monolayers of indium
In38	133	830	1.3	0.543 ML/sec	12
In44	131	510	12	1 ML/hour	12
In54	131	510	12	1 ML/hour	36

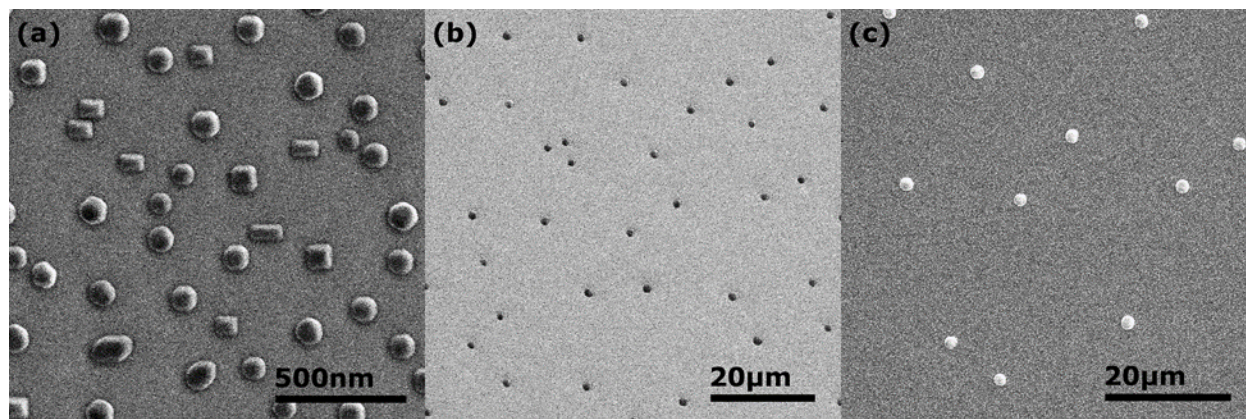


Figure 1.1 SEM images of indium island samples In38 (a), In44 (b), and In54 (c).

In addition to variations in indium deposition rates and quantities, the sample substrates were not identical. The In44 and In54 islands were grown on top of pure GaAs, while In38 consisted of islands grown on top of a  $\sim 10$  nm-thick InGaAs/GaAs quantum well with a  $\sim 5$  nm GaAs cap.

### 1.2.2 Arbitrary Units

Many graphs in this dissertation will use y-axis labels of “counts” or “arbitrary units (a.u.)”. In these cases, the equipment counted the number of times a certain event occurred, such as the number of photons of a certain wavelength captured by a camera, or the number of x-rays of a certain energy captured by a detector. If any processing of the data occurs, such as to convert from counts collected over 10 seconds to counts collected in 1 second, or to subtract a background spectrum, it is technically no longer accurate to use a y-axis label of “counts,” and “a.u.” is used instead.

Regardless of whether “counts” or “a.u.” is used, separate graphs should not be numerically compared unless otherwise stated. Arbitrary units are, indeed, arbitrary, and a value of 400 on one graph does not necessarily relate in any way to a value of 400 on another. Special significance should not be given to negative y-values, as the meaning of the graph is effectively unaltered by adding a constant to every data point. In these graphs, the shape of the line is usually the feature of primary importance.

### 1.3. Layout of Dissertation

This dissertation covers several of the main areas of my research during my time as a graduate student in the Quantum Nano-Optics of Semiconductors group. The primary details and results of these projects have been compiled into a coherent story, with additional data included in the appendices. This dissertation is divided into seven chapters, beginning with an introduction of relevant topics and concepts in Chapter 1 and continuing with a description of the primary methods used in the course of my research in Chapter 2.

Chapter 3 covers my exploration of one-dimensional silicon photonic crystal cavities, determining whether ALD-deposited  $\text{Er}^{3+}$  resulted in a usable gain medium within the cavity and examining the characteristics of the inconsistent presence of an asymmetric cavity resonance lineshape.

Chapters 4, 5, and 6 cover the composition and structure of a few indium island samples. The original characterization project is covered in Chapter 4, and analyses stemming from unexpected preliminary observations are detailed in Chapters 5 and 6. Chapter 4 provides a Transmission Electron Microscopy and Energy Dispersive Spectroscopy examination of the internal composition of islands grown under different conditions. Chapter 5 covers the composition and formation conditions of micrometer-scale hollow domes observed on two indium island samples. Chapter 6 provides characterization of an indium layer observed within the GaAs substrate of two indium island samples.

Chapter 7 summarizes the contributions of this work and proposes directions for further exploration.

## CHAPTER 2: METHODS

In the course of growing and analyzing indium islands, certain standardized sample preparation and data collection techniques were used. These techniques are detailed here for ease of understanding and replication.

### 2.1 Photoluminescence Measurement

Photoluminescence (PL) is the emission of light in response to the absorption of light. When a photon of sufficient energy is absorbed by a structure, an electron can be brought to a higher energy level, and can emit a photon while transitioning to a lower energy level. To measure the PL of a sample, a light source (a laser, in this dissertation) with wavelength shorter than the expected PL spectrum is focused onto the surface of the sample, and the emitted light is directed into a spectrometer. The spectrometer spreads out the PL spectrum by wavelength and a detector records the photon counts at each wavelength.

Because the PL of a sample is generally invisible, both due to its wavelength and relatively low intensity, emitted light is collected by aligning the laser such that the reflected light travels towards the spectrometer. This ensures that any PL following the same path as the source laser will enter the spectrometer. To increase the fraction of emitted light captured by this setup, a high-N.A. microscope objective is used for focusing the laser onto the sample.

Although the wavelength of the source laser should not overlap the PL wavelengths, it is still important to filter out the laser before the light enters the spectrometer. The diffraction grating within the spectrometer is intended to send the first-order diffraction spectrum to the detector, but does not prevent second-order diffraction, which leaves the grating at twice the angle of first-order diffraction. Thus, a bright 633 nm source can create a faint signal at 1266 nm, introducing artifacts into the measured PL spectrum.

Other sources of artifacts include scattered light from the setup and light emitted by other sources in the lab, such as the computer controlling the spectrometer. Some of these artifacts can be reduced or eliminated by first taking a background frame with the source laser blocked; the background spectrum is then subtracted from all frames of the PL measurement. Other artifacts can be reduced by, for example, turning off overhead lights or, for particularly sensitive measurements, turning off the computer monitor.

## **2.2 Molecular Beam Epitaxy**

Molecular Beam Epitaxy (MBE) is a method of growing structures in which materials are deposited one atomic layer at a time. MBE can use a variety of elemental ‘ingredients’, but our specific system focused on III-V materials: indium, arsenic, gallium, aluminum, and phosphorous. Although only indium, arsenic, and gallium were used in the samples analyzed in this thesis, conventional MBE wisdom states that, once an element has been used in an MBE system, it never fully leaves. Thus, all elements used in our system have been listed in case this information turns out to be relevant.

The MBE process begins with a substrate (usually a round wafer of material; undoped (100) GaAs, in the projects described here). This substrate is placed on a holder in the center of the growth chamber. The holder can rotate during growth, which improves the uniformity of material distribution, and can heat the substrate to temperatures exceeding 600°C. The substrate is faced towards the element sources, which, when open, release a fairly-uniform “beam” of gas that condenses onto the substrate.

In the case of a GaAs substrate, the substrate is first held at around 600°C to allow the surface oxide layer to desorb. The growth process then begins with Ga and As sources active. Conveniently, pure As will not grow on the substrate at this temperature; this means that the

precise amount of As released into the chamber is not important, so long as it is sufficient to match the deposition rate of Ga. This GaAs buffer layer is grown to smooth out the surface of the substrate and ensure that the rest of the growth has an ideal foundation to build on.

MBE growth of a 2-D structure is straightforward: simply release elements in the appropriate ratios to build the desired material layer. So long as the chosen materials have sufficiently-similar lattice constants, layers can be grown one atomic layer at a time, almost entirely uniform over the surface of the sample. Quantum wells with precise compositions (say,  $\text{In}_{0.3}\text{Ga}_{0.7}\text{As}/\text{GaAs}$ ) and dimensions (say, 10 nm thick) can be produced in this manner. In general, when working with As-containing materials at temperatures above  $300^\circ\text{C}$ , the As source is active at virtually all times to create an As overpressure that prevents As from diffusing out of the sample [12].

If 3-D structures are desired, the growth process becomes more complicated. The material being deposited must have a lattice constant different enough from the underlying layer that the deposited material will preferentially form localized structures rather than a smooth 2-D layer. In the case of our InAs quantum dots, and probably our indium islands, the growth mode was Stranski-Krastanov [13], meaning that a layer of material one atom thick first formed, followed by small 3-D structures as additional material was deposited on the sample. The rate of material deposition and the temperature of the substrate can control the size and distribution of these 3-D structures.

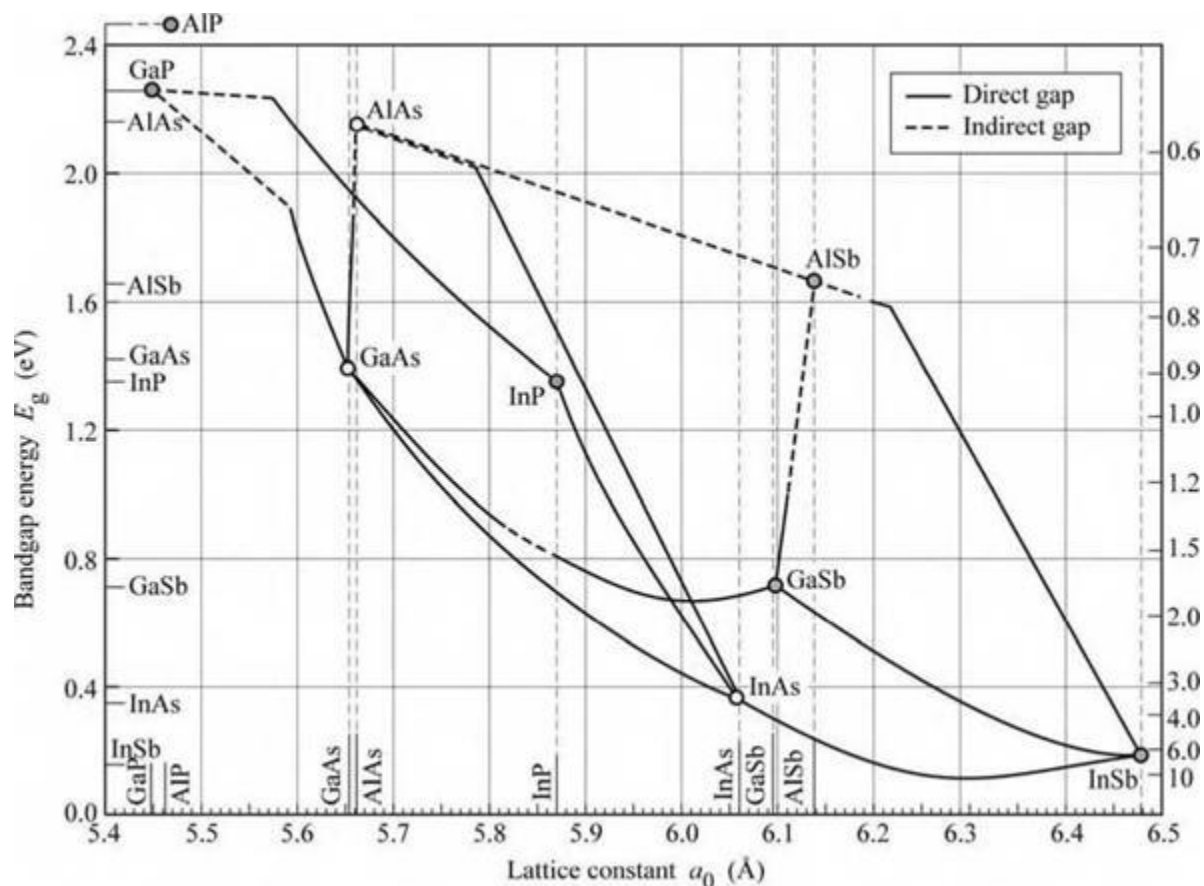


Figure 2.1 Bandgap energies and lattice constants of various III-V semiconductors at room temperature. [14]

To grow islands of pure indium, an As overpressure could not be present. Thus, the substrate temperature needed to be low enough that As would not diffuse out of the material in the absence of additional As. The substrate was held around 130°C for all three of the indium island samples analyzed in this dissertation.

The MBE growth process takes place under very high vacuum ( $<10^{-9}$  torr) to prevent contamination; any residual material is quickly pumped out of the system once an elemental source is turned off. In the case of indium island growth, the growth chamber was held at high vacuum for at least an hour with all sources off to make the environment as free of contaminants as possible.

## 2.3 TEM

Electron microscopy is a set of techniques for imaging samples. In traditional (optical) microscopy, photons are captured from the sample to generate an image. The resolution of optical microscopy is usually limited by the wavelength of the photons, meaning that most optical microscopes cannot resolve features smaller than a couple hundred nanometers. Electrons have a much smaller effective wavelength, which allows electron microscopy to achieve extremely high resolution imaging compared to optical microscopy.

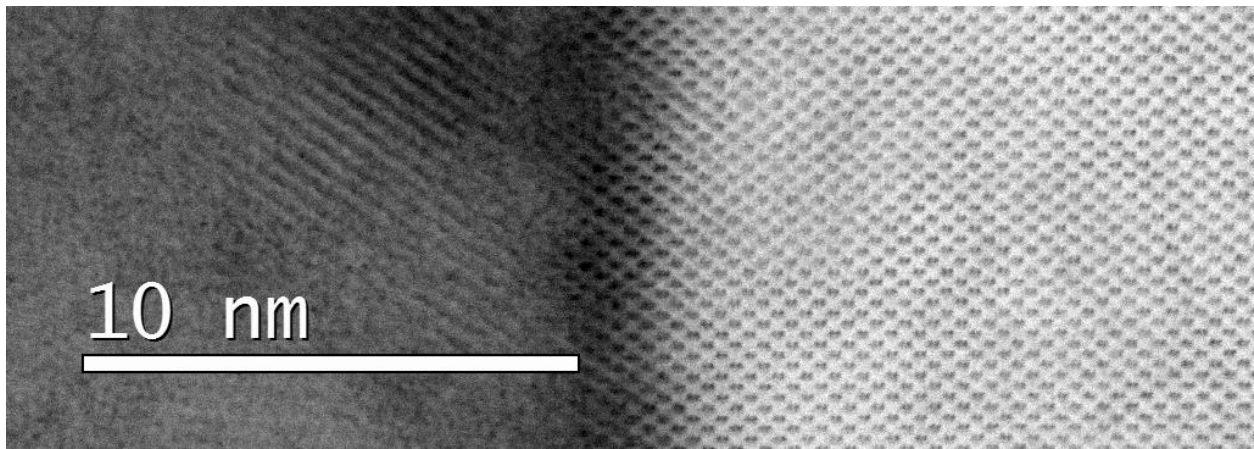


Figure 2.2 A TEM image resolving the different crystal structures of two adjacent materials.

Transmission Electron Microscopy (TEM) creates images of samples by sending a beam of electrons entirely through the sample and using the transmitted electrons to create an image of the sample. Because a sufficient number of electrons must pass through the sample in order to successfully image the sample, TEM samples are generally extremely thin (~100 nm thick) to reduce scattering and absorption. Most objects of interest are much thicker than the ideal TEM sample thickness, so a cross-section of the object is created for TEM imaging.

TEM cross-sections have traditionally been created by encasing the sample in resin or epoxy to prevent damage, and then cutting a thin slice from the encased sample. Part of the slice is then mechanically polished to the desired thickness, usually by creating a small, extremely

thin, 'dimpled' region. This process is slow and can damage temperature-sensitive samples. In addition, the precise location of the thinned region is difficult to control, meaning that a sample prepared in this manner may not contain an indium island cross-section. Because of these issues, the dimpling method of TEM cross-section preparation was not suitable for our samples.

An alternative method of creating TEM-suitable cross-sections is to use a Focused Ion Beam (FIB). In this method, a beam of ions ( $\text{Ga}^+$ , in our case) is used to precisely mill away material (like sandblasting, but with sand grains the size of atomic nuclei). FIBs are often coupled with Scanning Electron Microscopes (SEMs), allowing imaging of the sample before, during, and after the milling process and ensuring that the cross-section contains the exact region of interest.

Although this method of cross-section preparation is better-suited to our samples, a direct ion beam could still be too destructive. To prevent the milling process from damaging or altering the sample, several protective layers are used. First, a thin (~50 nm) layer of carbon, called a conformal coat, is deposited by flowing a hydrocarbon gas over the sample and using the SEM's electron beam to detach carbon atoms from the gas and fix them to the surface of the sample. The electron beam is rastered across a large region of sample, similar to beam movement during imaging. Even a beam of electrons can cause minor damage to the surface of a sample, but the smaller particle size and lower energy make serious damage unlikely.

Next, a platinum-containing gas is flowed over the sample, and the electron beam is rastered across the region of interest to deposit roughly 250 nm-thick platinum over the area that will ultimately become the TEM cross-section. The underlying carbon coat protects the sample from being damaged by the larger platinum atoms, although this electron beam-assisted deposition method is still unlikely to cause serious harm.

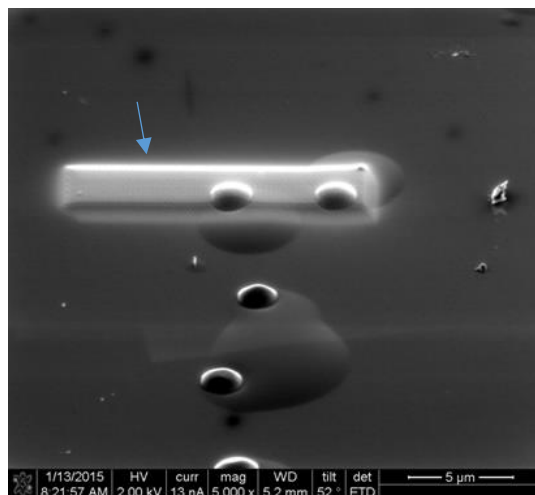


Figure 2.3 In54 after electron-beam deposition of platinum. Arrow points to the deposited platinum.

Finally, a beam of platinum ions is used to deposit a much thicker layer ( $\sim 2 \mu\text{m}$ ) of platinum on top of the original platinum layer. These platinum ions can penetrate roughly 200 nm into the material, so the underlying protective layers must be thick enough to stop the ions before they reach the surface of the sample. As part of preventing sample damage, this final, thick bar of platinum serves as a sacrificial layer, getting milled away by the  $\text{Ga}^+$  ions during the thinning process.

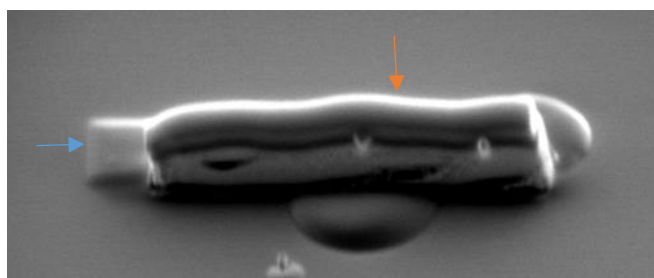


Figure 2.4 In54 after ion-beam-deposited platinum layer. Blue arrow points to electron-beam-deposited platinum, orange arrow points to ion-beam-deposited platinum. The indium islands are no longer visible.

Once the cross-section has been roughly carved out, the piece is transferred to a holder for further thinning. The sample is essentially welded to the holder using the platinum ion beam, and the gallium ion beam is used to continue to shave away material from the faces of the cross-

section. The sample holder used for In38 was made of copper, but after a substantial amount of copper was detected in the islands, molybdenum sample holders were used for In44 and In54.

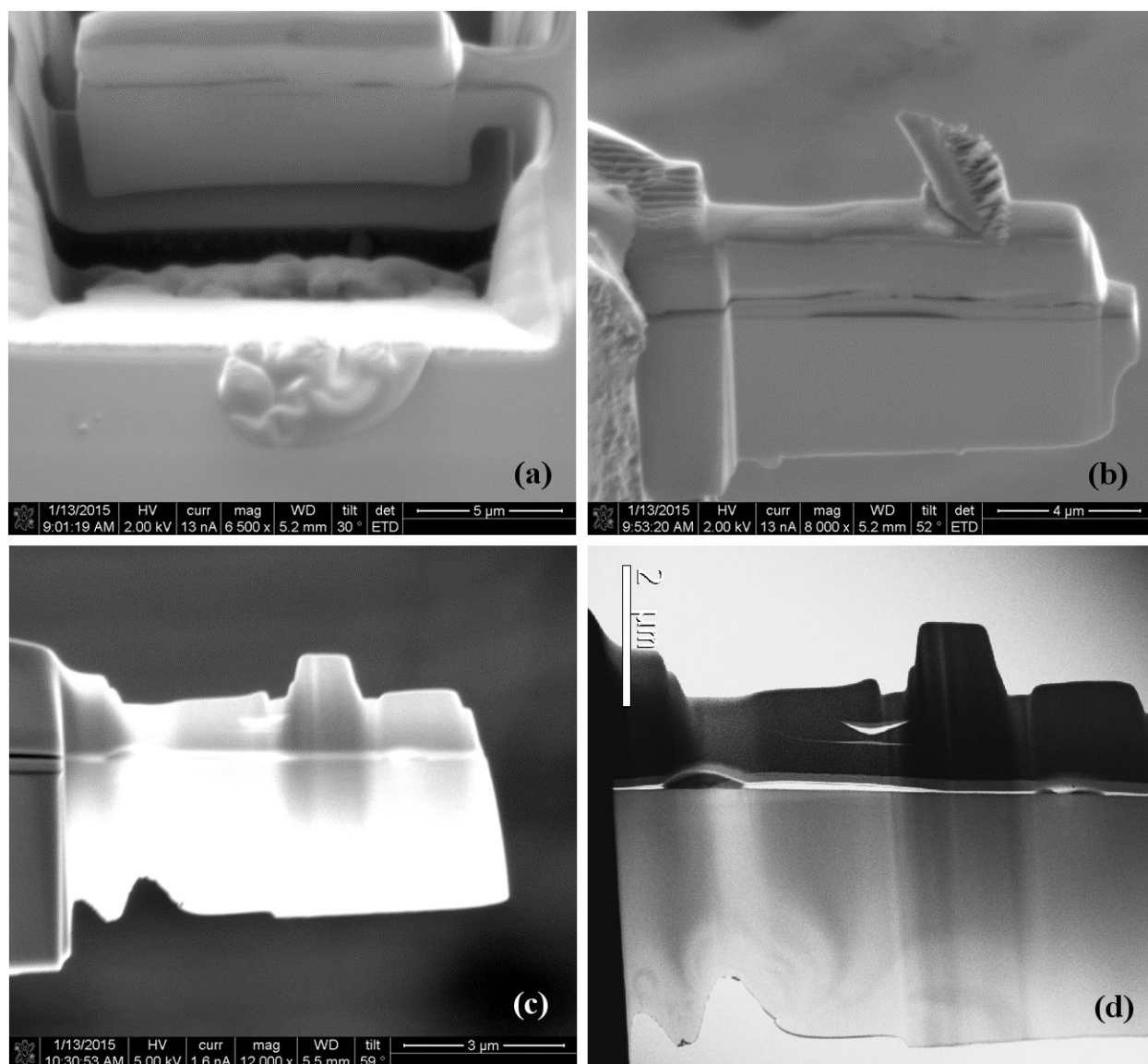


Figure 2.5 (a) SEM image of In54 during the initial cross-section milling. (b) SEM image of In54 cross-section after being attached to the sample holder. (c) In54 cross-section partway through the ion-milling process. (d) TEM image of finished cross-section, around 100 nm thick.

## 2.4 Energy Dispersive Spectroscopy

For determining elemental composition of the islands, potential techniques included Energy Dispersive Spectroscopy, X-ray Photoelectron Spectroscopy, and Electron Energy Loss

Spectroscopy. Conveniently, TEM naturally lends itself to electron-based spectroscopy techniques. Both EDS and EELS could have provided the basic composition information we needed.

EELS provides more detailed information beyond simply the presence of a given element, such as information regarding chemical bonds. This might have been useful in the context of indium islands; being able to differentiate between InGaAs and GaAs suspended in In would have provided important information. However, EELS is less useful when used with elements of a higher atomic number than Zn, which describes all three elements of particular interest. Also, Ga and In have extremely similar characteristic EELS spectra [15]. Overall, EELS is a comparatively finicky technique that requires more time and care to obtain reliable results, and is not particularly well-suited to In/Ga/As analysis.

EDS is a simpler technique that can easily distinguish between the main elements of interest in our samples (In, Ga, and As) and can provide some quantitative information. For our purposes, the amount of information gleaned through EDS was sufficient to determine the typical purity and general composition of indium islands, and so we opted to use EDS analysis and not EELS.

When an electron passes through a material, it can interact with an inner-shell electron of an atom, ejecting the atom's electron and causing a higher-energy electron to drop down into the resulting hole. This reshuffling causes an x-ray to be emitted, with the energy of the x-ray determined by the source atom and its orbitals. Each element has a characteristic x-ray spectrum, allowing the presence or absence of specific elements to be determined by capturing the emitted x-rays. Some elements have close or overlapping spectra, but context (such as the knowledge that iron should not be present in the sample) can help in interpreting results.

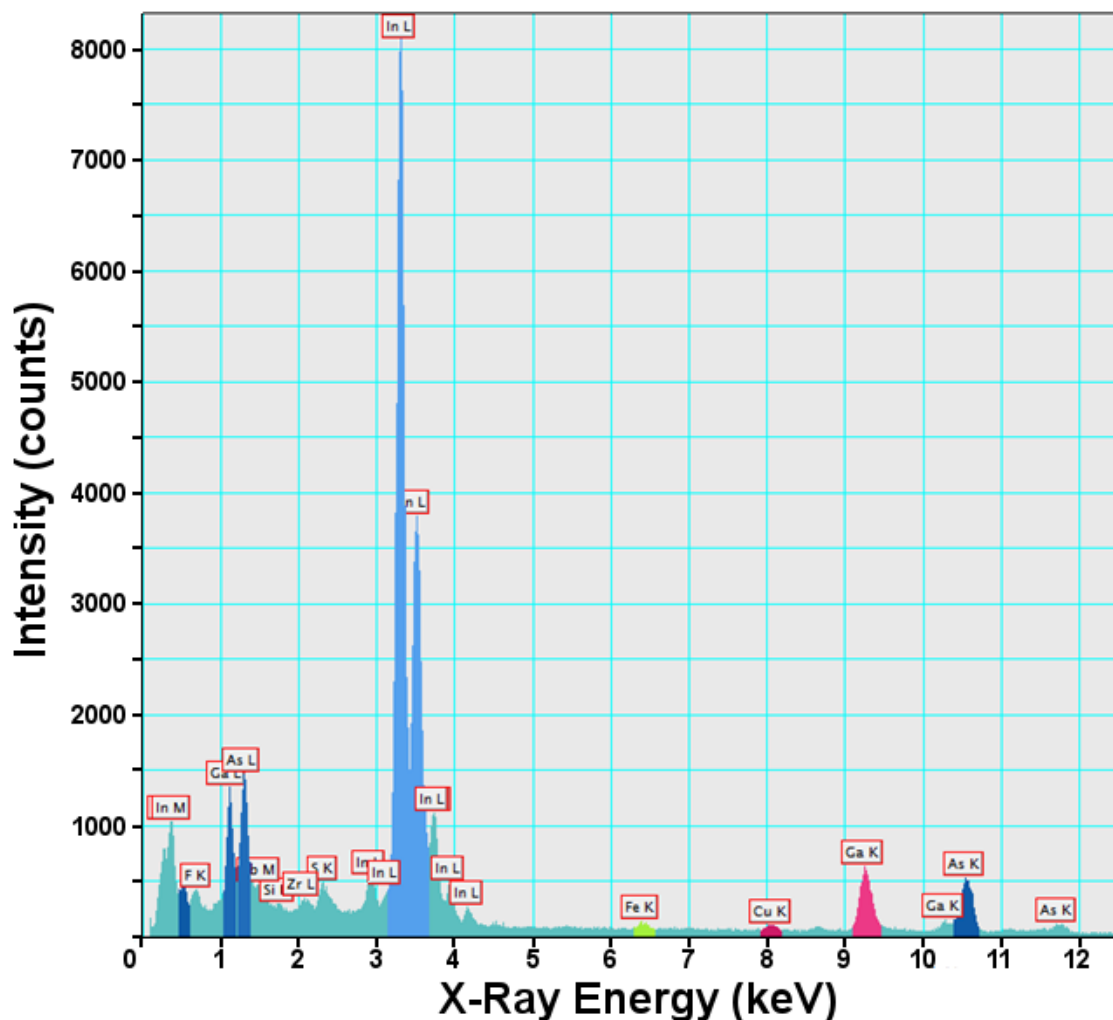


Figure 2.6 An example EDS spectrum after using the software’s “auto-identify peaks” function. The colored peaks indicate which spectral regions are actually being used in the analysis.

Energy Dispersive Spectroscopy (EDS) can be performed in both TEMs and SEMs, provided they contain the necessary x-ray detectors. However, in electron microscopy, the incident electrons interact with a significant volume of material; in a thick sample, x-rays will be generated from a very large region compared to the spot size of the electron beam. Fortunately, the thin samples required for TEM allow high-resolution EDS to be performed on TEM samples.

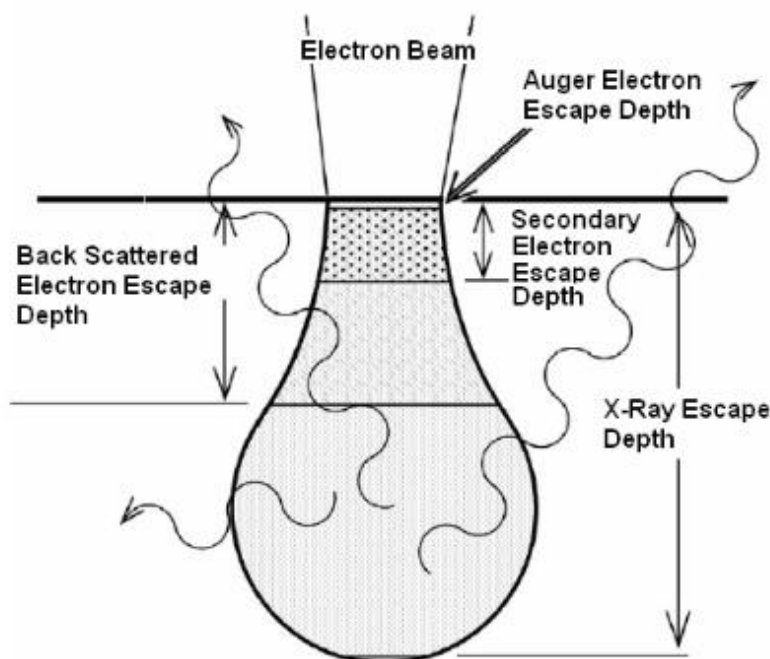


Figure 2.7 Illustration of the total volume of x-ray generation from a stationary electron beam. The precise dimensions of this bulb shape depend on the characteristics of the material. [16]

In the case of a thin sample, the spatial resolution of EDS is limited by the spot size of the electron beam, usually around 1.5 nm. However, the time required to complete a scan increases with the number of points being measured, and so the chosen resolution is often lower than the maximum-achievable resolution due to time constraints. The resolution of our indium island measurements ranged from 2-5 nm.

Three main types of EDS analysis were used on our indium island samples: spot, line, and area mapping. In spot EDS, the electron beam is kept stationary during x-ray collection. The resulting x-ray spectrum can then be used to determine the relative percentages of several elements in the region covered by the electron beam. The electron beam can be focused to a narrow spot or expanded to cover a substantial area of the sample (in which case, the results will be an average over the area). Of the three EDS analyses, spot EDS is most reliant on careful calibration to return accurate results.

Ele...	Cl...	(keV)	Counts	Mass%	Error%	Atom%	Comp...	Mass%	Cation	K
O	K	0.525	480.29	1.68	0.03	10.71				0.4903
Ga	L	1.098	208.06	1.89	0.13	2.77				1.2745
As	L*	1.282	171.06	1.42	0.17	1.94				1.1654
In	L	Ref.	13354.21	95.02	0.00	84.59				1.0000
Total				100.00		100.00				

Figure 2.8 Software readout of quantitative EDS results from In44 island 1.

In line EDS, the electron beam is focused to a narrow spot and moved in fixed increments across the sample, following a predetermined path. X-ray spectra are captured at each point along the path, and these spectra are used to plot intensity vs. distance lines for each element of interest. It should be emphasized that these plots only provide qualitative information regarding the amount of a given element at a given point on the sample, and cannot be used to compare relative quantities of different elements.

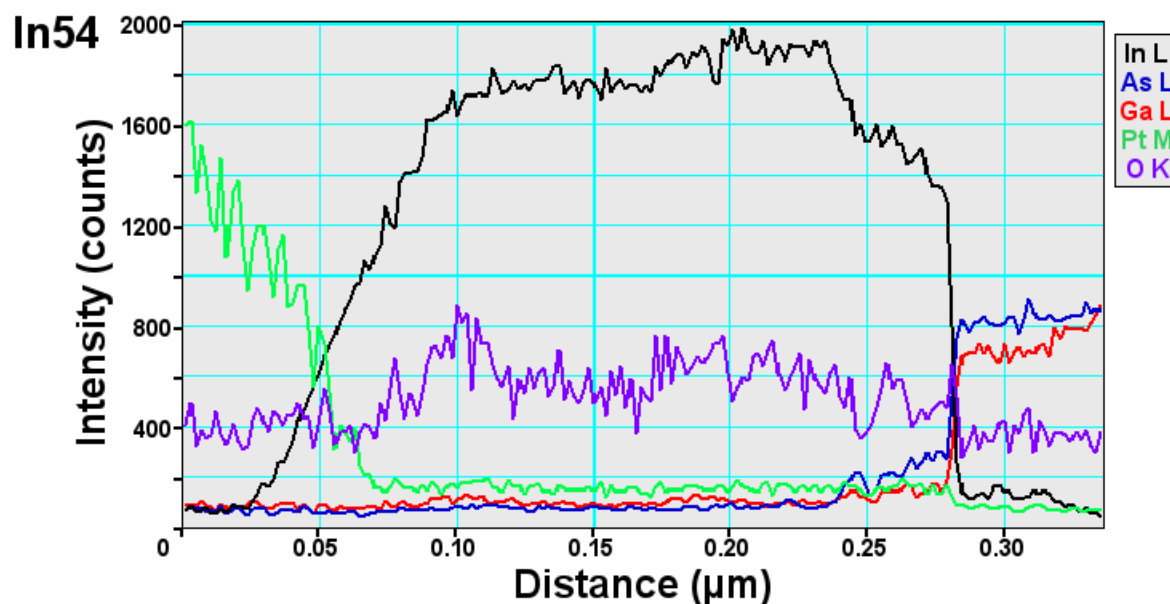


Figure 2.9 EDS line scan of In54.

In area mapping, the electron beam is again focused to a narrow spot and moved in fixed increments; however, unlike in line EDS, the beam travels over a 2-D region of the sample, generating x-ray spectra from a grid of points. One map is then generated for each element of interest, with each pixel in the map showing the relative intensity of that element's x-ray

spectrum at that point. To aid in analysis and visualization, these maps can be color-coded and overlaid to create a single elemental composition map. Area mapping is also a qualitative technique, and information regarding relative quantities of different elements cannot be inferred.

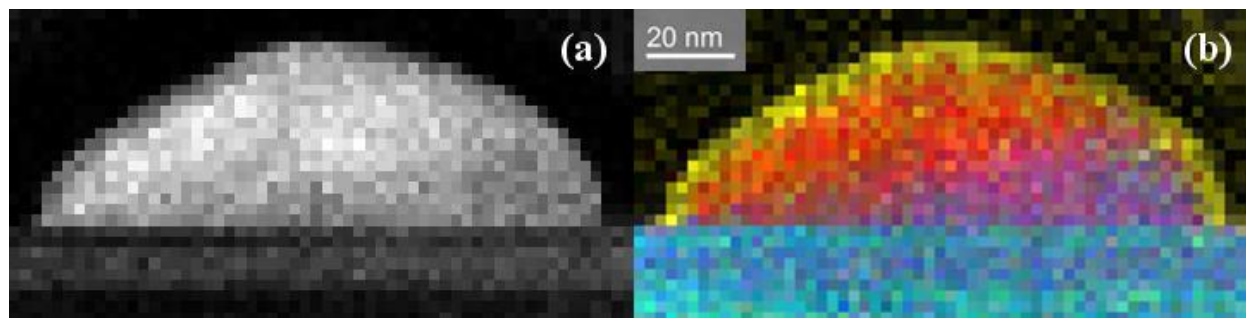


Figure 2.10 (a) EDS area map of In38 island 1 (indium only). (b) Composite EDS area map of In38 island 1 (In, Ga, As, O).

Certain steps can be taken to improve the quality or reliability of EDS measurements. For example, when generating quantitative results from spot EDS, peaks from the same orbital of each element of interest should be used when possible. Thus, when measuring the relative percentages of In, Ga, and As, the L peaks of all three elements should be used, rather than the indium L peak and the Ga and As K peaks. The EDS software provides error estimates, but these estimates seem to assume the equipment is perfectly calibrated; taking a measurement of a material of known composition, such as GaAs, allows for a better estimate of the calibration error. Also, if the spot size of the electron beam is smaller than the step size, the beam can be rastered across the pixel area defined by the step size in order to collect x-rays from the entire pixel. This results in a more-accurate representation of the composition of the pixel, rather than attributing the results of a smaller region to the entire pixel.

## CHAPTER 3: SILICON NANOBEAMS

### 3.1 Motivation

Silicon is easily the most common semiconductor in device fabrication, largely due to its low cost and convenient insulating oxide. Unfortunately, silicon's indirect bandgap makes on-chip light sources difficult to fabricate, as silicon alone cannot act as an active emitter. A simple method for creating on-chip light sources would make the transition from electronic chips to photonic chips more feasible [17], potentially increasing computation speeds and bandwidth dramatically [18].

Using electron-beam lithography, the surface of a silicon wafer can be formed into extremely precise structures. One such structure, a tapered nanobeam, was of interest in pursuing a method for fabricating an on-chip light source. These nanobeams consist of a long bar of silicon ( $\sim 10\ \mu\text{m}$  long and  $\sim 500\ \text{nm}$  wide) with a line of circular holes ( $\sim 200\ \text{nm}$  in diameter) running the length of the bar. The spacing and diameter of the holes decrease ("taper") towards the center of the bar. This nanobeam design results in a 1-D photonic crystal. The nanobeams for this project were fabricated by the Scherer group at Caltech.

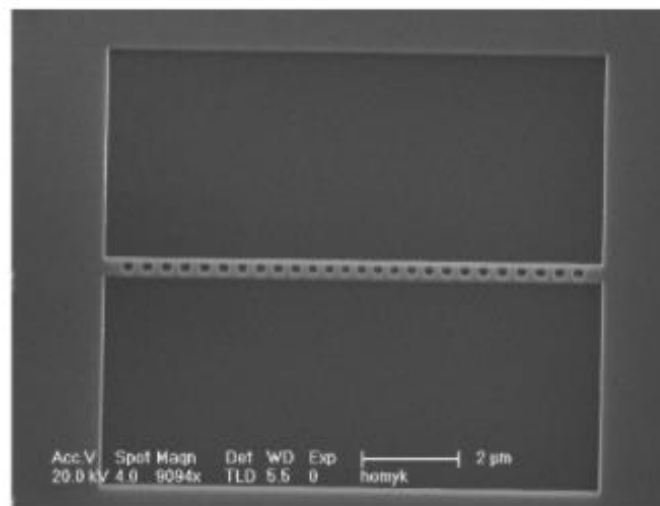


Figure 3.1 SEM image of a silicon nanobeam. Image credit: Andrew Homyk

Light traveling through one of these nanobeams does not, effectively, “see” a bar with a series of empty holes. Instead, propagating light interacts with the nanobeam as though it were a gradually-varying crystal lattice structure. At certain combinations of hole spacing and diameter, the corresponding effective crystal lattice behaves as a mirror for some wavelengths of light. Thus, for a certain range of wavelengths, the nanobeam structure can be treated as a resonant cavity with mirrors on either end. By choosing the appropriate hole size and spacing throughout the nanobeam, the resonant wavelength of the nanobeam can be precisely selected.

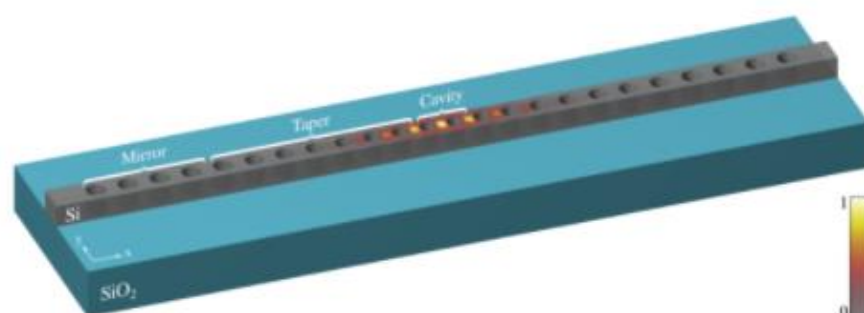


Figure 3.2 Diagram of a silicon nanobeam with simulated electric field energy density. [19]

Our original goal was to incorporate an active emitter into a silicon nanobeam in order to turn the nanobeam into an on-chip laser cavity, which will be discussed in Section 3.2. In the process of measuring the resonant wavelengths of some silicon nanobeams, an unexpected transmission lineshape was observed and investigated. This phenomenon and related applications will be discussed in Section 3.3.

### 3.2 Erbium Doping

We selected erbium as the active emitter to incorporate into our silicon nanobeams due to erbium’s emission spectrum, which peaks around 1550 nm. This is a popular wavelength for telecommunications because light at this wavelength experiences very little attenuation while propagating through silica optical fiber [20]. Erbium is already used as an active emitter in

fiberoptic devices such as optical amplifiers [21] and fiber lasers [22], making it a promising choice of active emitter for our silicon nanobeam cavities.

In order to maximize the interaction between the propagating light and active emitter, we wanted to deposit erbium inside the holes of the nanobeams. (Our first choice would have been to incorporate erbium directly into the silicon of the nanobeams, but this was outside our capabilities.) Atomic Layer Deposition (ALD), a technique for depositing conformal coatings, seemed like a good method of erbium incorporation. Our collaborators at Aalto University in Finland performed the ALD for this project.

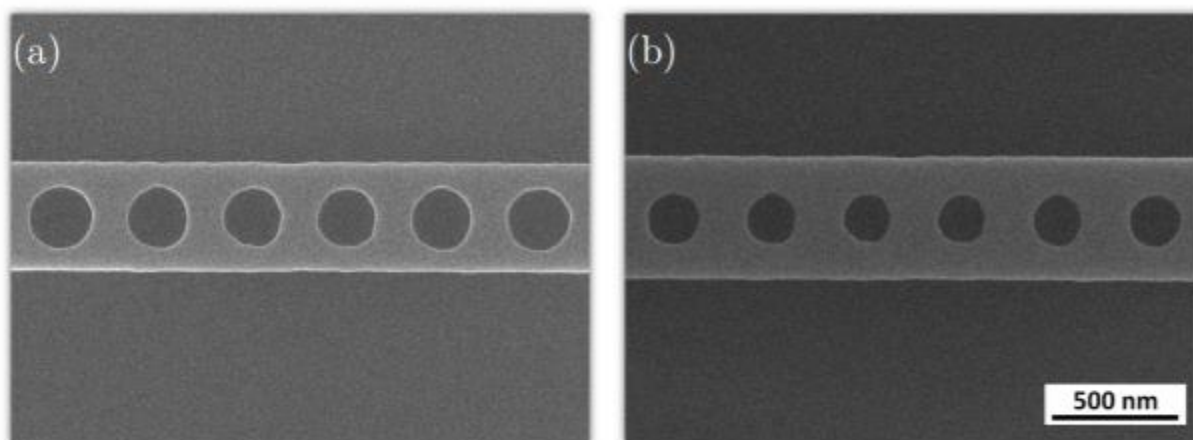


Figure 3.3 (a) SEM image of silicon nanobeam prior to ALD coating. (b) Silicon nanobeam after ALD coating with 20 nm of  $\text{Al}_2\text{O}_3$ .

We chose to deposit erbium between layers of  $\text{Al}_2\text{O}_3$  during ALD, due to a successful example in the literature of erbium-doped  $\text{Al}_2\text{O}_3$  resulting in 1530 nm emission [23]. Prior work in this lab explored the impact of ALD-deposited  $\text{Al}_2\text{O}_3$  on silicon nanobeams and found that, on average, ALD introduced a slight shift in resonant wavelength ( $\sim 30$  nm decrease) and improved the Q-factor of the cavities ( $\sim 30\%$  increase) [24]. Thus, we did not expect this method of erbium incorporation to negatively impact the performance of the nanobeams.

To test whether the incorporated erbium was functioning as an active emitter, photoluminescence measurements were taken using a 980 nm diode laser. This initial

measurement was simply to check whether any erbium emission could be observed, and so the PL measurements were taken on parts of the sample where nanobeams were not present. The entire sample underwent erbium-containing ALD, and so erbium should have been present across the surface of the sample.

Unfortunately, no erbium emission was observed from the sample. The collaborators who performed the ALD process mentioned that the deposited erbium layer was very thin, which might have resulted in insufficient erbium content for PL detection. It is also possible that too much erbium was incorporated, resulting in a lack of ~1500 nm emission due to erbium's self-quenching properties [25]. Due to difficulties with the ALD setup, the precise concentration of erbium in the ALD coating was unknown.

Another possibility was that much of the erbium may have formed as large domains of  $\text{Er}_2\text{O}_3$  rather than isolated erbium ions doping the deposited  $\text{Al}_2\text{O}_3$ ;  $\text{Er}_2\text{O}_3$  has a substantially different emission spectrum from  $\text{Er}^{3+}$  [26]. However, expanding the PL measurement range to include visible wavelengths did not reveal any new emission peaks.

Subsequent simulations indicated that, even if  $\text{Er}^{3+}$  were successfully incorporated via ALD as an active emitter, the electric field in the silicon nanobeam would not substantially interact with erbium coating the surface [12]. These results caused us to abandon this project rather than continuing to troubleshoot the absence of erbium emission.

Although we ultimately concluded that our sample showed no erbium emission, a PL spectrum was recorded that suggested the presence of PL at 1555 nm. This measurement was a good illustration of the importance of checking for false positives; the observed peak turned out to be an artifact from the filters used to eliminate the 980 nm pump laser from the PL measurements.

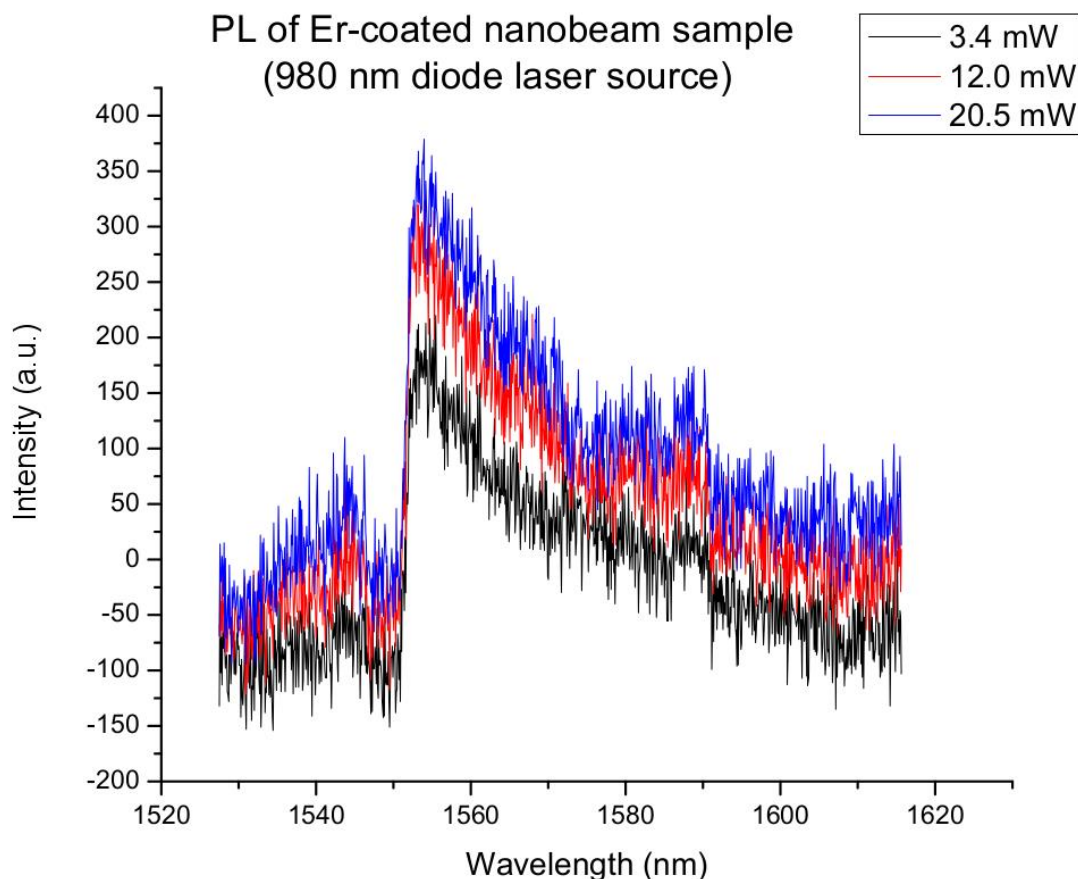


Figure 3.4 Spectrum from nanobeam sample coated with erbium-containing ALD. The primary peak is an artifact of the 980 nm pump laser. The smaller peaks around 1540 and 1585 are scattered light artifacts.

The odd shape of the peak - PL spectra do not usually exhibit such sharp cut-offs - resembled the shape of a laser spectrum incompletely blocked by a long pass filter. As mentioned in Chapter 2, the PL measurement setup requires a filter to prevent the pump laser from creating artifacts in PL spectra. In this particular setup, a single filter was insufficient; the Semrock 1064 blocked the majority of the pump laser, but exhibited transmission peaks around 700 nm, so an RG850 filter was added to block these peaks. However, the RG850 filter begins to have non-negligible transmission around 750 nm. It seemed possible that the observed peak was the second-order diffraction result of the RG850 filter incompletely blocking a transmission peak through the Semrock 1064 filter.

In order to check whether the “emission” was actually an artifact of the laser, the Semrock 1064 filter was tilted slightly to change the laser’s angle of incidence. The PL measurement was then re-taken, and the peak wavelength was observed to have changed in intensity. Changing the angle of an interference filter (such as the Semrock 1064) with respect to an incident laser beam shifts the cut-off frequency of the filter, also shifting the wavelengths of the transmission peaks. The cut-off of the RG850 (a colored glass filter) remained unchanged, but the portion of the transmitted peak blocked by this second filter changed due to the wavelength shift, changing the height of the resulting second-order spectroscopy peak.

This observed change indicated that the peak was the result of the pump laser and filters. Because erbium emits at wavelengths far longer than the cut-off wavelengths of the filters, tilting the interference filter would not have changed the measured spectrum if the peak were actually the result of erbium emission.

### **3.3 Fano Resonance**

Fano resonance is a mathematical way of describing a coupled-oscillator system in which one oscillator is strongly damped (non-resonant) and the other has very little damping (resonant) [27]. This type of system is characterized by a particular pattern of asymmetric lineshapes, in contrast to the nearly-symmetric peaks produced by systems that can be described as a single oscillator. Understanding whether a system exhibits Fano resonance can vastly reduce the amount of computation time required to create an accurate model of the system [28].

While measuring the resonances of silicon nanobeams, a lineshape indicative of Fano resonance sometimes appeared. After exploring how this lineshape depended on the choice of experimental parameters, we determined that certain measurement configurations led to Fano

resonance, likely between the silicon slab and the nanobeam cavity. A Fano-Lorentz lineshape, described by

$$T(\varepsilon) = A \left( \frac{\eta(\delta + \varepsilon)^2}{1 + \varepsilon^2} + \frac{1 - \eta}{1 + \varepsilon^2} \right), \quad (3.1)$$

[29] was fit to the experimental data, confirming that our system was well-described by this model. In this equation,  $\eta$  is a weighting parameter describing the relative contributions of the Fano and Lorentzian lineshapes,  $\varepsilon$  relates to the scaled energies of the system, and  $\delta$  is an asymmetry factor.

A fiber taper setup was used to measure the wavelength and Q-factor of the silicon nanobeam resonances. The fiber taper was created by heating and stretching an optical fiber (SMF-28) to create a thin ( $\sim 1 \mu\text{m}$  diameter), curved region. In this tapered region, it is easy to couple to the evanescent field of light passing through the fiber, allowing light to be extracted from the fiber by bringing the fiber in contact with a resonant cavity. Some tapers were created by Yong-Hee Lee's group at KAIST, and others were created by Professor Khan Kieu at the University of Arizona.

The tapered region of fiber was brought into contact with the nanobeam, light of varying wavelengths was run through the fiber, and the light exiting the fiber was captured by a photodetector. The change in transmission at each wavelength between the fiber when in free space and the fiber when in contact with the nanobeam was then graphed.

The measurement setup was composed of a tunable telecommunications-wavelength laser (Agilent 81682A, 0.2pm wavelength resolution), a paddle polarizer (for changing the polarization of the light in the fiber), a fiber taper mounted on an X/Y/Z stage, a collimator and linear polarizer (for measuring the output polarization), and a photodetector. The collimator and

linear polarizer could be bypassed, allowing the output of the fiber to be connected directly to the photodetector when desired.

On samples exhibiting Fano-type lineshapes, changing the input polarization of the light changed the shape of the transmission dip. The paddle polarizer was set up such that the polarization of the light in the fiber could easily be rotated through different linear polarization angles, rather than through different elliptical polarization states. Because measuring the polarization at the nanobeam was essentially impossible, the polarization at the output of the fiber was measured instead. On a single nanobeam, the output polarization was linearized and rotated through  $90^\circ$  in  $5^\circ$  steps. The resulting data matched the predictions of the Fano-Lorentz lineshape model. (Additional data can be found in Appendix A.)

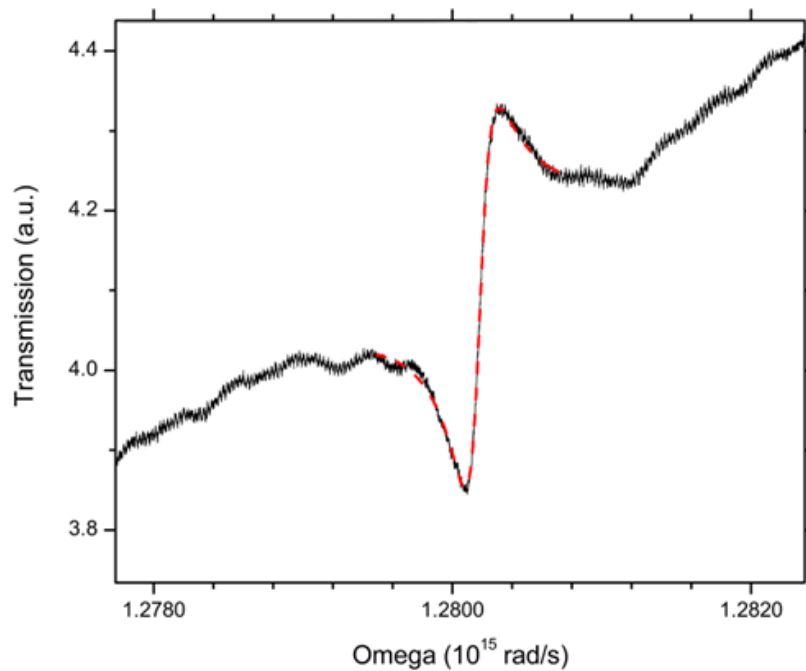


Figure 3.5 Nanobeam resonance data (black) overlaid with a Fano-Lorentz fit (red). The fitting parameters were  $\eta = 0.506$  and  $\delta = 0.055$ . [29]

It should be noted that a symmetric dip was not observed in this  $90^\circ$  polarization range, although symmetric lineshapes are predicted by the Fano-Lorentz lineshape equation. The most likely explanation is that the input polarization conditions that resulted in linear output

polarization actually resulted in elliptical polarization at the nanobeam, with linear polarization at the nanobeam being required for symmetric lineshapes. The failure to adjust the input polarization until a symmetric dip was achieved was an unfortunate oversight.

One observation made during the course of these measurements was that only certain fiber tapers seemed to result in a Fano-type lineshape; measurements made with other, similar fiber tapers produced symmetric transmission dips regardless of input polarization. We determined that, in the fiber tapers that exhibited Fano resonance, the fiber was shaped such that it was simultaneously in contact with the silicon slab (likely the non-resonant component) and the nanobeam (resonant).

This characterization of our nanobeam resonance measurement setup explained the occasional asymmetric lineshapes we had observed, and also allowed said asymmetric lineshapes to easily be mathematically described. In general, the presence of Fano resonance is counterproductive to an accurate measurement of the cavity Q-factor, due to the difficulty in defining and measuring the full-width-half-max parameter of an asymmetric dip. This fitting equation allows the resonance and Q-factor of a nanobeam cavity to be determined more accurately than previously.

## CHAPTER 4: TEM EDS ANALYSIS OF SELF-ASSEMBLED INDIUM ISLANDS

### 4.1 Motivation

Our group developed the self-assembled indium island MBE growth process while looking for an alternative to the silver nanoantennas we had been fabricating via e-beam lithography and evaporation. These silver nanoantennas were designed to convert incident visible light into a localized electromagnetic field, which could then be used to enhance the photoluminescence of an underlying quantum structure [30]. Indium has been identified as an alternative plasmonic material to silver for visible and near-visible wavelengths [31][32], and so seemed worth exploring as a nanoantenna material for our applications.

Although the silver nanoantennas usually performed acceptably, the fabrication facilities were completely separate from the MBE used to grow the underlying quantum structures, causing fabrication delays and increasing the potential for contamination. In addition, the e-beam lithography exposure step took a painfully long time per antenna and some nanoantennas were observed detaching from the substrate after fabrication. Epitaxially-grown silver has exhibited improved optical characteristics compared to evaporated silver (the deposition method used in our lithography process) [33], indicating that fabricating nanoantennas as part of an uninterrupted MBE growth process might eliminate the lithography-related inconveniences and improve the performance of our structures. Our MBE system is not equipped to deposit silver, but is capable of indium deposition.

MBE typically results in a series of 2-D sheets or slabs of material. As described in Chapter 2, near-uniform layers of material are deposited on the substrate. In the absence of other effects, MBE-grown structures should be practically unchanging along two dimensions, only

varying in composition along the direction of growth. Many types of structures, such as quantum wells and distributed Bragg reflectors, can be entirely constructed by stacking layers of different materials; the MBE process is well-suited to producing full wafers of these structures.

However, quantum dots, tiny specks of one material embedded in a different material with a higher bandgap, have also long been grown via MBE. If two materials have substantially different lattice constants, as in the case of GaAs ( $\sim 5.65$  Å) and InAs ( $\sim 6.05$  Å), it can be more energetically favorable for the deposited material to form into blobs rather than remaining as a uniform 2-D sheet over the substrate material. InAs quantum dots can quickly and easily be grown on a GaAs substrate using this phenomenon. Thus, MBE can be used to fabricate 3-D structures despite only depositing uniform layers of material.

3-D pure indium structures can be grown via MBE in a process similar to quantum dot growth. Like InAs, the lattice constant of pure indium is substantially different from that of GaAs. Thus, by depositing indium onto a GaAs substrate without the presence of arsenic, indium islands are formed. These islands can be similar in shape to the square silver nanoantennas previously fabricated by our group (the islands can also take a rounder or more pyramidal shape). The island shapes and metallic properties of indium led us to anticipate nanoantenna behavior from the islands.

In theory, the MBE process controls the composition of the sample down to the atomic layer. If only pure indium is deposited, the islands would ideally be composed only of indium. However, in practice, trace amounts of other elements are often present in a given layer. In the case of arsenic-containing materials in particular, growths are usually performed with a constant arsenic pressure in the growth chamber to prevent arsenic from diffusing out of the substrate, as it would in vacuum at the substrate temperatures normally used. Obviously, a

constant arsenic pressure would make pure indium deposition impossible, and so the growth process needed to be adjusted to account for this restriction.

The modified growth procedure involved keeping an arsenic overpressure in the chamber while the GaAs substrate was cooled to a temperature that should result in minimal arsenic diffusion ( $\sim 300^\circ\text{C}$ ). Once the substrate reached the desired temperature, the arsenic was turned off and the growth chamber was pumped out to remove any residual arsenic. Only after this step was indium released into the growth chamber. Although this procedure was designed to avoid contamination of the indium islands, there was still the potential for undesired elements to become incorporated within the indium.

While pure indium is metallic, the indium-containing compounds that were likely to appear in our indium islands - InAs and InGaAs - are both semiconductors. Our predictions of nanoantenna behavior were based on the assumption of a metallic nanostructure; the presence of semiconducting material would change the expected behavior of our islands. For the purposes of modeling the interactions between these islands and quantum structures, it was important to understand what the islands were actually composed of.

The purity of our indium islands was of particular interest because indium is superconducting at achievable temperatures ( $\sim 3.41\text{K}$ ). For comparison, aluminum becomes superconducting at much lower temperatures ( $\sim 1.175\text{K}$ ), and other metals typically used in device fabrication (copper, silver, gold) do not exhibit superconductivity at any achievable temperature. Semiconductors cannot superconduct; if compounds other than pure indium were present in substantial quantities, the islands would be unlikely to exhibit superconductivity.

A potential application of superconducting indium islands lies in quantum computing: Majorana fermions are a type of synthetic particle predicted to be useful in constructing qubits.

One method of creating Majorana fermions is to place an s-wave superconductor in close proximity to a 1-D semiconductor [34][35]. Indium and indium arsenide have been identified as a potentially-compatible superconductor/semiconductor pair [36][37], and this combination of materials would be easily grown via MBE if our indium islands can superconduct.

The knowledge of how to grow superconducting indium islands could also be useful in the context of single-photon detectors. When a low-temperature superconducting structure absorbs a photon, the increase in temperature destroys the superconducting state. The corresponding increase in resistance indicates the detection of a photon [38]. A method of fabricating an array of superconducting structures could allow for single-photon detectors with greater spatial sensitivity.

To better understand the potential applications and limitations of our indium islands, an examination of their elemental composition and atomic structure was necessary. We chose to use Transmission Electron Microscopy and Energy Dispersive Spectroscopy to carry out this analysis. TEM allows for internal examination of the islands instead of the surface examination that other forms of microscopy perform. This ability was important to give us an understanding of how homogeneous the islands were.

We initially considered removing islands from the substrate and analyzing them using a destructive spectroscopy method to determine the presence or absence of other elements. However, the removal process seemed likely to introduce contamination of its own (the islands did not easily detach from the substrate), and most contextual information, such as whether impurities were mostly present along the island-substrate interface, would be lost.

In addition, one of our goals was to couple these islands to underlying quantum structures, such as wells or dots. Due to the growth process, it was possible that the island growth

would interfere with the elemental ratios necessary for dots and wells. Thus, we chose an analysis technique that kept as much contextual information intact as possible and would allow us to simultaneously determine the impact of island growth on underlying quantum structures.

TEM can easily achieve extremely high resolution, allowing for observation of the crystal structure of the materials involved. Although this is theoretically possible with a few other types of microscopy, such as AFM and STM, TEM was more readily available and easier to use for this application. TEM has been used to examine embedded quantum dots in more detail [39], further suggesting that TEM is well-suited for analysis of indium islands.

Energy Dispersive Spectroscopy can be performed using an SEM instead of a TEM, but only has the desired spatial resolution when used with extremely thin samples. Thus, TEM EDS was the best combination of structural and compositional tools available to us, and was used to analyze three different indium island samples. These island samples were chosen based on growth parameters and resulting island sizes in order to provide a broad understanding of indium island structures in general.

Many of the results of this investigation were published as Reference [40], which has been included as Appendix B of this dissertation.

## **4.2 TEM Results**

Low-magnification images were obtained of each cross-section slice, and higher-magnification images were taken of each island of interest within each slice. On each sample, the GaAs substrate was examined at high enough magnification to observe the characteristic “dumbbell” pattern, verifying that the expected crystal structure was present.

Upon close examination of the islands, a pattern indicative of indium’s face-centered tetragonal structure was observed in the larger islands, but a pattern indicative of the InGaAs

zinc blende structure was observed throughout the In38 islands and in localized regions of the In54 island. However, these images only show the crystal structure of the island at the very surface of the cross-section slice, and so do not give significant information about the crystal structure or purity of the island throughout the entire ~100 nm-thick cross-section.

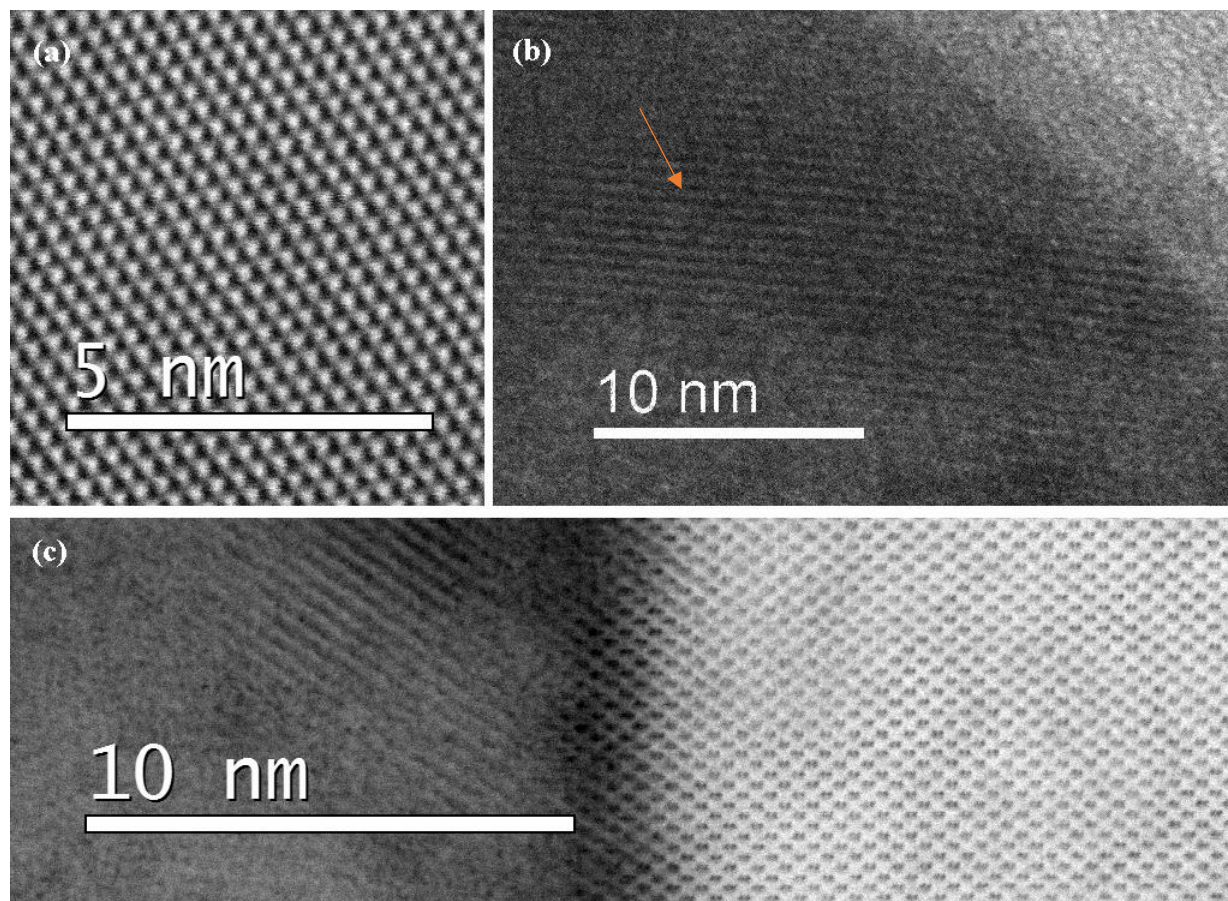


Figure 4.1 (a) Indium crystal structure in In54. (b) Probable zinc-blende structure in In38. (c) Probable zinc-blende structure (left) adjacent to GaAs crystal structure (right) in In54.

Some islands exhibited regions of different shades on the TEM images. For example, the InGaAs well beneath the In38 islands was a noticeably different shade of gray from the GaAs cap and substrate, making the well easily visible in the small island pictures. Although some neighboring regions of different shades did turn out to contain different elements, a change in color does not necessarily indicate a change in composition; these TEM images simply depict the transmission through each part of the sample. In the case of the large island, the different-colored

regions near the substrate were determined to partly be regions of indium with crystal planes oriented in different directions, and partly be regions of InGaAs. In the case of the low-magnification sample images, the bright and dark curves beneath the islands are due to slight changes in thickness and curvature introduced during the milling process.

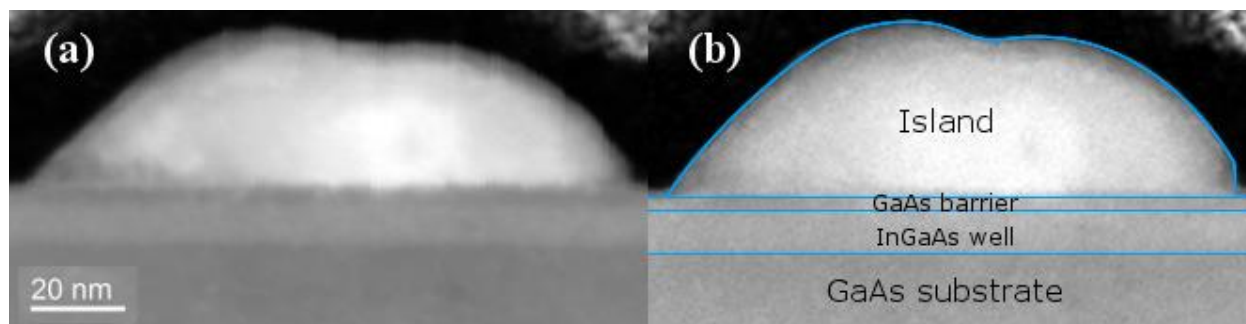


Figure 4.2 (a) A TEM image of In38 Island 2; the different substrate layers are clearly visible. (b) An image of the same island with the different regions outlined and labeled.

One important observation was that, with one exception, all islands captured in a cross-section survived the milling process. TEM analysis was initially attempted by a collaborator in Germany, but the group reported that ion milling usually caused the islands to melt away. In our samples, one large island did seem to largely vanish during cross-section preparation, but the other large island on the same sample seemed unaffected.

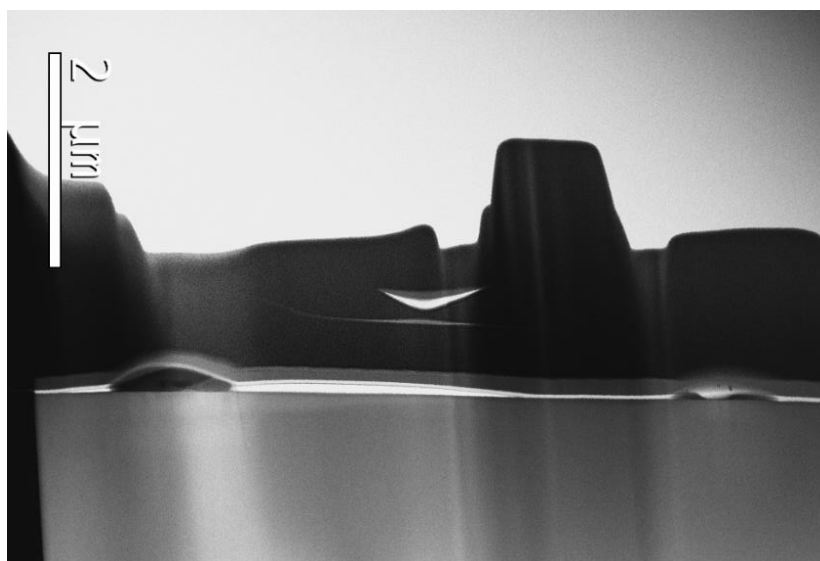


Figure 4.3 Low-magnification TEM image of In54. Two islands were captured in the cross-section, but the right-hand island seemed to disappear during the milling step.

We were unable to determine why the TEM samples in Arizona turned out so much better than the samples in Germany; similar islands were examined by both groups, and similar cross-section creation processes were used. It appears that the protective carbon layer was thinner in the samples prepared in Germany, but precise data was not available.

### 4.3 EDS Results

Overall, the small islands had substantially higher levels of non-indium elements than the larger islands. All islands had a thin, oxygen-rich outer shell. The majority of the substrate was almost entirely pure GaAs, and the quantum well present beneath the small islands was clearly visible from EDS measurements. Additional EDS data is included in Appendix C.

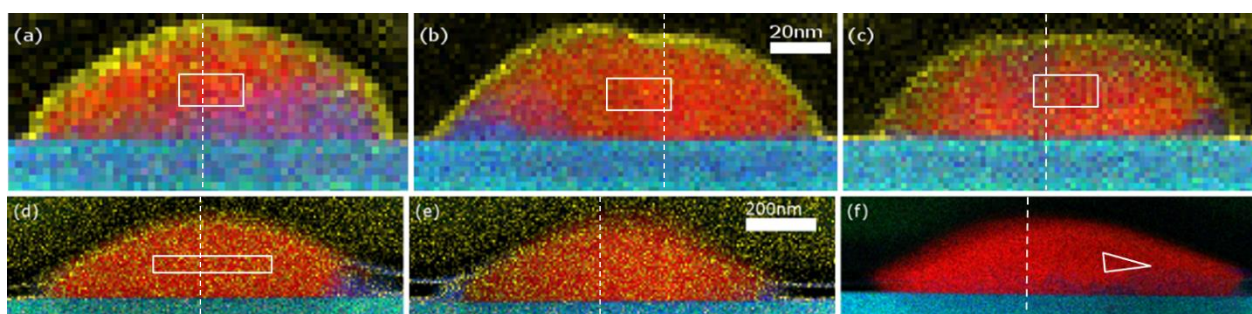


Figure 4.4 False-color elemental composition maps of In38 (a, b, c), In44 (d, e), and In54 (f) islands. The white boxes show the approximate area over which quantitative EDS was performed, and the dashed lines show the line scan paths. The 20 nm scale bar applies to a, b, and c, and the 200 nm scale bar applies to d, e, and f. Red corresponds to In, blue to As, cyan to GaAs, purple to InGaAs, and yellow to O. Oxygen has been omitted from (f) to increase the visibility of As.

The distribution of other elements was inconsistent in the small islands, with Ga/As-rich regions appearing near the substrate in some islands, but appearing near the tops of other islands. The quantitative indium percentage in the small islands varied dramatically, partly due to Ga/As-rich regions overlapping the quantitative measurement region to differing degrees in each island. Although indium was the most common element throughout the majority of each island, Ga and, to a lesser extent, As were present in at least low amounts throughout every small island.

The quantum well beneath the small islands was well-defined in EDS area images, although the quantum well cap layer contained significant levels of indium in some locations. This was most pronounced in one particular line scan, in which the quantum well was indistinguishable from the cap layer. However, this seemed to be the result of unfortunate line scan placement, as the other line scans showed distinct well and cap regions. Quantitative EDS measurements of the quantum well and substrate regions were in close agreement across all small islands, although the measured levels of arsenic were lower than expected (any  $\text{In}_x\text{Ga}_{1-x}\text{As}$  alloy should be 50% arsenic by atomic percentage) and the measured levels of gallium were higher than expected.

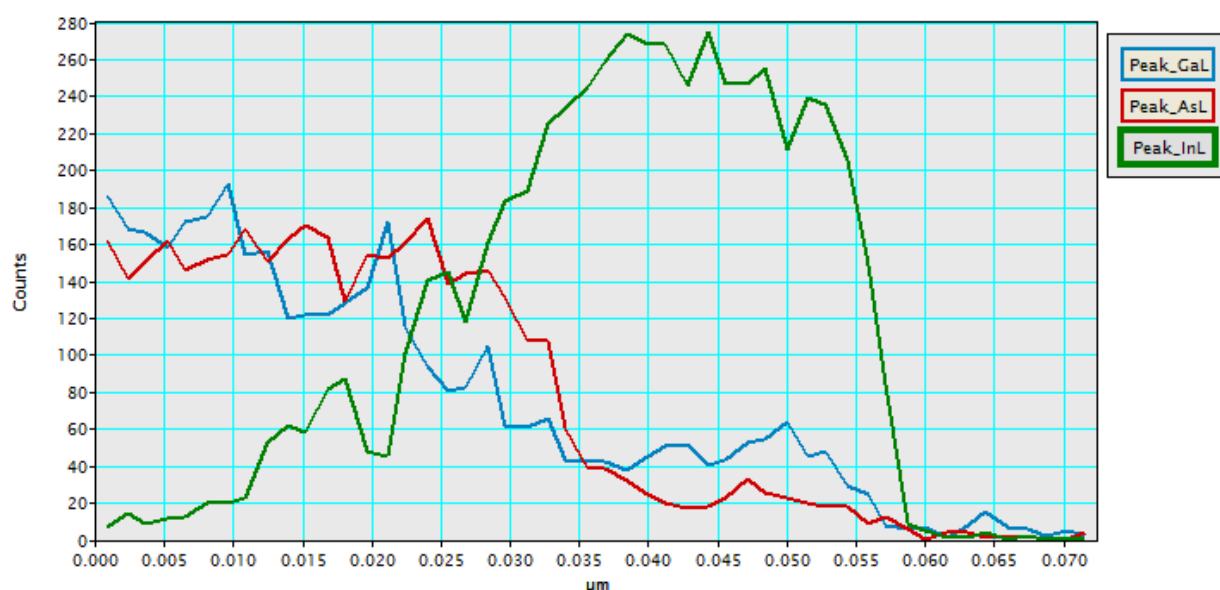


Figure 4.5 In38 Island 1 line scan, clearly showing a dip in indium corresponding to the GaAs cap layer between the InGaAs well and indium island.

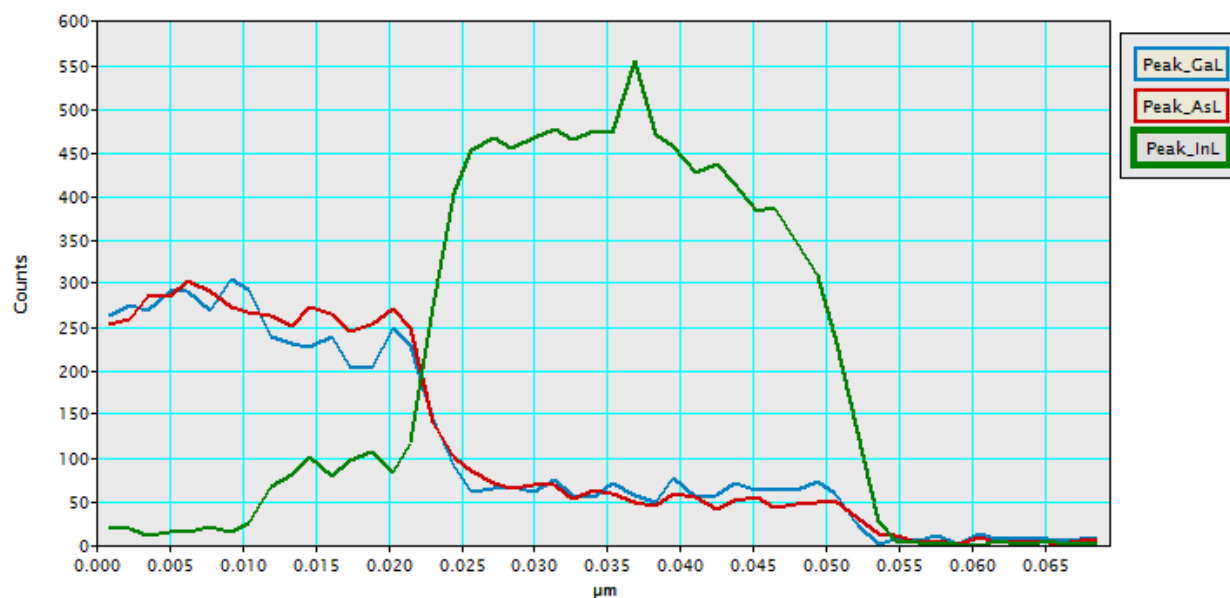


Figure 4.6 In38 Island 2 line scan, in which the GaAs cap is indistinguishable from the InGaAs well.

Virtually no arsenic or gallium was visible in the main body of the medium islands.

Quantitative measurements of one island corroborated the EDS area results. However, gallium and arsenic were visible in the corners of each island. Because the samples being measured are cross-sections of the original structures, the pattern of impurities in these islands suggests that a ring of GaAs or InGaAs surrounded each island.

Table 4.1 Average elemental composition of island interiors by atomic percentage.

Sample	In	Ga	As
In38	66.0% ( $\pm 2\%$ )	12.7% ( $\pm 0.7\%$ )	21.3% ( $\pm 0.8\%$ )
	89.9% ( $\pm 1.5\%$ )	5.6% ( $\pm 0.5\%$ )	4.5% ( $\pm 0.5\%$ )
	82.5% ( $\pm 1.8\%$ )	8.0% ( $\pm 0.6\%$ )	9.4% ( $\pm 0.6\%$ )
In44	94.7% ( $\pm 1\%$ )	3.1% ( $\pm 0.5\%$ )	2.2% ( $\pm 0.5\%$ )
In54	96.1% ( $\pm 1\%$ )	2.5% ( $\pm 0.5\%$ )	1.41% ( $\pm 0.5\%$ )

Even lower amounts of arsenic and gallium were present in the main body of the large island. However, the Ga/As-rich regions in the large island did not have the same distribution as those in the medium islands; the gallium and arsenic were spread out more uniformly along the base of the large island. As previously noted, the different-colored regions in the body of the large island did not consistently line up with regions of higher impurities.

Indium was present directly beneath the larger islands; each one exhibited a mixed In/Ga/As region roughly 10 nm thick along the island-substrate interface. The indium levels dropped off very sharply with increasing substrate depth - quantitative EDS measured only 3.65% indium at a depth of 7 nm below the large island. The In/Ga/As intermixed region appeared to only be 5 nm thick in the small islands, although the presence of the InGaAs well 5 nm below the islands makes it difficult to determine how the substrate indium levels truly drop off.

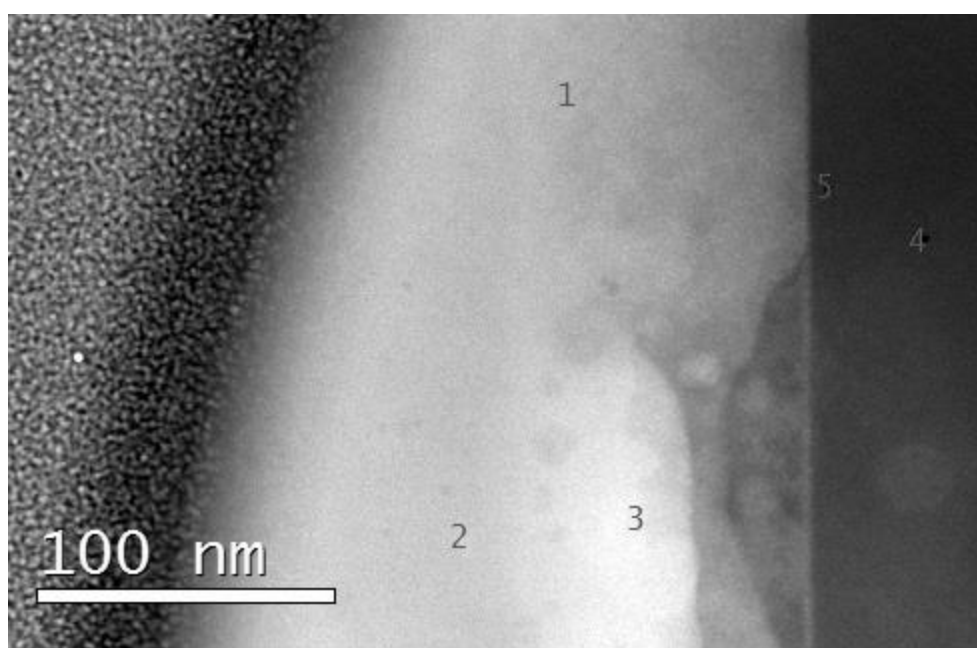


Figure 4.7 TEM image of In54 with quantitative EDS measurement points highlighted. Table 4.2 contains composition results for each point.

Table 4.2 Elemental composition of In54 measurement points by atomic percentage.

Point	In	Ga	As
1	93.9%	4.48%	1.63%
2	97.4%	1.53%	1.05%
3	96.9%	1.59%	1.55%
4	0.66%	51.3%	48.0%
5	3.65%	49.2%	47.2%

Island impurities were somewhat correlated with the different-colored island regions in the TEM images. However, in most cases, the regions of impurities were only subtly different colors from the bulk island, and the amount of gallium compared to arsenic seemed unrelated to the precise coloration. The oxygen-rich shell around each small island lined up extremely well with the shell of a slightly different color observed in the TEM images. The oxygen shell did not seem to be visible in TEM images of larger islands.

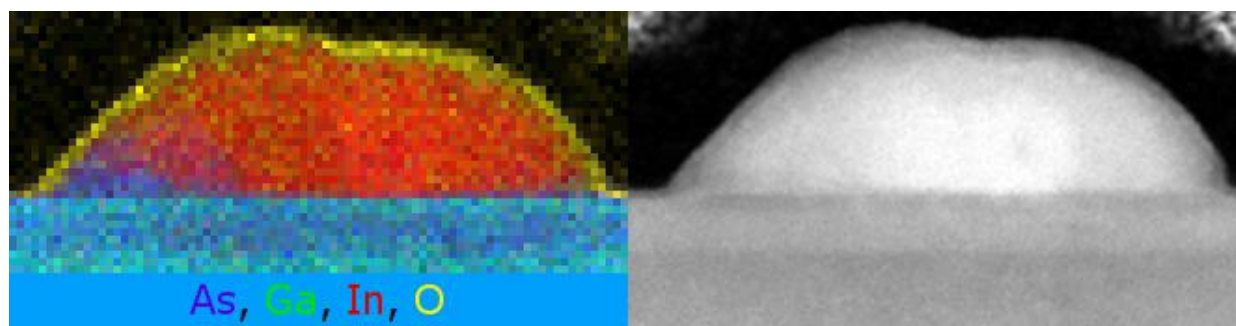


Figure 4.8 Comparison of EDS colormap and TEM image of In<sub>38</sub> Island 2.

The small island composition maps also revealed a shockingly high amount of copper in some islands. Because it is virtually impossible for copper to have been present in any measurable quantity during island growth, the copper was almost certainly an artifact introduced during cross-section sample preparation; the sample holder, present during the final milling steps, was made of copper. Molybdenum sample holders were used for the larger island samples, and neither copper nor molybdenum were observed in those samples in appreciable quantities.

In addition to the oxygen-rich shell around each island, oxygen was present in low levels throughout every island and in even lower levels in all substrates. Pure indium will oxidize, so the oxygen present within the islands is likely due to post-cross-sectioning oxidation, and was almost certainly not originally present (there is virtually no oxygen in the MBE growth chamber during indium deposition). GaAs oxidizes far more slowly than pure indium, which might alone explain the lower oxygen levels observed in the substrate. However, the oxygen EDS peak also

overlaps somewhat with the arsenic EDS peak; it is possible that the low levels of oxygen reported throughout the substrates are actually an artifact of the strong arsenic signal.

#### **4.4 Discussion of Results**

Some small islands were round, while others were faceted. Among faceted islands, some appeared to be almost pyramidal. Unfortunately, I did not pay close attention to the shapes of the islands selected for analysis, and so can only make educated guesses as to the original shapes of the islands; specifically, I believe In38 Island 1 was faceted, while In38 Island 2 and In38 Island 3 were round. Fortunately, our collaborators in Germany did pay attention to the islands they tried to analyze, and managed to prepare one circular and one faceted island for analysis.

Comparing the cross-section shapes of our islands to their islands allows me to be more confident in my guesses. Island shape was not a concern for the larger islands, as all of those islands were round.

The literature reports that InAs islands (uncapped quantum dots) are pyramidal. Among the small islands I analyzed, the faceted island had a substantially-higher atomic percentage of arsenic, and also exhibited much more arsenic along the island-substrate interface than the other islands did. The two islands analyzed in Germany seemed to show a similar pattern of arsenic distribution, although the pyramidal island contained a higher percentage of indium near the top of the island compared to the round island. It is possible that a higher arsenic percentage along the island-substrate interface leads to faceted island shapes, although the sample sizes are too small to draw any concrete conclusions. If faceted islands are indeed indicative of increased levels of arsenic, round islands would likely behave more similarly to ideal nanoantennas.

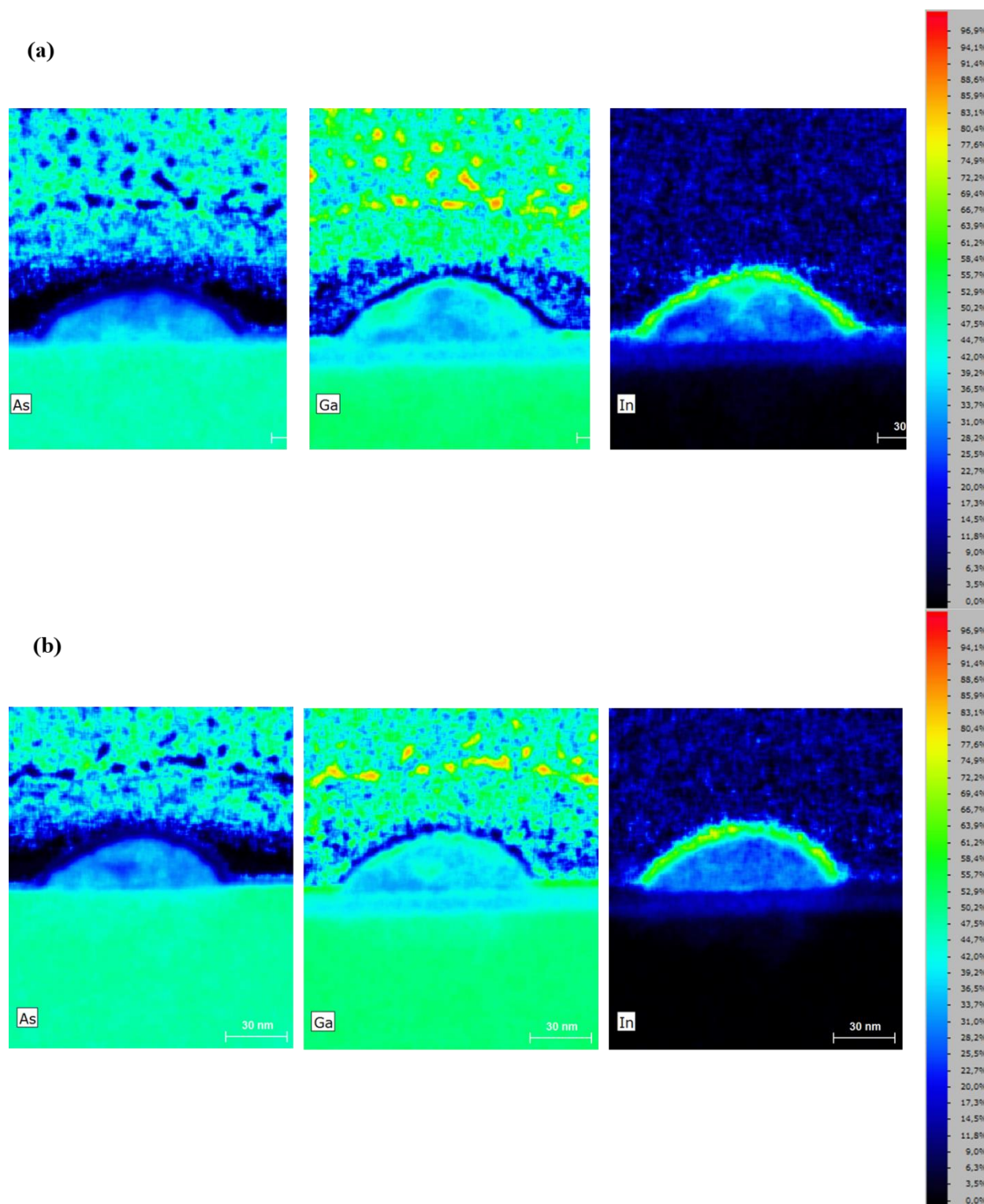


Figure 4.9 In<sub>38</sub> quantitative EDS results from Germany. (a) Pyramidal-shaped island, with highest measured atomic indium percentage around 55%. (b) Round island, with highest measured atomic indium percentage around 42%. The high-indium shells correspond to the oxide layer (oxygen not pictured).

The use of a Ga<sup>+</sup> ion beam for sample preparation was anticipated to contribute low levels of Ga throughout the sample, but this source of contamination was not expected to exceed 5% by atomic percentage [41]. Based on the quantitative EDS results, the actual levels of Ga<sup>+</sup> contamination were less than 3%. Although Ga<sup>+</sup> ion contamination appears to have been minimal, it may largely explain the unexpected gallium and arsenic ratios observed beneath the small islands. However, it is also possible that the quantitative measuring equipment was improperly calibrated for our particular sample, and the reported quantitative results are simply slightly incorrect.

The oxygen-rich shell around each island was almost certainly the result of indium oxidation following the removal of each sample from the growth chamber. This shell was 4-7.5 nm thick in the small islands and 15-25 nm thick in the larger islands, according to EDS measurements.

Although the oxide layer appeared to be thicker in the larger islands, this may partly be due to the larger island cross-sections being thicker. There is not a clear reason for a thicker oxide to form on a larger island, since the oxide layer is thin compared to the island height in all cases. However, because oxides form more slowly on GaAs than on pure indium, it is possible that the presence of more gallium and arsenic halted the oxidation process earlier in the smaller islands. Indium islands incorporated into devices would most likely be exposed to oxygen at some point during device fabrication, so oxide shells would likely form on all indium islands. This shell might need to be compensated for by, for example, using a metal deposition process that penetrates several nanometers into the islands in order to ensure good contact between the metal and indium. It is also possible that an indium oxide shell is not a cause for concern; In<sub>2</sub>O<sub>3</sub> has been linked to superconducting behavior, independently of pure indium. [42]

Some islands clearly had non-uniform height in the region captured within the cross-section. This made certain measurements, such as oxide thickness, less accurate, as the oxide of one part of the island appeared on the same plane as the indium of another part of the island. Carbon and platinum also overlapped with the island in some cases, although this did not seem to impact measurements of relative In/Ga/As levels.

Islands on the same sample appeared very similar to one another. Although there did not seem to be a pattern of Ga/As contamination within the small islands, every small island reliably contained some Ga/As-rich patches. This suggests that these high-impurity regions were produced through a mechanism affecting most islands. The higher overall levels of arsenic present in the smaller islands may be the result of the shorter arsenic pump-out time, although this would not explain the higher levels of gallium.

The small and medium islands were grown with the same amount of indium; the primary difference between the two growths was the temperature of the indium during deposition. It appears that the higher indium temperatures used in the growth of the small islands resulted in the indium collecting more substrate material before or while redistributing into islands. This collected material then formed into chunks within the islands, possibly via Ostwald ripening (the process of smaller bits of a material shrinking away while larger clumps grow even larger) [43]. This material transport could have been possible due to certain  $\text{In}_x\text{Ga}_{1-x}\text{As}$  alloys having much lower melting points than others, which would have allowed solid pieces of material to exist in a temporarily-liquid medium, and ultimately become fixed in place as the overall island cooled.

As mentioned earlier, the pattern of Ga/As contamination in the medium islands suggested a Ga/As-rich ring surrounding each island. During the capping of InAs dots with GaAs, dots have often been observed to deform into ring shapes. It is possible that a mechanism

similar to the one that causes InGaAs rings to form during quantum dot growth is responsible for the presence of an InGaAs ring around the medium islands. However, it should be noted that the actual chemical composition of the Ga/As-rich region was not determined, and so might not actually be InGaAs. Also, the levels of indium at the edges of the island are very low, which would mean the ring, if present, would be much closer to GaAs than InAs.

The large island was grown using the same indium temperature as the medium islands, but with substantially more total indium, and thus, a substantially longer growth time. There are not Ga/As-rich regions confined only to the corners of the large island; instead, the entire ~50 nm region near the island-substrate interface contains higher levels of gallium and arsenic than the rest of the island. It seems likely that the initial growth was very similar to that of the medium islands, but that, over the course of the rest of the growth, the localized gallium and arsenic slowly diffused along the island-substrate interface. It is also possible that some of the impurities in this region are simply the result of diffusion from the substrate, which would explain the roughly-constant maximum impurity height across the island.

Based on the composition measurements taken directly beneath the islands, the growth of larger islands does not result in large amounts of indium several nanometers beneath the island-substrate interface. Thus, it is unlikely that medium and large island growth would appreciably alter the photoluminescence wavelength of near-surface quantum wells or dots, as the composition, and thus the bandgap, of the cap layer would not be substantially altered. A larger percentage of indium was observed in the GaAs layer beneath the small islands.

According to the EDS results, the In<sub>38</sub> islands contained significant amounts of non-indium materials. PL measurements of unaltered In<sub>38</sub> were compared to PL measurements of In<sub>38</sub> with the islands etched away, and the PL of the etched sample was significantly higher than

that of the original sample. This etching process resulted in lower PL when performed on other samples, suggesting that the In<sub>38</sub> islands were actually reducing the emission of the underlying quantum well rather than enhancing it as intended.

It is possible that the high levels of Ga and As within the In<sub>38</sub> islands caused the overall structure to behave more like a semiconductor cavity, increasing the mode volume. It is also possible that the high levels of impurities caused additional scattering of moving electrons, decreasing the Q-factor of the cavity by increasing the rate of energy loss. Either of these effects would reduce the Purcell factor, and thus, the predicted enhancement of the spontaneous emission rate.

Because other indium island samples did exhibit PL enhancement of underlying quantum structures, it seems likely that islands with average indium purities greater than the 80% observed in In<sub>38</sub> are necessary for useful nanoantenna behavior.

The substrate was held at the same temperature for all three samples analyzed. While this does not give an indication as to how substrate temperature impacts island composition, the lower indium percentages observed in islands grown with a higher indium temperature suggests that a higher substrate temperature may also result in a higher percentage of impurities, likely due to increased diffusion rates.

The purity of the larger indium islands indicated that superconducting behavior would be observed at low temperatures. Superconductivity was later experimentally verified using the large island sample [44]. Because the medium and large islands have very similar indium percentages, it is very likely that the medium islands are also capable of superconducting. The medium and large islands were grown at the same indium temperature, but with different total

amounts of indium; this suggests that any islands grown at this indium temperature using between 12 and 36 monolayers of indium should be superconducting at low temperatures.

Indium temperature primarily controls island density, while indium quantity primarily controls island size. Based on the composition analysis results, it is possible that impurities are unavoidable in small, dense island growth, but that small, sparse islands can be grown with minimal impurities by depositing fewer than 12 monolayers of indium at 510°C.

## CHAPTER 5: MICRODOME FORMATION ON INDIUM ISLAND SAMPLES

### 5.1 Context of Observation

During the TEM cross-section preparation of In44 (the medium island sample), round features were noticed near the indium islands:

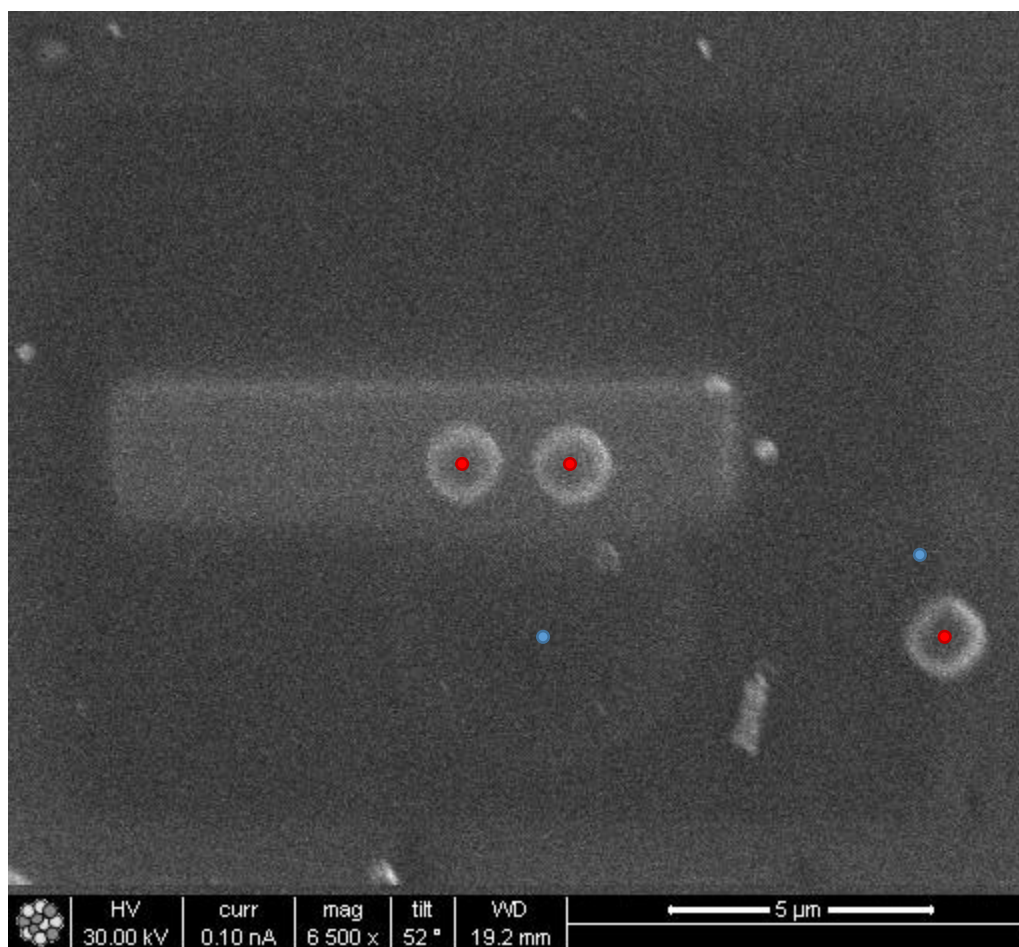


Figure 5.1 First observation of microdome formation. Red dots are placed on indium islands; blue dots are placed on domes.

One such feature was present between the two islands chosen for analysis, which allowed the feature to be cross-sectioned and analyzed along with the islands. EDS analysis of the feature revealed that the feature was mostly empty space.

Due to the settings used to take initial SEM images of the indium island samples, it was not possible to concretely determine whether the hollow features were present before TEM preparation, or were an artifact of the carbon deposition during cross-section preparation. AFM scans were later taken of another piece of In44 and other indium island samples, confirming that the substrates were flat and smooth post-growth, and that the hollow features must have formed during the TEM preparation process.

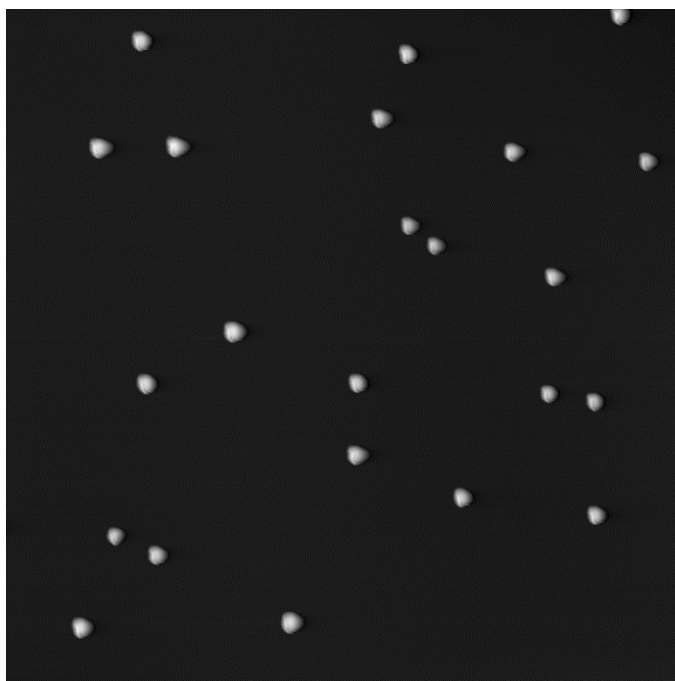


Figure 5.2 AFM image of In44. Region is  $60\ \mu\text{m} \times 60\ \mu\text{m}$ . All white features are indium islands; very little variation is seen in substrate height.

During the TEM cross-section preparation of In54, dome-shaped features were observed following the carbon deposition step. The shapes of these features were confirmed by tilting the stage to increase the contrast between the raised domes and the flat substrate. When one of the domes was cut through with the FIB, it collapsed in a manner reminiscent of a deflating balloon, which was consistent with the previous observation that the domes appeared hollow.

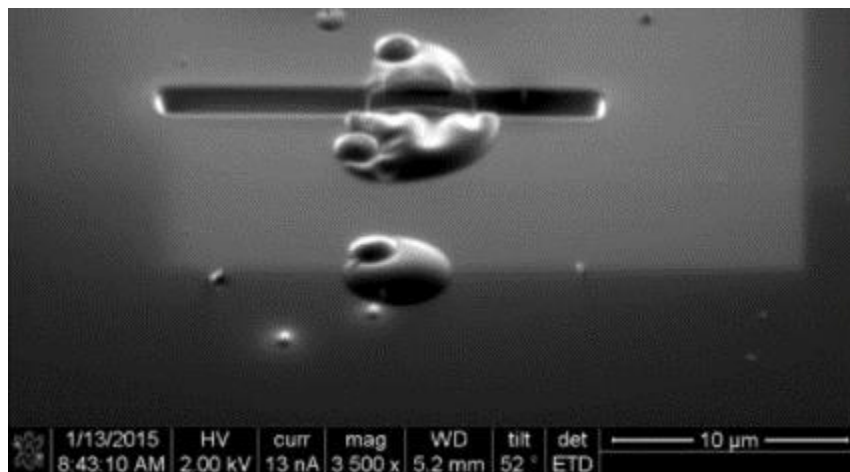


Figure 5.3 SEM image of In54 at the start of the ion milling process.

Hollow domes were not present in the In38 cross-section. This difference between samples can also be seen in the images of individual islands; the In44 and In54 islands each have thin lines of material leading away from the edges of the island with empty space between the material and the substrate, while the In38 islands do not. These lines of material seem to correspond to dome edges.

## 5.2 Characterization of Microdomes

The observed domes varied in size from approximately 1  $\mu\text{m}$  to 5  $\mu\text{m}$  in diameter. Height was more difficult to determine, but the domes appeared to each be approximately .5  $\mu\text{m}$  tall at the highest point. The domes were round, although not perfectly circular. Every island in the observed region had a dome extending out from the island, and there were no domes not connected to islands. In one case, two islands were connected to the same irregularly-shaped dome, which seemed to be the result of two domes merging.

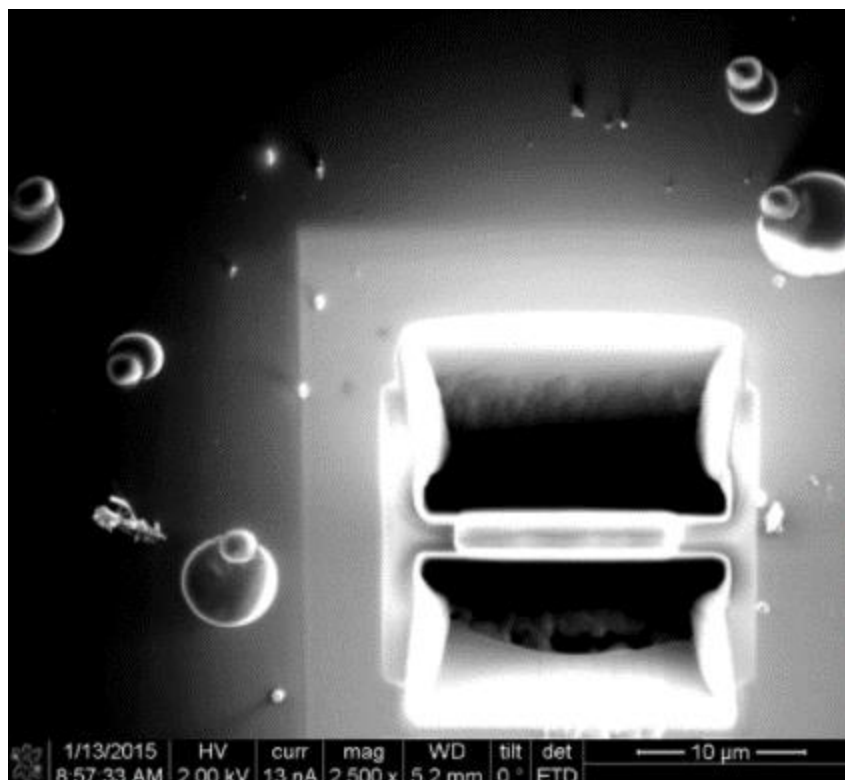


Figure 5.4 SEM image of In54 showing five islands with attached microdomes.

The region of observation mostly corresponded to the region over which the electron beam was rastered to deposit the conformal carbon coat. Domes within the carbon coat region tended to be larger than domes outside that region, although sizes varied. Domes seemed randomly oriented with respect to their attached islands and the center of the carbon coat region.

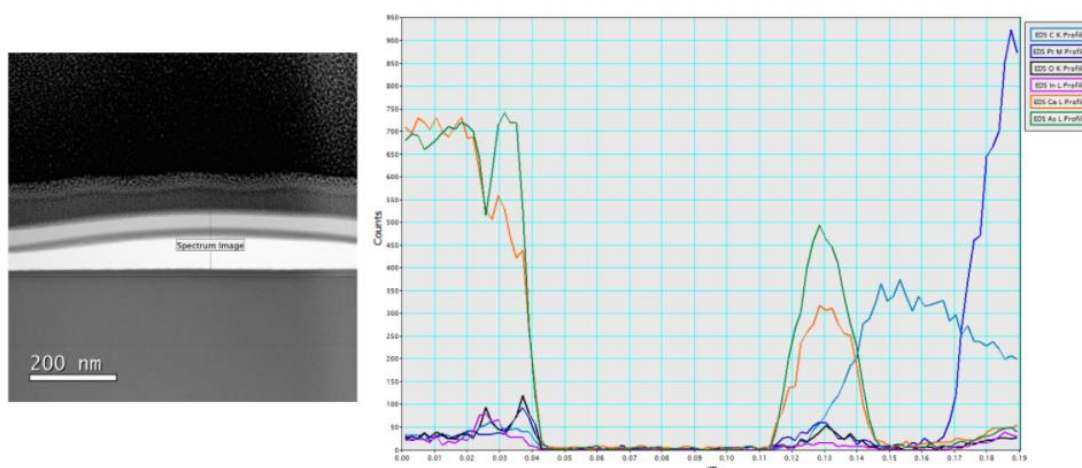


Figure 5.5 EDS line scan of dome cross-section. Low-count region near the center of the graph corresponds to the white region in the TEM image.

Under TEM observation, the outer shell of the dome captured in the In44 cross-section was approximately 20 nm thick. EDS analysis revealed that the shell was mostly arsenic, with some gallium, oxygen, carbon, and possibly indium and platinum. It is unclear whether the latter two elements were actually present in the shell, as the levels indicated by the line scan were very similar to the baseline levels of indium and platinum measured in the substrate (where the indium and platinum levels should have been close to zero).

Because the thin lines of material leading away from the larger islands were likely part of attached domes, these lines are another source of information. Based on the area maps of the larger islands, virtually no indium was present in the dome shells, and gallium was present at lower levels than arsenic. The shell thickness in the area maps seems to be approximately 20 nm (based on a thickness of 3-4 pixels and a pixel size of ~5 nm).

### **5.3 Attempts to Replicate**

All three samples went through the same TEM preparation steps using the same equipment (FEI NOVA 200). Thus, it is somewhat surprising that In38 did not exhibit microdomes while In44 and In54 did. Because microdomes were not observed on all prepared indium island samples, it was important to perform replication attempts on a sample already known to support microdome formation. Therefore, pieces of In44 were used in all replication attempts. The equipment used for these attempts was an FEI Helios DualBeam.

Microdome formation was originally observed immediately following the deposition of a conformal carbon coat layer. To check whether the domes were forming simply in response to the presence of carbon, a piece of In44 was sputter-coated with carbon. The sputtered carbon coat was approximately 50 nm thick, similar to the thickness of the conformal carbon coat created during TEM cross-section preparation. No domes were observed under SEM

examination of the sputtered sample; in fact, the islands could no longer be found post-sputtering, indicating that this method of carbon deposition may have destroyed the islands.

Next, an FEI Helios DualBeam an electron beam was rastered over a section of sample for a long period of time. The slight hydrocarbon contamination on the sample (due to exposure to atmosphere) provides a carbon source, and the electron beam fixes the carbon to the surface of the sample. As the carbon is fixed to the surface, a local low-concentration region of hydrocarbons forms, while hydrocarbon surface diffusion continues to provide more material for the electron beam to fix to the surface. No microdomes were observed following this process.

Finally, the original carbon coat conditions were replicated, although still using the Helios rather than the original NOVA. Hydrocarbon gas was flowed over the sample, and the electron beam was rastered across the sample to fix the hydrocarbons to the surface. Although a conformal carbon coat of approximately 30 nm was created, no domes appeared.

It is possible that the failure to replicate the microdome formation on other pieces of In44 was due to the different equipment. It is also possible that the electron beam accelerating voltage or current was different during the replication attempt. Over a year elapsed between the original microdome observation and the replication attempts; microdome formation may have become impossible as the sample aged.

## **5.4 Possible Explanations**

Microdome formation does not seem to always result from the conformal carbon coating technique used; thus, It seems likely that, in the regions of substrate that exhibited dome formation, the top layer of material was already prone to delamination.

Since simply the presence of a surface layer of carbon was not sufficient to create microdomes, it is possible that the hydrocarbon gas flowing across the sample contributed to the

delamination, essentially inflating the domes. Because the domes did not deflate once the flow of hydrocarbon gas was stopped, and because the SEM chamber was kept at low vacuum after the conformal carbon coat step, it seems unlikely that the domes needed to stay filled with gas to hold their shape.

It is possible that heating from the electron gun caused the surface layer to thermally expand. However, the increase in surface area between the flat substrate and subsequent microdomes seems to be far too large to entirely attribute to thermal expansion, and the persistence of the domes indicates that the material forming the dome has expanded permanently. If thermal expansion did play a role in the formation of the microdomes, it seems likely that its primary role was through differential expansion of the dome material and underlying flat substrate, facilitating delamination.

Observations of rapidly-cooled indium island samples indicate that larger islands shift around after indium deposition has ended, during the cooling phase. On these rapidly-cooled samples, many islands exhibit a nearby region of thinner substrate that appears in both SEM and Atomic Force Microscopy (AFM) images [12].

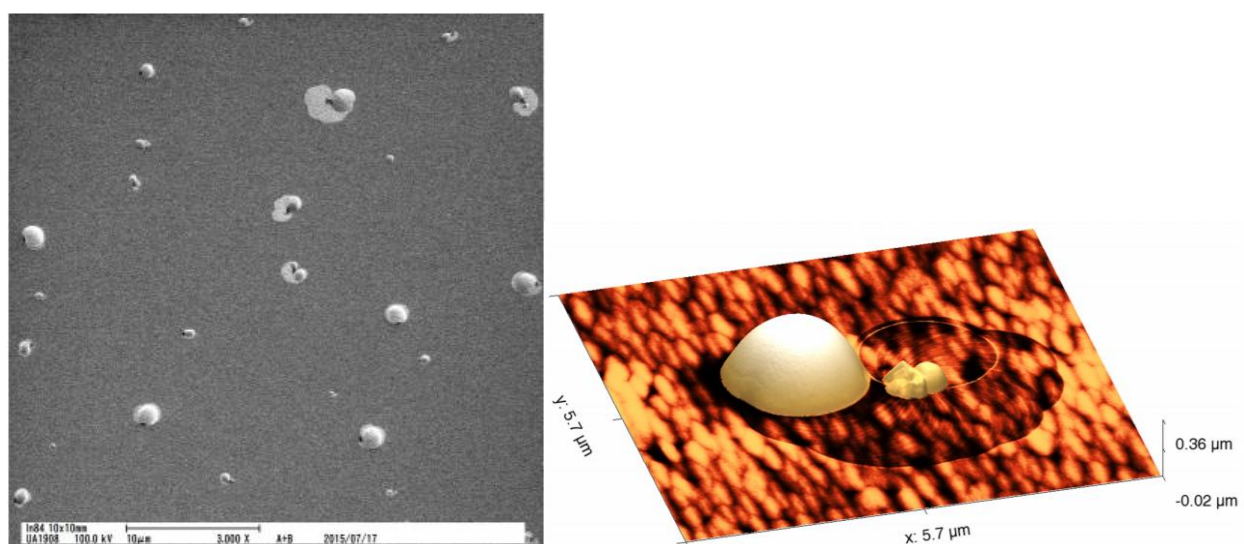


Figure 5.6 SEM (left) and AFM (right) images of rapidly-cooled indium islands. The AFM image shows that the light regions near some islands in the SEM image are depressions.

This feature was not observed in In44 or In54 prior to TEM cross-section preparation, despite these samples being grown under very similar conditions to samples with non-uniform substrates; the primary difference in growth conditions was that In44 and In54 were allowed to slowly cool from growth temperatures to room temperature. It is possible that the substrate is altered in all larger indium island samples, but that slow cooling allows the substrate to smooth back out, and that the microdomes observed during TEM cross-section preparation formed from these altered substrate regions.

The EDS line scan was taken starting in the GaAs substrate and ending in the platinum layer above the dome. Although this line scan is a qualitative measurement of composition, not a quantitative measurement, certain inferences can be made. The intensities of the Ga and As signals are approximately equal in the substrate, where the ratio of Ga to As should be 50:50. This indicates that the Ga and As lines should be approximately equal in regions with equal amounts of Ga and As. In the shell, the Ga line is significantly below the As line. This indicates that the shell was likely not composed entirely of GaAs and contained arsenic in other forms.

If this line scan interpretation is correct, it would mean that some amount of gallium was displaced from the top layer of GaAs substrate, either during indium island growth or during TEM cross-section preparation.

### **5.3 Potential Applications**

In both observations of dome formation, every island in the observed region had an attached microdome, and no microdomes formed unattached to islands. This consistency could be valuable in the context of reliable, targeted microdome formation as part of device fabrication.

The literature shows that microdomes have been used as optical resonators [45]; after the incorporation of an active emitter, microdomes have functioned as lasers [46]. It is possible that the microdomes formed on our samples could function as optical resonators with resonances

$$2\pi a = m \frac{\lambda}{n}, \quad (5.1)$$

[47] where  $a$  is the radius of the microdome along the path of propagation,  $m$  is an integer, and  $\lambda/n$  is the resonant wavelength in the material. Because a single microdome can support many different resonant wavelengths, microdomes of any size can be suitable for applications that do not require extremely precise wavelengths.

In the case of GaAs microdomes, an additional active emitter would not necessarily need to be incorporated for the emission of light. GaAs is a direct-bandgap material that can emit infrared light [48], and so, it is possible that a GaAs microdome could form a laser cavity. It is likely that these domes are not composed of pure GaAs; however, InAs and InGaAs can also emit light, particularly when encased in GaAs.

Coupling to dome-shaped microresonators can prove a challenge; fortunately, the indium island attached to each dome could provide a method of coupling light into or out of the resonator. Thus far, we have been inducing photoluminescence in quantum structures beneath nanoantennas by shining an optical pump source perpendicular to the surface of the sample. If these nanodomes could be used to couple light into the nanoantennas, shining light parallel to the surface of the sample could prove a more efficient coupling setup, as a pump photon would have multiple chances to couple into a resonator rather than passing ineffectually through the sample if it did not initially interact with a nanoantenna or underlying structure.

If a microdome attached to an indium island were capable of light emission, the island could be used to couple pump light into the dome to stimulate emission. Alternatively,

microdome emission could be induced some other way, and the resulting light could be outcoupled to the attached island.

## CHAPTER 6: LOCALIZED SUB-SURFACE INDIUM LAYERS

### 6.1 Motivation

While examining the cross-section of the microdome discussed in Chapter 5, a localized layer of high indium content was found only beneath the microdome. This layer was of particular interest because it could potentially constitute a quantum well that formed only beneath the microdome, not across the entire substrate.

Quantum wells grown via MBE usually span the entire wafer, existing as a uniform 2-D structure. This is usually a desirable quality, as the quantum well properties can be taken advantage of without the need for careful alignment during subsequent fabrication steps. However, if a quantum well were only needed in specific locations, parts of the substrate would need to be etched away to remove the quantum well structure, adding complexity and time to the fabrication process.

The sub-surface indium feature was observed next to, but not beneath, the In<sub>44</sub> and In<sub>54</sub> islands. If a quantum well were forming under part, but not all, of the substrate during the growth of indium islands, the resulting sample would consist of a non-overlapping set of quantum wells and nanoantennas, which would be a novel combination easily grown via MBE but difficult to accomplish via traditional lithography.

A handful of potential applications come to mind. Due to the different absorption properties of quantum wells and nanoantennas, this combination of structures could allow for photolithography without the need for a separate mask. Light with lower transmission through the quantum well than through plain GaAs (or vice versa) could be used to accurately discriminate between regions with and without an active emitter. Similarly, light could pass through the quantum well to expose a photoresist while not fully transmitting through the

nanoantennas, or vice versa. Alternatively, the nanoantennas could be removed through an HCl etch, which has been shown to preserve the PL of underlying quantum structures. This would result in quantum well-free regions via a simpler process than traditional lithography methods.

## 6.2 Experimental results

In order to understand the properties and applications of the observed sub-surface indium layer, composition and spectral analysis was performed. As seen in Figure 6.1, a thin, pale line was observed beneath substrate under the dome. The EDS scan of the microdome indicated that indium was present at higher levels in the line compared to the surrounding regions.

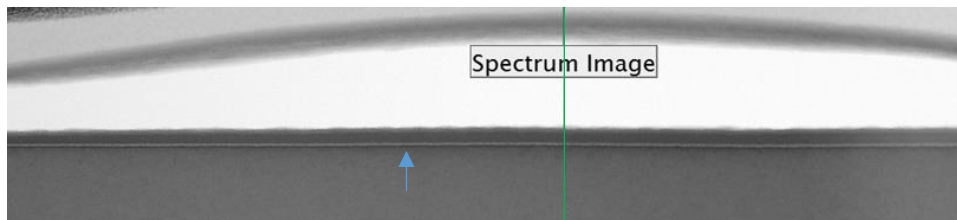


Figure 6.1 TEM micrograph of the hollow region between In44 islands. Arrow points to indium-rich line.

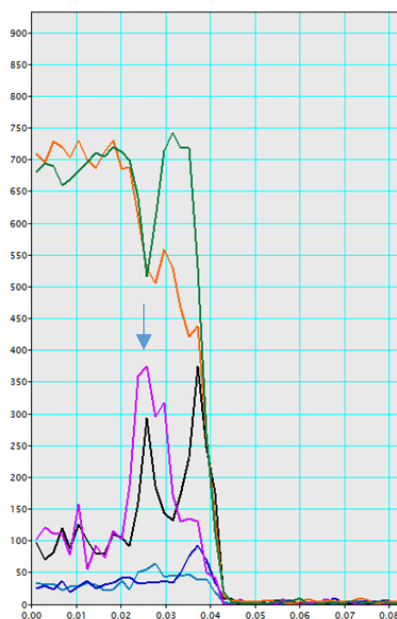


Figure 6.2 EDS line scan taken along the green vertical line in Fig. 6.1, with the indium (purple) and oxygen (black) lines scaled up to increase visibility. The arrow points at the indium peak corresponding to the thin white line in Fig. 6.1.

Upon closer inspection of the In44 and In54 island images, potentially-similar features were observed in the substrate next to each island. EDS area maps confirmed the presence of a thin line of indium in these regions.

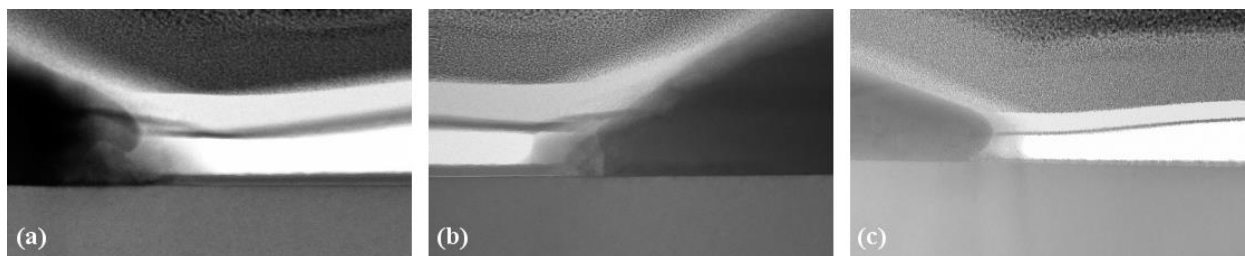


Figure 6.3 Images of sub-surface indium layers next to In44 Island 1 (a), In44 Island 2 (b), and In54 (c). As explained in Section 1.1.3, a quantum well can be formed by sandwiching a thin layer of low-bandgap material between two higher-bandgap layers; for example, the quantum well beneath In38 consists of a ~12 nm layer of InGaAs between GaAs cap and substrate layers. Based on the composition results from the EDS scan, it seemed possible that the thin line was a layer of  $\text{In}_x\text{Ga}_{1-x}\text{As}$  between a GaAs substrate and an  $\text{In}_y\text{Ga}_{1-y}\text{As}$  substrate, with  $x > y$ . The bandgap of InGaAs decreases with higher In content, so the observed feature was potentially a quantum well.

The EDS line scan suggests that the sub-surface indium region consists of a layer of indium that displaced both gallium and arsenic, followed by a layer in which the arsenic had not been displaced, but gallium had. After a peak 15 nm below the surface, the relative quantity of indium in the substrate seems to decrease with decreasing distance to the surface. The EDS area maps suggest a similar pattern, although the compositional resolution of the area maps is significantly worse than the resolution of the line scan (spectra were collected for 3s at each point along the line scan, but for only .1s at each point within the area maps), making it difficult to draw conclusions about relative compositions.

As previously noted, EDS line scans and area maps provide qualitative, not quantitative, information about the amounts of each element present at in a given region. These EDS results are best used to determine whether the quantity of a given element increased or decreased between two points. However, context allows for some minor extrapolation; the substrate is known to be GaAs, which should be a 50:50 ratio of Ga and As. Conveniently, the EDS line scan levels for Ga and As were nearly identical in the substrate, meaning that we can confidently assume that, when the Ga line is substantially lower than the As line, the ratio of Ga to As is lower than 50:50.

In this line scan, the As levels near the surface (below the dome shell) appear to be similar to the As levels in the substrate. The Ga levels near the surface are markedly lower than those in the substrate. In the dome shell, which would have formed the top ~20 nm of surface had it not delaminated, the As line is still substantially higher than the Ga line. Although indium is clearly present in some regions, it is impossible to tell from the data whether the indium fully compensates for the reduction in Ga, or whether the expected  $\text{In}_x\text{Ga}_{1-x}\text{As}$  structure is not present.

Peaks in the platinum line could be artifacts, but could also be actual platinum that penetrated through the protective carbon coat during cross-section preparation and displaced gallium. Peaks in the oxygen line might indicate the presence of oxides; because no oxygen is present during growth, oxide formation would likely have taken place after the cross-section was created, and would not be present in an uncut sample.

Unfortunately, EDS cannot determine which compounds are present in a sample, and so cannot distinguish between InGaAs and regions of pure indium mixed with regions of GaAs. However, if a quantum well were present, PL emission should be observed. In order to determine whether this sub-surface indium region comprised an InGaAs/GaAs quantum well, pieces of

In44, In54, and other, similar indium island samples were optically-pumped and evidence of PL was sought.

Based on the In44 EDS results, a quantum well, if present, would contain  $\text{In}_{0.3}\text{Ga}_{0.7}\text{As}$  or lower indium:gallium ratios. The well would be roughly 5 nm thick and 30 nm deep. Comparing this predicted structure to actual InGaAs/GaAs wells grown by our group, the expected wavelength of the predicted quantum well would be around 1100 nm, although the expected PL moves to shorter wavelengths with decreasing indium fraction. No PL was observed from these indium island samples in the range of 900 nm to 1100 nm, indicating that no quantum wells were present.

Transmission spectra of the indium island samples was also examined for evidence of quantum wells, in case a well was present but had extremely weak emission. In theory, wavelengths near the transition energy of the quantum well would show lower transmission due to absorption by the well. The transmission spectrum of each sample showed a clear dip at the indium island resonance, but did not show additional transmission dips that could be attributed to quantum well absorption.

### **6.3 Further analysis and possible explanations**

Of the three indium island samples thoroughly analyzed, a sub-surface indium layer was only seen in In44 and In54. The In38 data showed evidence of a thin surface layer of indium, consistent with the islands' predicted Stranski-Krastanov growth mode, but no unexpected sub-surface indium. In44 and In54 did not show evidence of a separate indium surface layer, suggesting that the sub-surface indium layer was originally the indium wetting layer formed at the start of island growth.

It should be noted that the lattice constant of pure indium is around 0.4 nm, and the resolution of the EDS line scan through the sub-surface indium layer was 1.9 nm. In Stranski-Krastanov growth, a complete single atomic layer of material forms, with islands forming above that layer. If the sub-surface indium layer were simply this monolayer, the EDS line scan should have shown a sharper indium peak. Instead, the sub-surface indium region appears to span many atomic layers, and possibly contains indium additional to the initial monolayer.

As previously mentioned, examination of rapidly-cooled indium island samples showed that part of the GaAs substrate was missing near many of the islands. However, in samples allowed to slowly cool to room temperature, such as In44 and In54, the substrate appeared smooth. It is possible that, as indium redistributes during the growth and cooling process, Ga and As atoms leach into the indium wetting layer and eventually diffuse to the surface before the material solidifies.

The absence of PL suggests that the crystal structure of the top layer of substrate does not contain InGaAs. If the top layer of substrate formed through displaced Ga and As atoms diffusing through liquid indium, it is also possible that the top layer of substrate is primarily not GaAs. This is supported by the Ga:As ratio appearing lower than 50:50, and by the ability of the top layer of substrate to form a dome with a significantly-larger surface area than that of the underlying substrate.

These results indicate that, although a sub-surface indium layer seems to form as part of the growth process of medium and large indium islands, this layer does not result in unintended PL or absorption behavior. The existence of a sub-surface indium layer that does not form a quantum well might still be useful. For example, an etchant that removes GaAs more quickly

than In-containing compounds could be slowed or stopped by this indium layer, improving depth control and uniformity during the etching process.

## CHAPTER 7: CONCLUSION AND FUTURE DIRECTIONS

In Chapter 3, a nanoantenna sample was examined for evidence of an ALD-deposited gain medium, which was ultimately not found. ALD was later determined to be unsuited to the goal of incorporating active emitters into silicon nanobeams, as the electric field in the nanobeam was unlikely to substantially interact with the ALD coating. However, the overarching idea of incorporating an active emitter into a silicon nanobeam is still an active area of research [49]. Including an active telecommunications-wavelength emitter within the silicon used to make the bar, rather than as part of an external coating, may achieve the on-chip light source originally mentioned as the motivation for this project.

Chapters 4, 5, and 6 of this dissertation provide novel insight into the composition of epitaxially-grown indium islands and related structures. The practical implications of these results are that high-purity (>94%) indium islands can be grown on top of GaAs; increasing the indium deposition temperature may lead to reduced purity of indium islands; and the MBE growth process seems to facilitate the formation of other structures (microdomes and sub-surface indium layers) unique to MBE growth. This information should be valuable to any other researchers pursuing epitaxially-grown nanoantenna structures for III-V systems.

The indium island samples analyzed in this work represent a small fraction of the total number of samples grown by our group. Other work [50] has shown that the presence of sparse islands (<4 per square micron) enhances the PL of underlying quantum dots. It was noted in Chapter 4 that In38, the small island sample, did not exhibit quantum well PL enhancement, possibly due to the lower (~80%) indium purity of the In38 islands. It is also possible that the high density of islands (~15 per square micron) on In38 contributed to the reduction, rather than enhancement, of PL. Fortunately, it appears that both indium purity and island density depend on

indium deposition temperature, meaning that sparser islands are likely to exhibit higher average purity.

One might notice that successful examples of PL enhancement through indium islands were observed in quantum dot samples, while the unsuccessful In38 sample contained a GaAs/InGaAs quantum well. It is thus logical to wonder whether indium nanoantenna enhancement of a quantum well is feasible. Reference [30] showed PL enhancement of an InGaAs/AlInAs quantum well via silver nanoantennas, and other papers have predicted or demonstrated nanoantenna enhancement of InGaN/GaN quantum wells [51][52][53]. So, although indium island enhancement of GaAs/InGaAs quantum wells has not yet been demonstrated, it is reasonable to expect future work to accomplish this result.

The III-V materials used in this work were limited to indium, gallium, and arsenic. While In/Ga/As structures have many applications, other III-V semiconductor materials, such as InP and GaN, are also commonly grown. GaN seems to be a particularly promising platform for future applications of epitaxially-grown indium islands, as it occupies a different niche than GaAs [54], but in many ways has similar material properties [55][56]. Attempting to grow self-assembled indium nanoantennas on GaN-based quantum structures seems like a logical future project.

Another area that merits further exploration is how the growth of indium islands impacts the emission wavelength of underlying quantum structures. The results of Chapter 3 suggest that the quantum well band structure may become asymmetric due to the GaAs cap incorporating indium during growth;  $\text{In}_x\text{Ga}_{1-x}\text{As}$  has a smaller bandgap than pure GaAs. However, at the indium concentrations indicated by EDS analysis, the overall shift in emission wavelength would

be a redshift of 1% or less, which is negligible compared to the spectral broadness of these quantum structures.

Oddly, the actual wavelength shifts observed in pairs of quantum dot samples (with one sample containing indium islands and the other containing only dots) suggest that the growth of indium islands blueshifts the emission spectrum, albeit inconsistently. Thus, it appears that MBE growth of indium islands may modify the emission spectrum of underlying quantum structures in ways other than through modification of the potential well shape, and that this effect should be fully characterized to make epitaxially-grown nanoantennas more suitable for wavelength-sensitive applications.

## APPENDIX A – FIBER TRANSMISSION DATA

This appendix contains additional data illustrating the observed Fano-Lorentz transmission lineshapes and demonstrating that the experimental setup described in Chapter 3.3 provides accurate lineshape data.

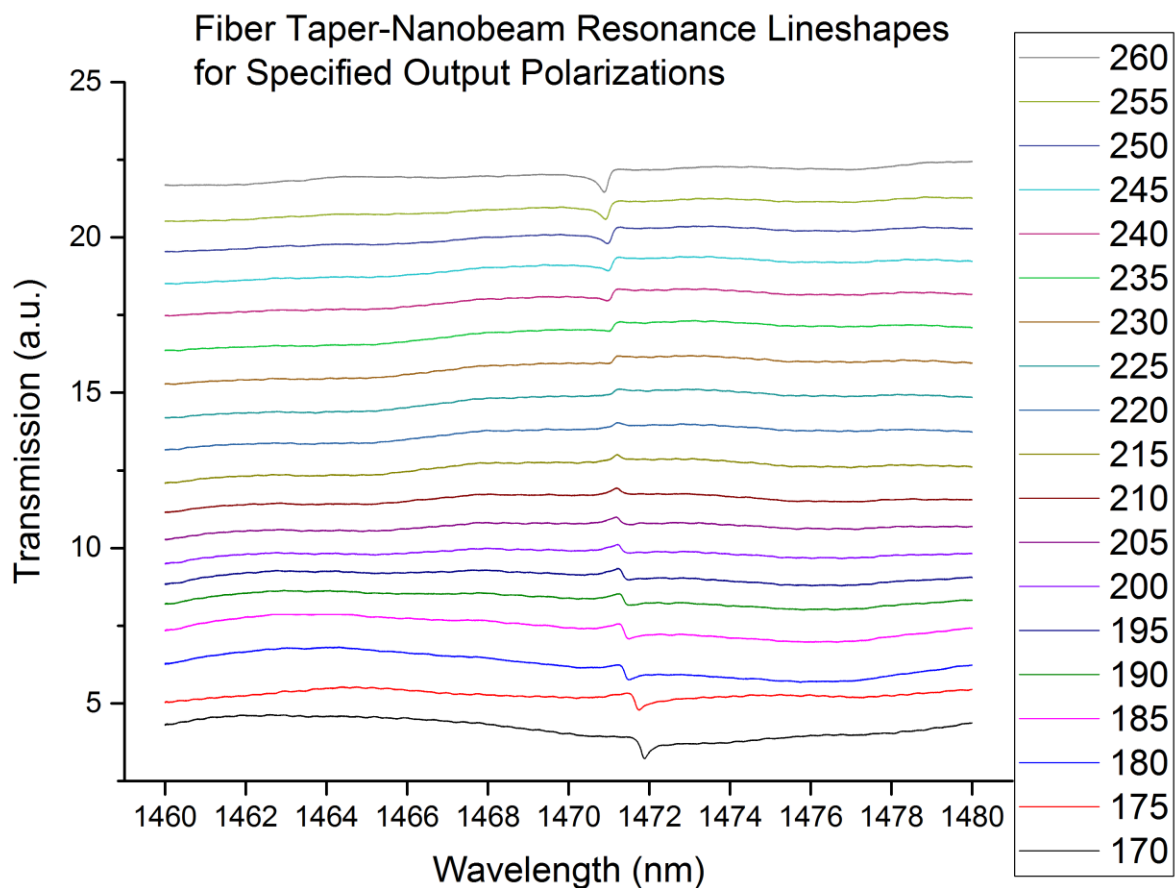


Figure A.1 Fiber transmission data across  $90^\circ$  of polarization on a single nanobeam.

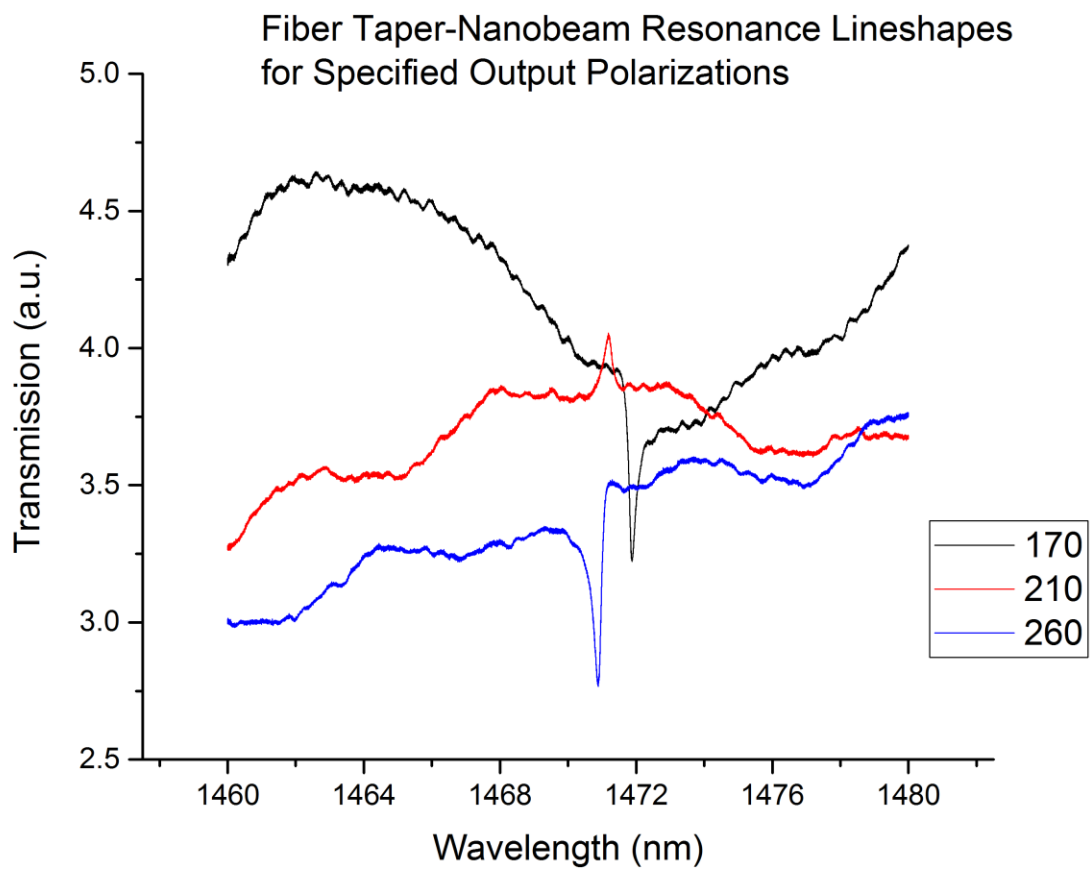


Figure A.2 Higher-resolution plots of three of the lines from Figure A.1.

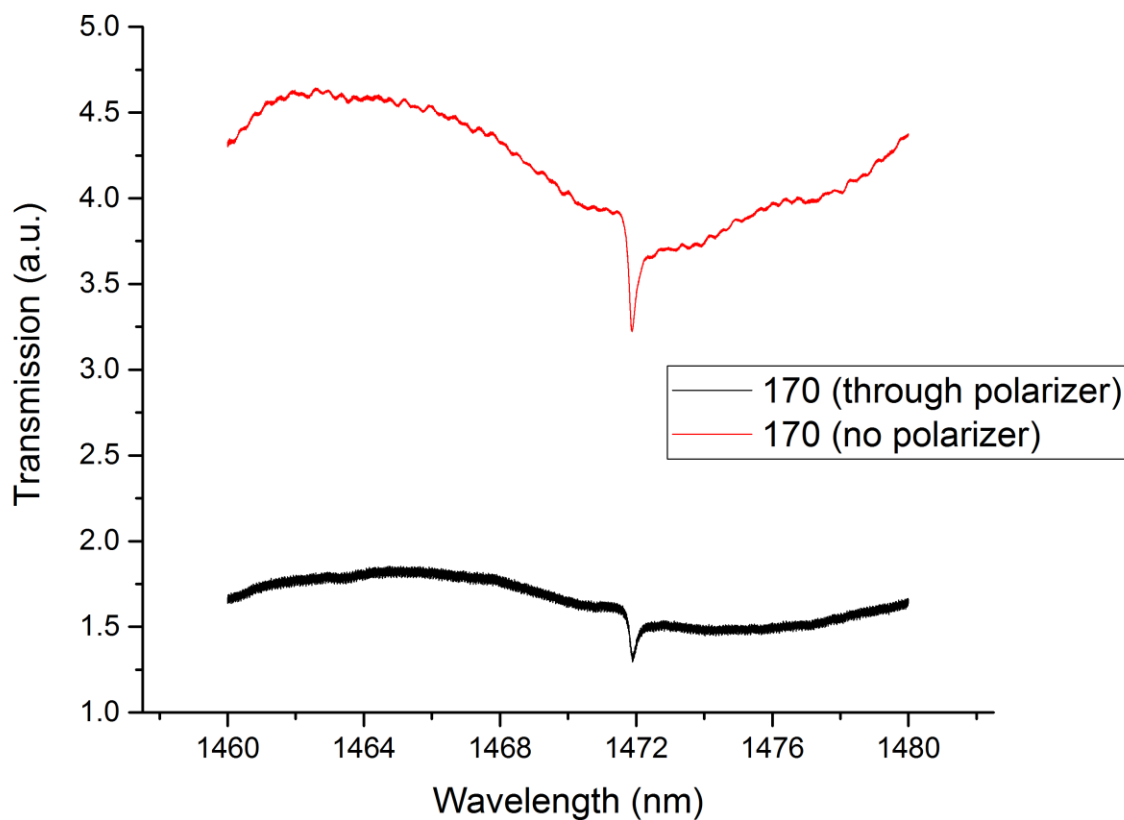


Figure A.3 Fiber transmission lineshapes taken before (black) and after (red) the fiber was connected directly to the photodetector. Bypassing the collimator and polarizer does not change the shape of the transmission peak, but does drastically improve the resolution of the transmission measurement. Pairs of transmission measurements (one through the collimator and polarizer, one bypassing these elements) were taken at each polarization angle to verify that the setup had remained stable during the adjustment.

## APPENDIX B – TEM EDS ANALYSIS OF EPITAXIALLY-GROWN SELF-ASSEMBLED INDIUM ISLANDS

Jasmine Sears, Ricky Gibson, Michael Gehl, Sander Zandbergen, Patrick Keiffer, Nima Nader,

Joshua Hendrickson, Alexandre Arnoult, Galina Khitrova

AIP Advances, Vol. 7, 055005 (May, 2017)

Copyright (2017), Reprinted with permission from AIP



## TEM EDS analysis of epitaxially-grown self-assembled indium islands

Jasmine Sears,<sup>1,a</sup> Ricky Gibson,<sup>1,2,3</sup> Michael Gehl,<sup>1,4</sup> Sander Zandbergen,<sup>1</sup> Patrick Keiffer,<sup>1</sup> Nima Nader,<sup>1,2,5</sup> Joshua Hendrickson,<sup>2</sup> Alexandre Arnoult,<sup>6</sup> and Galina Khitrova<sup>1</sup>

<sup>1</sup>College of Optical Sciences, University of Arizona, 1630 E University Blvd., Tucson, Arizona 85721, USA

<sup>2</sup>Air Force Research Laboratory, Sensors Directorate, 2241 Avionics Circle, Wright-Patterson AFB, Ohio 45433, USA

<sup>3</sup>University of Dayton Research Institute, 300 College Park, Dayton, Ohio 45469, USA

<sup>4</sup>Sandia National Laboratory, Applied Photonic Microsystems, P.O. Box 5800, Albuquerque, New Mexico 87185, USA

<sup>5</sup>National Institute of Standards and Technology, 325 Broadway, Boulder, Colorado 80305, USA

<sup>6</sup>LAAS-CNRS, 7 Avenue du Colonel Roche, 31000 Toulouse, France

(Received 1 February 2017; accepted 1 May 2017; published online 9 May 2017)

Epitaxially-grown self-assembled indium nanostructures, or islands, show promise as nanoantennas. The elemental composition and internal structure of indium islands grown on gallium arsenide are explored using Transmission Electron Microscopy (TEM) Energy Dispersive Spectroscopy (EDS). Several sizes of islands are examined, with larger islands exhibiting high (>94%) average indium purity and smaller islands containing inhomogeneous gallium and arsenic contamination. These results enable more accurate predictions of indium nanoantenna behavior as a function of growth parameters. © 2017 Author(s). All article content, except where otherwise noted, is licensed under a Creative Commons Attribution (CC BY) license (<http://creativecommons.org/licenses/by/4.0/>). [<http://dx.doi.org/10.1063/1.4983492>]

### I. BACKGROUND

As the field of plasmonic nanostructures develops, there is increasing demand for epitaxially-grown metallic nanostructures. Metal-on-semiconductor nanoantennas, which operate at optical and near-infrared wavelengths, have a wide range of potential applications, from low-cost photodetectors<sup>1</sup> to higher-efficiency solar cells.<sup>2</sup> Currently, nanoantenna fabrication is often performed separately from substrate preparation,<sup>3–8</sup> this discontinuity can adversely affect the finished product through contamination and impurities introduced during fabrication. One method for avoiding these issues is to epitaxially grow both the substrate and plasmonic nanostructure, with the structure self-assembling from a uniformly-deposited metal layer such as silver or indium.<sup>9,10</sup> Self-assembled nanostructures can additionally benefit from a better contact interface between structure and substrate compared to other fabrication methods.

Epitaxially-grown nanostructures may also have applications in quantum computing.<sup>11,12</sup> Majorana fermions, a candidate for qubit construction, have been observed in InSb nanowires coupled to superconducting NbTiN.<sup>13</sup> Other s-wave superconductor-1D semiconductor systems are also expected to generate Majorana fermions; InAs and indium have been identified as a potential semiconductor and superconductor, respectively.<sup>14,15</sup> InAs nanowires can be grown epitaxially, suggesting that self-assembled indium islands may allow for the epitaxial growth of entire Majorana fermion-generating heterostructures.

<sup>a</sup>Corresponding author. E-mail: [jasminesears@email.arizona.edu](mailto:jasminesears@email.arizona.edu)



While epitaxially-grown self-assembled indium islands show promise as nanoantennas,<sup>16</sup> the internal structure of these islands has not been thoroughly explored. Prior work has indicated that these structures may contain impurities unique to the epitaxial growth process.<sup>17</sup> This paper seeks to describe and analyze the internal structure of indium islands grown under three different sets of growth conditions, in order to better predict the behavior and future applications of these plasmonic nanostructures.

## II. EXPERIMENT

The indium islands analyzed in this work were grown via Molecular Beam Epitaxy (MBE), using the equipment and procedures described in Ref. 17. The growth parameters of each sample are listed in Table I. Three samples, shown in Fig. 1, are discussed: a sample with islands averaging 125nm in diameter (In38), a sample with islands averaging 1.5 $\mu$ m in diameter (In44), and a sample with islands averaging 2.5 $\mu$ m in diameter (In54). All three samples were grown on GaAs substrates, and In38 contained an InGaAs quantum well 5nm below the surface of the substrate. For each sample, after completion of the substrate growth, the substrate was allowed to cool to a stable temperature and residual arsenic was pumped from the growth chamber before the deposition of indium.

In order to determine the spatially-dependent composition of the islands, a combination of Transmission Electron Microscopy (TEM) and Energy Dispersive Spectroscopy (EDS) was used. Thin cross-sections of each sample were analyzed by focusing a narrow electron beam on the sample and collecting the resulting x-ray spectrum. Each of the elements of interest have distinct x-ray emission spectra, as shown in Fig. 2, allowing qualitative maps of island composition to be constructed by collecting x-ray spectra from an array of points.

The analysis of the In38 islands was performed using a JEOL 2010F TEM with an EDAX-manufactured 30mm<sup>2</sup> atmospheric thin window SiLi EDX detector. A JEOL ARM200F with a JEOL-manufactured 50mm<sup>2</sup> windowless SiLi EDX detector was used to analyze the In44 and In54 islands. The resolution of the EDS area maps and line scans ranges from 1.4nm to 4nm. Quantitative EDS, measuring the average atomic percentage composition of a region, was performed by expanding the beam to cover a large area of the In38 and In44 islands, and by measuring an array of points on the In54 island. The measured area was approximately 10% of each of the In38 islands, 17% of the In44 island, and 3% of the In54 island. Quantitative EDS error estimates were obtained from the collection software and from calibration measurements.

TABLE I. Sample growth parameters.

Sample	Substrate temp. ( $^{\circ}$ C)	Indium temp. ( $^{\circ}$ C)	Arsenic clear time (hours)	Deposition rate	Monolayers of indium
In38	133	830	1.3	0.543 ML/sec	12
In44	131	510	12	1 ML/hour	12
In54	131	510	12	1 ML/hour	36

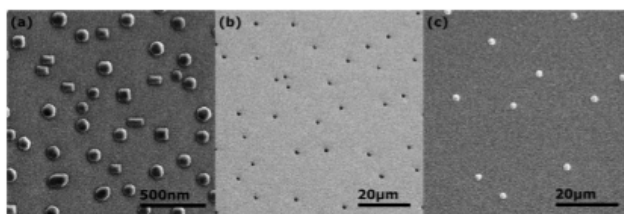


FIG. 1. SEM images of indium island samples In38 (a), In44 (b), and In54 (c).

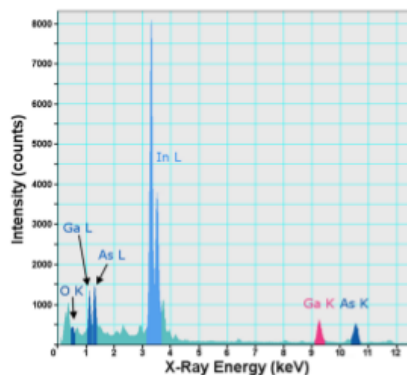


FIG. 2. An x-ray emission spectrum from In38. The peaks of each of the elements of interest (O, Ga, As, In) are highlighted to show that the In, Ga, and As lines do not overlap.

To prepare the TEM cross-sections, the regions to be analyzed were covered in a protective coating composed of 10nm of electron beam-deposited carbon, followed by 500nm of electron beam-deposited platinum, and finally 2 $\mu$ m of ion beam platinum, with the electron beam-deposited layers serving to protect the surface of the sample from damage during the deposition of the ion beam platinum layer. A slab of material was then cut from the bulk sample using a focused gallium ion beam. The slab was gradually thinned using progressively weaker beam strengths, with the protective coating preventing damage to the underlying sample. Cross-sections were thinned to roughly 60nm (In38) or 100nm (In44, In54). Due to differences in island spacing and size constraints on cross-section preparation, three In38, two In44, and one In54 island were analyzed.

### III. RESULTS

A quantitative comparison of island centers, found in Table II, shows increasing indium purity with increasing island size. However, the islands were not homogenous; Fig. 3 shows EDS maps of the islands, and Fig. 4 shows annotated line scans of the In54 island and one In38 island. These images reveal several distinct features: all three of the examined In38 islands contained large regions of high gallium and arsenic and low indium concentrations; both of the examined In44 islands contained high gallium and arsenic and low indium concentrations at the island corners; and the In54 island exhibited a 50nm-tall arsenic-rich band along the base of the island.

All islands contained low concentrations of oxygen, with most islands exhibiting a distinct surface oxide. This surface oxide was approximately 4-7.5nm thick on In38, 15-25nm thick on In44, and 25nm thick on In54; the ratio of oxide thickness to island base diameter was roughly 1:20 for In38 and 1:100 for In44 and In54. All islands also contained an InGaAs region along the island-substrate interface. This region was roughly 5nm thick in In38 (b) and (c) and 10nm thick in the In44 and In54 islands. In38 (a) did not exhibit a sharp transition. This intermixed region was highly localized in most of the islands – the In54 substrate showed only 3.65% indium just 7nm below the island, and

TABLE II. Elemental composition of island interiors by atomic percentage.

Sample	In	Ga	As
In38	66.0% ( $\pm 2\%$ )	12.7% ( $\pm 0.7\%$ )	21.3% ( $\pm 0.8\%$ )
	89.9% ( $\pm 1.5\%$ )	5.6% ( $\pm 0.5\%$ )	4.5% ( $\pm 0.5\%$ )
	82.5% ( $\pm 1.8\%$ )	8.0% ( $\pm 0.6\%$ )	9.4% ( $\pm 0.6\%$ )
In44	94.7% ( $\pm 1\%$ )	3.1% ( $\pm 0.5\%$ )	2.2% ( $\pm 0.5\%$ )
In54	96.1% ( $\pm 1\%$ )	2.5% ( $\pm 0.5\%$ )	1.41% ( $\pm 0.5\%$ )

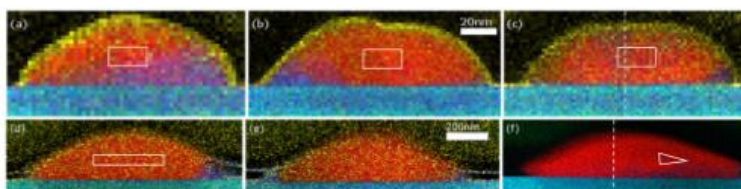


FIG. 3. False-color elemental composition maps of In38 (a, b, c), In44 (d, e), and In54 (f) islands. The white boxes show the approximate area over which quantitative EDS was performed, and the dashed lines show the line scan paths. The 20nm scale bar applies to a, b, and c, and the 200nm scale bar applies to d, e, and f. Red corresponds to In, blue to As, cyan to GaAs, purple to InGaAs, and yellow to O. Oxygen has been omitted from (f) to increase the visibility of As.

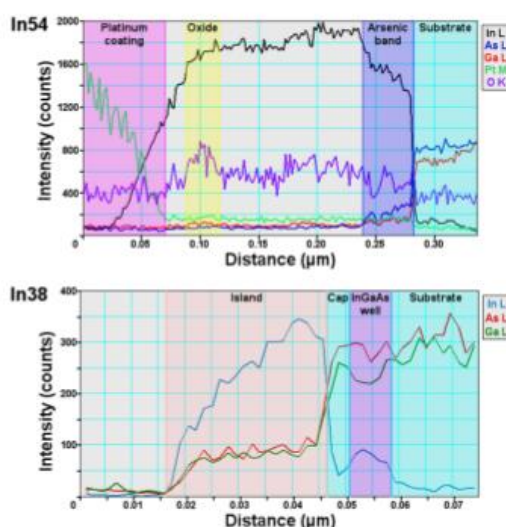


FIG. 4. Elemental composition line scans of In54 and In38, (f) and (c) in Fig. 3, with major regions highlighted. The line scan runs from above to below the In54 island and from below to above the In38 island. Lines are not normalized with respect to one another, but points along the same line can be qualitatively compared. The platinum coating has substantial overlap with the In54 island due to the TEM slice having non-negligible thickness compared to the curvature of the island.

0.66% indium 40nm below the island. Indium was also found in low concentrations in the GaAs cap layer separating the In38 islands from the InGaAs quantum well, as shown in Fig. 4b, although the InGaAs well remained distinct from the cap layer.

#### IV. DISCUSSION

The distribution of elements throughout the islands was not consistent between samples, suggesting that island properties or growth parameters may affect oxidation and intermixing between the substrate and islands. The high indium purities observed in the In44 and In54 islands indicate that superconducting behavior could be expected in these islands at low temperatures; superconductivity has been subsequently observed in In54.<sup>18</sup> However, it seems unlikely that the In38 islands would exhibit superconducting behavior.

The oxygen signal from the islands was very noisy, due to the weak oxygen K line and its proximity to unrelated peaks. The differences in oxide layer thickness between the In44 and In54 islands can potentially be explained by measurement resolution, margins of error, and cross-section thickness, but the In38 island oxides appear significantly thinner. The In38 slices were thinner than

the In44 and In54 slices, potentially giving a more accurate oxide thickness measurement. It is also possible that the higher concentrations of arsenic and gallium in the In38 islands impeded oxide growth, although the native oxides on both GaAs and pure indium tend to be roughly 4nm thick.<sup>19,20</sup>

The inhomogeneous distribution of material within the In38 islands coupled with the smoothness of the GaAs substrate suggest that the semiconductor pockets within the islands precipitated from material that diffused into the indium during the initial deposition, before the material redistributed into islands. The indium temperature during the growth of In38 was 830°C, substantially higher than the temperature required to melt most  $\text{In}_{1-x}\text{Ga}_x\text{As}$  alloys<sup>21</sup> and similar to temperatures at which pronounced In-Ga intermixing has been observed.<sup>22</sup>

Aside from different indium deposition temperatures, the arsenic pump-out time prior to growth was substantially shorter for In38 than for In44 or In54, which may have also contributed to the higher levels of arsenic found in the In38 islands. It is possible that the arsenic and gallium incorporated into the islands preferentially formed low-indium alloys which solidified while the rest of the island was still liquid, and which then combined into larger masses within the islands via Ostwald ripening.

In Fig. 1a, two island morphologies can be observed on In38: faceted islands, and rounded islands. Of the In38 islands examined, one (Fig. 3a) was faceted and two (Fig. 3b and c) were rounded. All three In38 islands exhibited substantial inhomogeneity; while the results suggest a possible relationship between In38 island morphology and composition, the number of characterized In38 islands is too small to draw meaningful conclusions.

The In44 and In54 island cross-sections showed arsenic and gallium contents that were lower on average and significantly more localized than in the In38 islands. The pattern of contamination at the corners of the In44 islands indicates the presence of a GaAs or InGaAs ring around the outer edge of the island, which may be similar to the InGaAs rings formed during GaAs capping of InAs quantum dots.<sup>23</sup> Although the length scales of the two systems are orders of magnitude different, it is possible that similar kinetic or thermodynamic forces are responsible for both; for example, the lattice constants of both InAs and crystalline indium are significantly greater than that of GaAs, suggesting that physical strain may play a similar role in quantum dot and larger island formation.

The arsenic-rich strip observed in In54 (Fig. 4) is not mirrored in the other samples. Gallium is also present in this band, but in lower quantities, suggesting that diffusion of arsenic into indium is more energetically favorable than the diffusion of gallium into indium under In54's growth conditions. Simulations in the literature indicate that arsenic may have a longer diffusion length than gallium at the In54 island-substrate interface temperature,<sup>24</sup> and arsenic is likely more mobile than gallium in pure indium due to the potential to form InAs rather than needing to fill indium vacancies.

The fairly-uniform horizontal distribution of arsenic and gallium in In54, along with the decay in concentration with increasing distance from the base of the island, indicate that the materials diffused from the substrate after the indium along the interface had become relatively stationary. The arsenic and gallium concentrations in the In38 islands do not show a similar decay with island height over distances similar to the height of the In54 arsenic band, supporting the earlier remark that the presence of arsenic and gallium in the In38 islands is likely not the result of diffusion post-island formation.

The observed patterns of intermixing suggest that low indium deposition temperatures are necessary for the formation of high-purity, homogeneous islands. In addition, shorter growth times may limit diffusion between the substrate and islands. The arsenic band along the base of the In54 island and the arsenic- and gallium-rich rings around the In44 islands seem unlikely to have a significant effect on nanoantenna behavior, but may impact the potential formation of Majorana fermions in islands coupled to InAs nanowires.

In summary, indium islands grown with low indium deposition temperatures exhibited high (>94%) indium purity throughout the main body of the island and highly-localized arsenic and gallium contamination. Low indium deposition temperature but longer deposition time resulted in very similar average indium purity, but the formation of a broad band of contamination along the island-substrate interface. Islands grown with high indium deposition temperatures contained large, irregular regions of gallium and arsenic contamination and a significantly lower (80%) average indium purity. The islands grown with a low indium deposition temperature were 1.5 $\mu\text{m}$  or larger in diameter, while the islands grown with a high indium deposition temperature were an average of 125nm in diameter. These results suggest that low indium deposition temperatures and short growth

times contribute to the formation of high-purity, homogeneous islands. These results also suggest that superconducting behavior may be generally achievable in micron-scale islands, corresponding to mid-IR resonances. Modification of growth parameters may be necessary to produce self-assembled superconducting visible or near-IR nanoantenna arrays.

## SUPPLEMENTARY MATERIAL

See [supplementary material](#) for single-element composition maps and additional line scans.

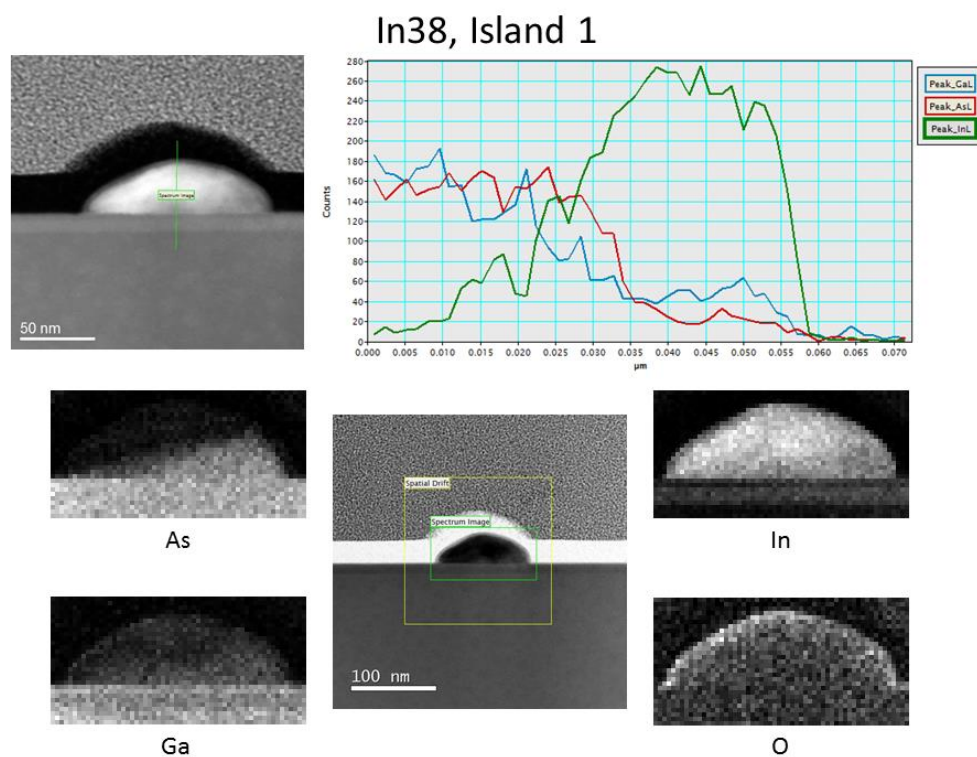
## ACKNOWLEDGMENTS

We gratefully acknowledge the use of facilities with the LeRoy Eyring Center for Solid State Science at Arizona State University. This work was funded by the Air Force Office of Scientific Research (AFOSR, Dr. Gernot Pomrenke, Grant FA9550-13-1-0003), the National Science Foundation Atomic, Molecular and Optical Physics (NSF-AMOP 1205031) and the Engineering Research Center for Integrated Access Networks (NSF ERC-CIAN, Award EEC-0812072). JS would like to acknowledge the support of Arizona Technology and Research Initiative Funding (TRIF) and Professor Euan McLeod. MG would like to acknowledge the support of the Department of Defense through the National Defense Science and Engineering Graduate (NDSEG) Fellowship Program. SZ would like to acknowledge the support of the Department of Energy (DOE) through the Office of Science Graduate Fellowship (SCGF) made possible in part by the American Recovery and Reinvestment Act of 2009, administered by ORISE-ORAU under Contract no. DE-AC05-06OR23100. JH would like to acknowledge support from the Air Force Office of Scientific Research (AFOSR, Program Manager – Dr. Gernot Pomrenke, Contract 12RY05COR). AA would like to acknowledge support from the French technology network RENATECH.

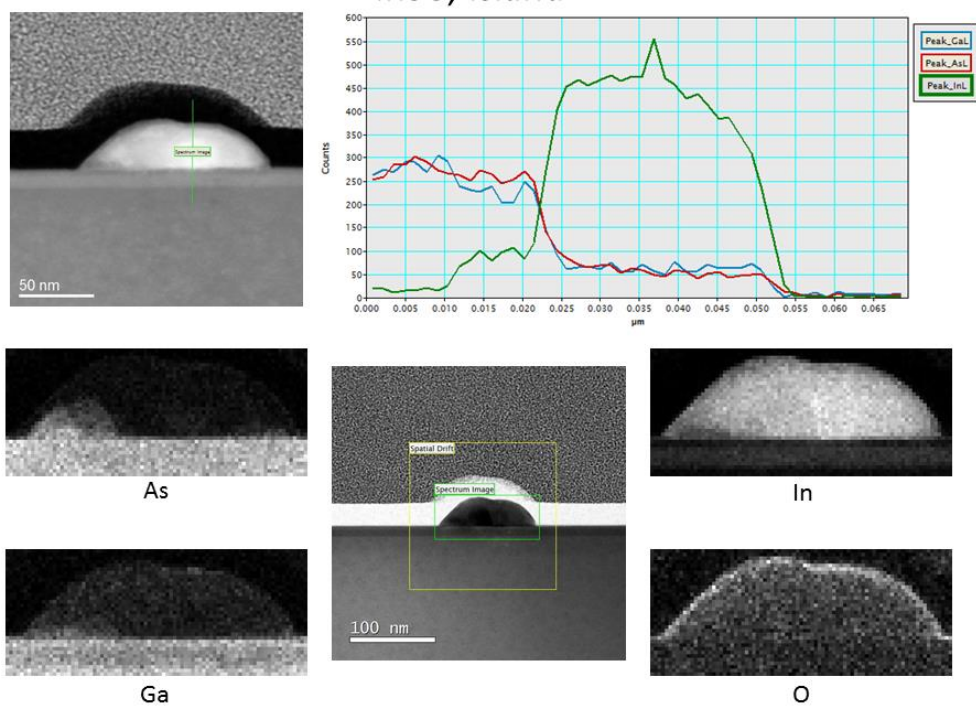
- <sup>1</sup>M. A. Nazirzadeh, F. B. Atar, B. B. Turgut, and A. K. Okyay, *Sci. Rep.* **4**, 7103 (2014).
- <sup>2</sup>S. Mokkaapati, F. J. Beck, R. de Waele, A. Polman, and K. R. Catchpole, *J. Phys. D: Appl. Phys.* **44**, 185101 (2011).
- <sup>3</sup>M. F. G. Klein, H. Hein, P. Jakobs, S. Linden, N. Meinzer, M. Wegener, V. Saile, and M. Kohl, *Microelectron. Eng.* **86**, 1078 (2009).
- <sup>4</sup>A. Kawakami, S. Saito, and M. Hyodo, *IEEE Trans. Appl. Supercond.* **21**, 632 (2011).
- <sup>5</sup>H. Chen, A. M. Bhuiya, R. Liu, D. M. Wasseman, and K. C. Toussaint, *J. Phys. Chem. C* **118**, 20553 (2014).
- <sup>6</sup>M. N. Gadalla, M. Abdel-Rahman, and A. Shamim, *Sci. Rep.* **4**, 4270 (2014).
- <sup>7</sup>M. Gehl, S. Zandbergen, R. Gibson, M. Béchu, N. Nader, J. Hendrickson, J. Sears, P. Keiffer, M. Wegener, and G. Khitrova, *J. Opt.* **16**, 114016 (2014).
- <sup>8</sup>N. Meinzer, M. Ruther, S. Linden, C. M. Soukoulis, G. Khitrova, J. Hendrickson, J. D. Olitsky, H. M. Gibbs, and M. Wegener, *Optics Express* **18**, 24140 (2010).
- <sup>9</sup>A. Urbańczyk and R. Nötzel, *J. Appl. Phys.* **112**, 124302 (2012).
- <sup>10</sup>A. Urbańczyk, G. J. Hamhuis, and R. Nötzel, *Appl. Phys. Lett.* **96**, 113101 (2010).
- <sup>11</sup>M. Leijnse and K. Flensberg, *Semicond. Sci. Technol.* **27**, 124003 (2012).
- <sup>12</sup>C. W. J. Beenakker, *Annu. Rev. Condens. Matter Phys.* **4**, 113–136 (2013).
- <sup>13</sup>V. Mourik, K. Zuo, S. M. Frolov, S. R. Plissard, E. P. A. M. Bakkers, and L. P. Kouwenhoven, *Science* **336**, 1003 (2012).
- <sup>14</sup>Y. Oreg, G. Refael, and F. von Oppen, *Phys. Rev. Lett.* **105**, 177002 (2010).
- <sup>15</sup>R. M. Lutchyn, J. D. Sau, and S. Das Sarma, *Phys. Rev. Lett.* **105**, 077001 (2010).
- <sup>16</sup>A. Urbańczyk, G. J. Hamhuis, and R. Nötzel, *Nanoscale Res. Lett.* **5**, 1926 (2010).
- <sup>17</sup>R. Gibson, M. Gehl, J. Sears, S. Zandbergen, N. Nader, P. Keiffer, J. Hendrickson, A. Arnoult, and G. Khitrova, *J. Cryst. Growth* **425**, 307 (2015).
- <sup>18</sup>M. Gehl, R. Gibson, S. Zandbergen, P. Keiffer, J. Sears, and G. Khitrova, *JOSA B* **33**, C50 (2016).
- <sup>19</sup>P. J. Grunthaner, *J. Vac. Sci. Technol.* **17**, 1045 (1980).
- <sup>20</sup>J. Kim, H. Schoeller, J. Cho, and S. Park, *J. Electron. Mater.* **37**, 483 (2007).
- <sup>21</sup>N. J. Quitoriano and E. A. Fitzgerald, *J. Appl. Phys.* **102**, 033511 (2007).
- <sup>22</sup>N. A. Bert, V. V. Chaldyshev, Yu. G. Musikhin, A. A. Suvorova, V. V. Proembrazhenskii, M. A. Putyato, B. R. Semyagin, and P. Wemer, *Appl. Phys. Lett.* **74**, 1442 (1999).
- <sup>23</sup>J. M. García, G. Medeiros-Ribeiro, K. Schmidt, T. Ngo, J. L. Feng, A. Lorke, J. Kotthaus, and P. M. Petroff, *Appl. Phys. Lett.* **71**, 2014 (1997).
- <sup>24</sup>A. Amrani, M. Djafari Rouhani, and A. A. Mraoufel, *Appl. Nanosci.* **1**, 59 (2011).

## APPENDIX C – ADDITIONAL TEM EDS DATA

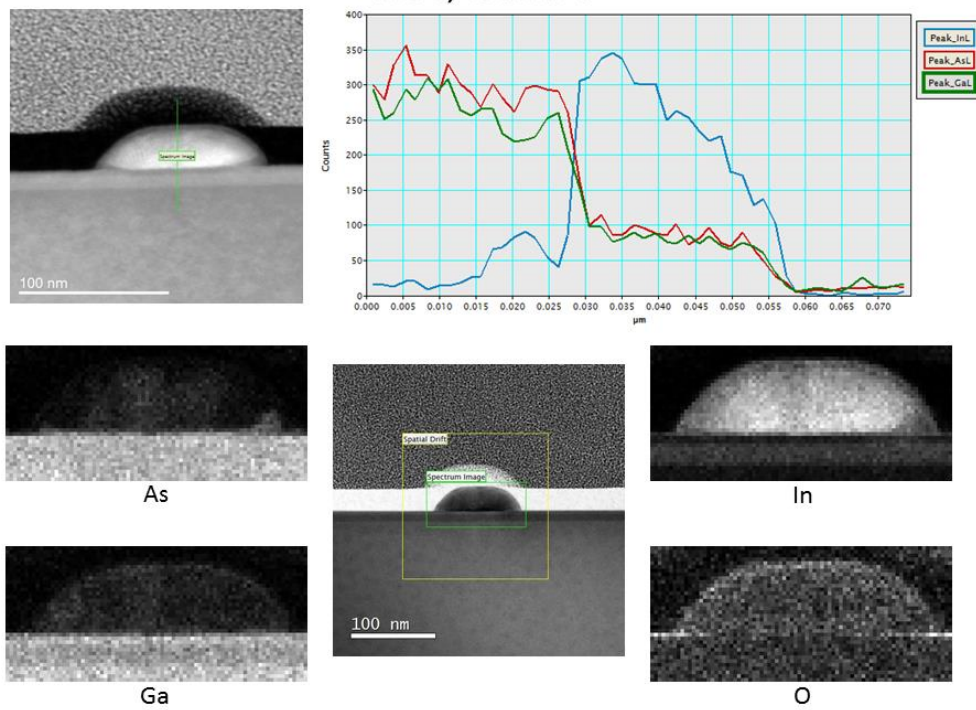
This appendix contains the raw line scans and individual element area maps of the islands discussed in Chapter 4.



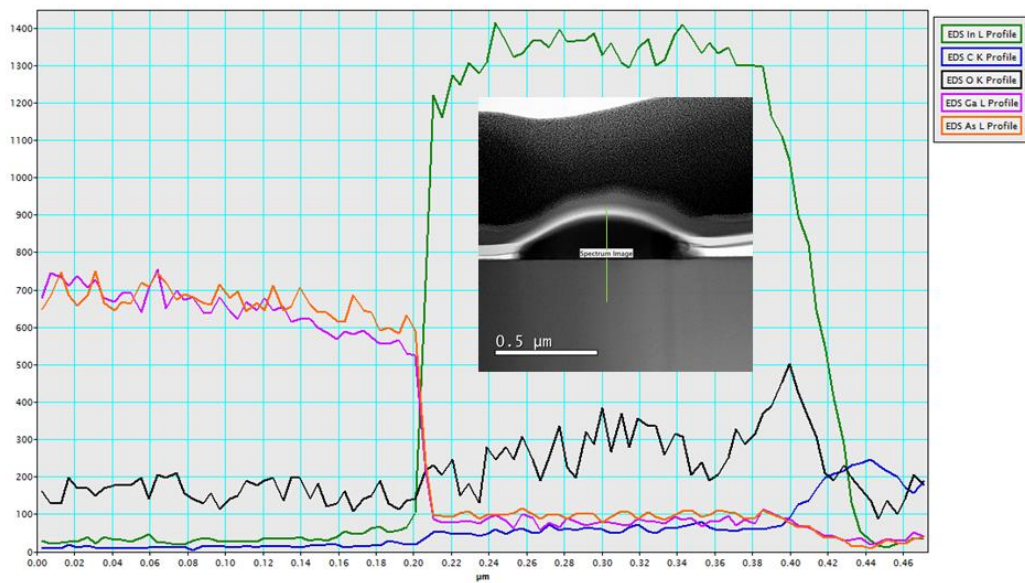
## In38, Island 2



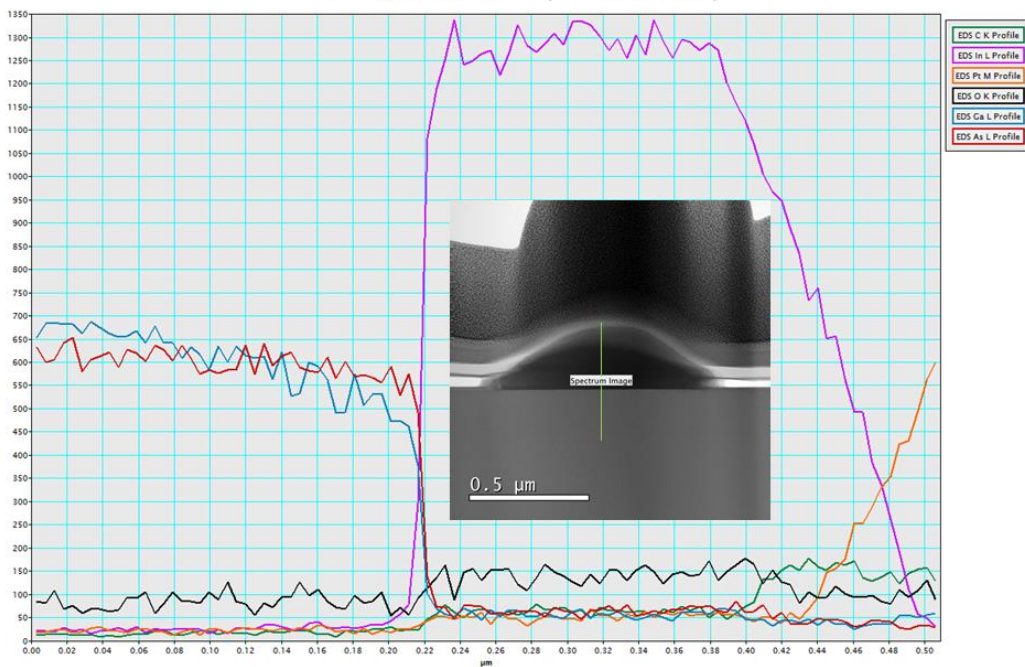
## In38, Island 3



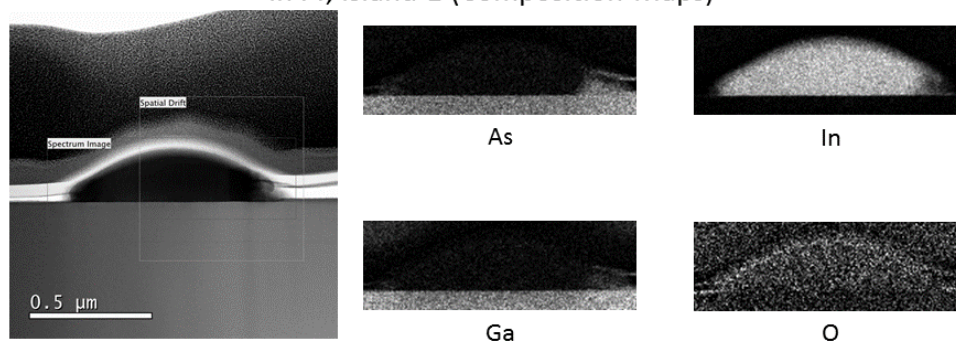
## In44, Island 1 (Line Scan)



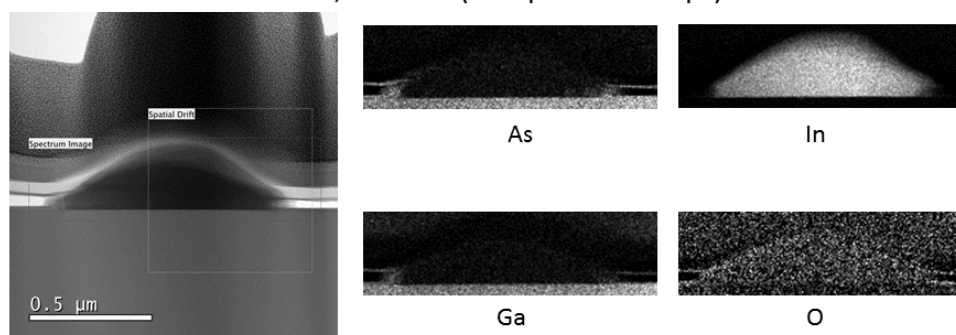
## In44, Island 2 (Line Scan)



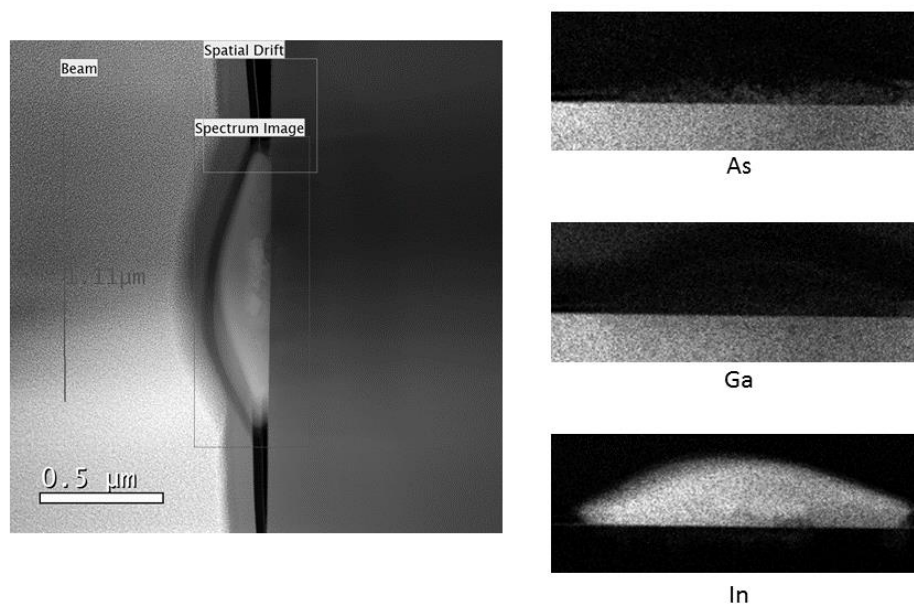
## In44, Island 1 (Composition Maps)



## In44, Island 2 (Composition Maps)



## In54, Island 1 (Composition Maps)



## REFERENCES

- [1] S. A. Dereshgi, Z. Sisman, K. Topalli, and A. K. Okyay, “Plasmonically enhanced metal–insulator multistacked photodetectors with separate absorption and collection junctions for near-infrared applications,” *Scientific Reports* 7, 42349 (2017). doi:10.1038/srep42349
- [2] M. A. Nazirzadeh, F. B. Atar, B. B. Turgut, & A. K. Okyay, “Random sized plasmonic nanoantennas on Silicon for low-cost broad-band near-infrared photodetection,” *Scientific Reports* 4, 7103 (2014). doi:10.1038/srep07103
- [3] S. Mokkaapati, F. J. Beck, R. de Waele, A. Polman, & K. R. Catchpole, “Resonant nano-antennas for light trapping in plasmonic solar cells,” *Journal of Physics D: Applied Physics* 44, 185101 (2011). doi:10.1038/nmat3356
- [4] O. Hess, J. B. Pendry, S. A. Maier, R. F. Oulton, J. M. Hamm, and K. L. Tsakmakidis, “Active nanoplasmonic metamaterials,” *Nature Materials* 11, 573–584 (2012).
- [5] P. J. Shadbolt, M. R. Verde, A. Peruzzo, A. Politi, A. Laing, M. Lobino, J. C. F. Matthews, M. G. Thompson, and J. L. O'Brien, “Generating, manipulating and measuring entanglement and mixture with a reconfigurable photonic circuit,” *Nature Photonics* 6, 45-49 (2012). doi:10.1038/nphoton.2011.283
- [6] B. E. A. Saleh and M. C. Teich, *Fundamentals of Photonics*, Second Edition, 376 (Wiley, 2007).
- [7] C. Santis and A. Yariv, “High-Q silicon resonators for high-coherence hybrid Si/III-V semiconductor lasers,” *CLEO: 2015, SW3F.6* (2015). doi:10.1364/CLEO\_SI.2015.SW3F.6
- [8] M. Gehl, “Controlling light-matter interaction in semiconductors with hybrid nano-structures,” Ph.D. dissertation, University of Arizona (2015).
- [9] C. Cohen-Tannoudji, B. Diu, and F. Laloë, *Quantum Mechanics Volume One*, 67-78 (Wiley, 2005).
- [10] H. Brech, “Optimization of GaAs based high electron mobility transistors by numerical simulations,” Ph.D. dissertation, Vienna University of Technology (1998). [http://www.iue.tuwien.ac.at/phd/brech/ch\\_2\\_2.htm](http://www.iue.tuwien.ac.at/phd/brech/ch_2_2.htm)
- [11] J.-H. Song, J. Kim, H. Jang, I. Y. Kim, I. Karnadi, J. Shin, J. H. Shin, and Y.-H. Lee, “Fast and bright spontaneous emission of Er<sup>3+</sup> ions in metallic nanocavity,” *Nature Communications* 6, 7080 (2015). doi:10.1038/ncomms8080

- [12] R. Gibson, "Plasmonic and superconducting self-assembled MBE grown indium islands," Ph.D. dissertation, University of Arizona (2016).
- [13] A. Rosenauer, D. Gerthsen, D. Van Dyck, M. Arzberger, G. Böhm, and G. Abstreiter, "Quantification of segregation and mass transport in  $\text{In}_x\text{Ga}_{1-x}\text{As}/\text{GaAs}$  Stranski-Krastanow layers," *Physical Review B* 64, 245334 (2001). doi:10.1103/PhysRevB.64.245334
- [14] Tien (1988), unpublished.
- [15] J. L. Robins, "Characteristic Electron Energy Loss Spectra of a Number of Solid Elements," *Proceedings of the Physical Society* 79, 119-132 (1962).
- [16] B. Hafner, "Energy Dispersive Spectroscopy on the SEM: A Primer," Characterization Facility, University of Minnesota.  
[http://www.charfac.umn.edu/instruments/eds\\_on\\_sem\\_primer.pdf](http://www.charfac.umn.edu/instruments/eds_on_sem_primer.pdf)
- [17] Z. Zhou, B. Yin, and J. Michel, "On-chip light sources for silicon photonics," *Light: Science & Applications* 4, e358 (2015). doi:10.1038/lisa.2015.131
- [18] <http://cian-erc.webhost.uits.arizona.edu/silicon-photonics>
- [19] R. Gibson, M. Gehl, A. Homyk, A. Saynatjok, L. Karvonen, A. Tervonen, S. Honkanen, S. Zandbergen, J. D. Olitzky, J. Sears, K. Kieu, A. Scherer, G. Khitrova, H. M. Gibbs, J.-Y. Kim, Y.-H. Lee, and J. Hendrickson, "C3-1 Applications for Silicon Nanobeam Cavities," CIAN Site Visit, Tucson, AZ (2012).
- [20] B. E. A. Saleh and M. C. Teich, *Fundamentals of Photonics*, Second Edition, 350 (Wiley, 2007).
- [21] M. A. Ali, A. F. Elrefaie, R. E. Wagner, F. Mendez, J. Pan, and S. A. Ahmed, "Optimized performance of erbium-doped fiber amplifiers in multiwavelength lightwave systems," *IEEE Photonics Technology Letters* 6, 1039-1042 (1994). doi:10.1109/68.313087
- [22] K. Kieu, S. Mehravar, R. Gowda, R. A. Norwood, and N. Peyghambarian, "Label-free multi-photon imaging using a compact femtosecond fiber laser mode-locked by carbon nanotube saturable absorber," *Biomedical Optics Express* 4, 2187-2195 (2013).  
doi:10.1364/BOE.4.002187
- [23] K. Solehmainen, M. Kapulainen, P. Heimala, and K. Polamo, "Erbium-doped waveguides fabricated with atomic layer deposition method," *IEEE Photonics Technology Letters* 16, 194-196 (2004). doi:10.1109/LPT.2003.820484

- [24] M. Gehl, R. Gibson, J. Hendrickson, A. Homyk, A. Säynätjoki, T. Alasaarela, L. Karvonen, A. Tervonen, S. Honkanen, S. Zandbergen, B. C. Richards, J. D. Oltzky, A. Scherer, G. Khitrova, H. M. Gibbs, J.-Y. Kim, and Y.-H. Lee, "Effect of atomic layer deposition on the quality factor of silicon nanobeam cavities," *JOSA B* 29, A55-A59 (2012). doi:10.1364/JOSAB.29.000A55
- [25] P. Myslinski, D. Nguyen, and J. Chrostowski, "Effects of concentration on the performance of erbium-doped fiber amplifiers," *Journal of Lightwave Technology* 15, 112-120 (1997). doi:10.1109/50.552118
- [26] V. M. Marchenko, L. D. Iskhakova, and M. I. Studenikin, "Selective emission and luminescence of Er<sub>2</sub>O<sub>3</sub> under intense laser excitation," *Quantum Electronics* 43, 859-864 (2013). doi:10.1070/QE2013v043n09ABEH015158
- [27] A. E. Miroshnichenko, S. Flach, and Y. S. Kivshar, "Fano resonance in nanoscale structures," arXiv, (2009).
- [28] Y. Xu, Y. Li, R. K. Lee, and A. Yariv, "Scattering-theory analysis of waveguide-resonator coupling," *Physical Review E* 5, 7389-404 (2000). doi:10.1103/PhysRevE.62.7389
- [29] I. Avrutsky, R. Gibson, J. Sears, G. Khitrova, H. M. Gibbs, and J. Hendrickson, "Linear systems approach to describing and classifying Fano resonances," *Physical Review B* 87, 125118 (2013). doi:10.1103/PhysRevB.87.125118
- [30] M. Gehl, S. Zandbergen, R. Gibson, M. Béchu, N. Nader, J. Hendrickson, J. Sears, P. Keiffer, M. Wegener, and G. Khitrova "Spectroscopic studies of resonant coupling of silver optical antenna arrays to a near-surface quantum well," *Journal of Optics* 16, 114016 (2014). doi:10.1088/2040-8978/16/11/114016
- [31] M. B. Ross and G. C. Schatz, "Aluminum and Indium Plasmonic Nanoantennas in the Ultraviolet," *Journal of Physical Chemistry C* 118, 12506-12514 (2014). doi:10.1021/jp503323u
- [32] E. Cottancin, C. Langlois, J. Lermé, M. Broyer, M.-A. Lebeault, and M. Pellarin, "Plasmon spectroscopy of small indium–silver clusters: monitoring the indium shell oxidation," *Physical Chemistry Chemical Physics* 16, 5763-5773 (2014). doi:10.1039/C3CP55135K
- [33] Y.-J. Lu, J. Kim, H.-Y. Chen, C. Wu, N. Dabidian, C. E. Sanders, C.-Y. Wang, M.-Y. Lu, B.-H. Li, X. Qiu, W.-H. Chang, L.-J. Chen, G. Shvets, C.-K. Shih, and S. Gwo, "Plasmonic Nanolaser Using Epitaxially Grown Silver Film," *Science* 337, 450-453 (2012). doi:10.1126/science.1223504

- [34] M. Leijnse and K. Flensberg, "Introduction to topological superconductivity and Majorana fermions," *Semiconductor Science and Technology* 27, 124003 (2012). doi:10.1088/0268-1242/27/12/124003
- [35] C. W. J. Beenakker, "Search for Majorana Fermions in Superconductors," *Annual Review of Condensed Matter Physics* 4, 113–136 (2013). doi:10.1146/annurev-conmatphys-030212-184337
- [36] Y. Oreg, G. Refael, and F. von Oppen, "Helical Liquids and Majorana Bound States in Quantum Wires," *Physical Review Letters* 105, 177002 (2010). doi:10.1103/PhysRevLett.105.177002
- [37] R. M. Lutchyn, J. D. Sau, and S. Das Sarma, "Majorana Fermions and a Topological Phase Transition in Semiconductor-Superconductor Heterostructures," *Physical Review Letters* 105, 077001 (2010). doi:10.1103/PhysRevLett.105.077001
- [38] W. H. P. Pernice, C. Schuck, O. Minaeva, M. Li, G. N. Goltsman, A. V. Sergienko, and H. X. Tang, "High-speed and high-efficiency travelling wave single-photon detectors embedded in nanophotonic circuits," *Nature Communications* 3, 1325 (2012). doi:10.1038/ncomms2307
- [39] P. E. Vullum, M. Nord, M. Vatanparast, S. F. Thomassen, C. Boothroyd, R. Holmestad, B.-O. Fimland, and T. W. Reenaas "Quantitative strain analysis of InAs/GaAs quantum dot materials," *Scientific Reports* 7, 45376 (2017). doi:10.1038/srep45376
- [40] J. Sears, R. Gibson, M. Gehl, S. Zandbergen, P. Keiffer, N. Nader, J. Hendrickson, A. Arnoult, and G. Khitrova, "TEM EDS analysis of epitaxially-grown self-assembled indium islands," *AIP Advances* 7, 055005 (2017). doi:10.1063/1.4983492
- [41] C. Lehrer, L. Frey, S. Petersen, M. Mizutani, M. Takai, and H. Ryssel, "Defects and gallium-contamination during focused ion beam micro machining," *Conference on Ion Implantation Technology*, 695-698 (2000). doi:10.1109/IIT.2000.924248
- [42] A. Kadir, S. Mukhopadhyay, T. Ganguli, C. Galande, M. R. Gokhale, B. M. Arora, P. Raychaudhuri, and A. Bhattacharya, "Non-intrinsic superconductivity in InN epilayers: Role of Indium Oxide," *Solid State Communications* 146, 361-364 (2008). doi:10.1016/j.ssc.2008.04.002
- [43] P. Taylor, "Ostwald ripening in emulsions," *Advances in Colloid and Interface Science* 75, 107-163 (1998). doi:10.1016/S0001-8686(98)00035-9
- [44] M. Gehl, R. Gibson, S. Zandbergen, P. Keiffer, J. Sears, and G. Khitrova, "Superconductivity in epitaxially grown self-assembled indium islands: progress towards hybrid

superconductor/semiconductor optical sources,” *JOSA B* 33, C50-C56 (2016).  
doi:10.1364/JOSAB.33.000C50

[45] T. Ioppolo and M. Manzo, “Dome-shaped whispering gallery mode laser for remote wall temperature sensing,” *Applied Optics* 53, 5065-5069 (2014). doi:10.1364/AO.53.005065

[46] D. Ta, R. Chen, and H. Sun, “Flexible microresonators: Lasing and sensing,” *Conference on Laser Resonators, Microresonators, and Beam Control XVI*, 8960 (2014).  
doi:10.1117/12.2036890

[47] G. C. Righini, Y. Dumeige, P. Feron, M. Ferrari, G. Nunzi Conti, D. Ristic, and S. Soria, “Whispering gallery mode microresonators: Fundamentals and applications,” *Rivista Del Nuovo Cimento* 34, 435-488 (2011). doi:10.1393/ncr/i2011-10067-2

[48] K. Kudo, Y. Makita, I. Takayasu, and T. Nomura, “Photoluminescence spectra of undoped GaAs grown by molecular-beam epitaxy at very high and low substrate temperatures,” *Journal of Applied Physics* 59, 888 (1986). doi:10.1063/1.336559

[49] H. Kim, W.-J. Lee, A. C. Farrell, A. Balgarkashi, and D. L. Huffaker, “Telecom-Wavelength Bottom-up Nanobeam Lasers on Silicon-on-Insulator,” *Nano Letters* (2017).  
doi:10.1021/acs.nanolett.7b01360

[50] R. Gibson, M. Gehl, J. Sears, S. Zandbergen, N. Nader, P. Keiffer, J. Hendrickson, A. Arnoult, and G. Khitrova, “Molecular beam epitaxy grown indium self-assembled plasmonic nanostructures,” *Journal of Crystal Growth* 425, 307-311 (2015).  
doi:10.1016/j.jcrysgro.2015.02.058

[51] I. Gontijo, M. Boroditsky, E. Yablonovitch, S. Keller, U.K. Mishra, S.P. Den Baars, M. Krames, “Coupling of InGaN quantum well photoluminescence to silver surface plasmons,” *LEOS* (1999). doi:10.1109/LEOS.1999.813496

[52] D. Iida, A. Fadil, Y. Chen, Y. Ou, O. Kopylov, M. Iwaya, T. Takeuchi, S. Kamiyama, I. Akasaki, and H. Ou, “Internal quantum efficiency enhancement of GaInN/GaN quantum-well structures using Ag nanoparticles,” *AIP Advances* 5, 097169 (2015). doi:10.1063/1.4931948

[53] A. Neogi, C.-W. Lee, H. O. Everitt, T. Kuroda, A. Tackeuchi, and E. Yablonovitch, “Enhancement of spontaneous emission in a quantum well by resonant surface plasmon coupling,” *Physical Review B* 66, 153305 (2002). doi:10.1103/PhysRevB.66.153305

[54] J.-J. DeLisle, “GaN Enables RF Where LDMOS And GaAs Can't,” (2014).  
<http://www.mwrf.com/active-components/gan-enables-rf-where-ldmos-and-gaas-cant>

[55] S. Chen, W. Lin, S. Li, and J. Kang, "Electronic structures of InN/GaN quantum dots," *Journal of Nanoscience and Nanotechnology* 9, 1226-1228 (2009).

[56] I. Vurgaftman and J. R. Meyer, "Band parameters for III–V compound semiconductors and their alloys," *Journal of Applied Physics* 89, 5815 (2001). doi:10.1063/1.1368156